Numerical Simulation of Ship Motion under Consideration of Design Criterion for Dynamic-Positioning-Systems

Vom Promotionsausschuss der
Technischen Universität Hamburg
zur Erlangung des akademischen Grades
Doktor-Ingenieur
genehmigte Dissertation

von

Bernhard Lasse Theilen

aus

Bremen

2024

Vorsitzender des Prüfungsausschusses:
Prof. Dr.-Ing. Stefan Krüger

Gutachter
1. Gutachter: Prof. Dr.-Ing. Moustafa Abdel-Maksoud
2. Gutachter: Prof. Dr.-Ing. Robert Seifried

Tag der mündlichen Prüfung:
17. April 2024

Am Schwarzenberg-Campus 4 (C)
21073 Hamburg
https://www.tuhh.de/vss/

Bericht Nr. 731
ISBN 978-3-89220-731-3

Acknowledgment

Throughout the entire research of my thesis I experienced helpful support. Therefore, I would like to address my graduate to the staff on the Institute of Fluid Dynamics and Ship Theory of Hamburg University of Technology. Special gratitude go to my supervisor Prof. Dr.-Ing. Moustafa Abdel-Maksoud for the scientific supervision of my work at the Institute of Fluid Dynamics and Ship Theory of Hamburg University of Technology. I am very grateful for his unlimited support and for the opportunity he offered me to gain various experiences during my time at the institute. The work and interpersonal experiences have had a great impact on me and are still decisive for me in my future career.
I also would like to thank Dr. Dirk Jürgens, Michael Palm and Philipp Koschorrek from Voith Turbo GmbH, with whom I was able to work on this very enthusiastic development of DP-Systems with Voith-Schneider-Propeller. With their support I was always inspired to my research project. Further, I would like to thank Marc Steinwand and Dr. Matthias Fröhlich as well as the staff from the SVA-Potsdam for their immense effort and care during the intense test campaigns.
Many thanks go to my colleague and office roommate Ole Detlefsen who was always helpful in fruitful discussions about the seakeeping of ships as well as technical support.
Further, I thank Prof. Dr.-Ing Stefan Krüger and Prof. Dr.-Ing. Robert Seifried for their advice on the thesis and the interesting discussions during the defense.
I would also like to thank my parents-in-law for their thoughts and good advice, which have always been a help to me. Last but not least, I would like to express my special thanks to my parents, who have supported me and encouraged me over all years. With their care and faith in me, I could always be confident on every path I took.
Finally, my last thanks go to my dear wife Xiaojing, to whom I owe endless support and ultimately the incentive to finish this work successfully. I am very grateful to have her and our wonderful children Phileas and Frido at my side.

This work was supported by the German Federal Ministry of Economics and Technology (BMWi) under grants DPMotion (No. 03SX351D) and DP-II (No. 03SX428C).

Zusammenfassung

Die vorliegende Arbeit beschäftigt sich mit der Entwicklung und Anwendung einer Simulationsplattform *"DPTool"* für die Bewertung der dynamischen Positionshaltefähigkeit (DP) von typischen DP-Schiffen mit Voith-Schneider-Propellern im Zeitbereich. Die Plattform berücksichtigt realistische Umweltbelastungen wie Wind, Wellen und Strömungen, die sowohl numerisch als auch experimentell untersucht wurden. Die numerischen Methoden umfassen die Simulation der Schiffsbewegung im Seegang, die Parametrierung des Reglers durch eine System-Identifikation und einem Allokationsmodul zur Festlegung der Steuergrößen an den Manövrierorganen. Die Methoden sind in einem ganzheitlichen MATLAB/Simulink-Modell als "Software-in-the-Loop" (SIL) integriert und über eine graphische Oberfläche zu bedienen.
Die Schiffsbewegung wird mit der auf den Impuls-Antwort-Funktionen basierenden Methode "IMPRES" in der Potentialtheorie simuliert. Die Regelung des DP-Systems erfolgt durch einen nichtlinearen PID-Regler mit einem Kalman-Filter für die Schiffsbewegungen im Seegang. Ein Optimierungsalgorithmus wird für das Allokationsmodul verwendet, mit dem in kurzer Zeit und energieeffizient die erforderlichen Manövrierkräfte realistisch erzeugt werden können.
Im Rahmen der Arbeit sind die Wind-, Strömungs- und Wellenkräfte an zwei Modellen, einem Offshore Versorger und einem Schlepper, in Experimenten untersucht und gemessen worden. Die Messungen der Windlasten wurden in dem Windkanal der Technischen Universität Hamburg-Harburg durchgeführt. Im Vorlauf der Messungen ist der Einfluss der Bodengrenzschicht des Windkanals untersucht worden. Die Strömungskräfte sind in dem Schlepptank der SVA-Potsdam gemessen worden. Hierfür ist das Modell des Offshore Versorgers an einer Kraftmesswaage mit verschiedenen Begegnungswinkeln und Geschwindigkeiten durch den Tank geschleppt worden. Ein Vergleich der ausgewerteten Experimente mit drei verschiedenen numerischen Methoden, einer stationären und einer transienten RANS Simulation sowie einem hybriden DES Ansatz, quantifiziert die Abweichungen der unterschiedlichen Methoden zum Experiment. Die Ermittlung der Wellenkräfte wurde durch eine Einspannung des Modells mit Federn realisiert, sodass Bewegungen erster Ordnung vollständig möglich waren. Die Messungen wurden mit drei verschiedenen numerischen Methoden verglichen: einer zweidimensionalen Streifenmethode PDStrip und einem dreidimensionalen Paneelverfahren im Frequenzbereich sowie einem RANS Verfahren.
Die Auswirkungen der Abweichungen zwischen den experimentellen und den numerisch simulierten Kräften auf die DP-Simulationen sind in der Arbeit durch vergleichende Simulationen dargestellt. Die Funktionalitäten des *"DPTool"* sind in einem Anwendungsfall gezeigt. Dabei ist ein Vergleich einer statischen und der in dieser Arbeit entstandenen dynamischen Methode im Zeitbreich verglichen worden.

Summary

The present thesis is concerned with the development and application of a simulation platform called "DPTool" for evaluating the Dynamic-Positioning (DP) capability of typical DP vessels with Voith-Schneider propellers in the time domain. The platform takes into account realistic environmental loads such as wind, waves, and currents, which have been investigated both numerically and experimentally. The numerical methods include simulating ship motion in waves, parameterizing control using system identification, and an allocation module for determining control inputs to maneuvering devices. These methods are integrated into a holistic MATLAB/Simulink model as a "Software-in-the-Loop" (SIL) and can be operated through a graphical interface.

Ship motion is simulated using the "IMPRES" method based on impulse response functions in potential theory. The DP system control is achieved through a nonlinear PID controller with a Kalman filter for ship motion in waves. An optimization algorithm is used for the allocation module to generate the required maneuvering forces realistically and efficiently within a short time.

In the scope of this work, wind, current, and wave forces on two models, an offshore supply vessel and a tugboat, have been investigated and measured through experiments. Wind force measurements were conducted in the wind tunnel of the Hamburg University of Technology. The influence of the wind tunnel's boundary layer was examined prior to the measurements. Flow forces were measured in the towing tank of SVA-Potsdam. For this purpose, the offshore supply vessel model was towed through the tank at various encounter angles and speeds using a force measurement carriage. A comparison of the evaluated experiments with three different numerical methods - a steady-state and a transient Reynolds-Averaged Navier-Stokes (RANS) simulation, as well as a hybrid Detached Eddy Simulation (DES) approach - quantifies the discrepancies between the various methods and the experiments. Determination of wave forces was achieved by restraining the model with springs, allowing for full first-order motion. The measurements were compared with three different numerical methods: a two-dimensional strip method PDStrip, a three-dimensional panel method in the frequency domain, and a transient RANS method.

The impacts of deviations between experimental and numerically simulated forces on DP simulations are presented in the work through comparative simulations. The functionalities of the "DPTool" are demonstrated in a use case, comparing a static method with the dynamic method developed in this work in the time domain.

Contents

Nomenclature **V**

List of Figures **VII**

List of Tables **X**

1 Introduction **1**

1.1 Motivation . . . 2
1.2 Review on previous work . . . 3
1.2.1 Simulation of dynamic positioning maneuvers . . . 3
1.2.2 Wind loads on ships . . . 4
1.2.3 Current loads on ships . . . 5
1.2.4 Wave drift loads on ships . . . 6
1.3 Present work . . . 7
1.3.1 Contributions in the present work . . . 9
1.3.2 Introduction of typical DP vessels using VSP . . . 9
1.3.3 Layout of the thesis . . . 11

2 Fundamentals **13**

2.1 Governing equations . . . 13
2.2 Equations for viscose turbulent flow . . . 14
2.2.1 Reynolds-Averaged Navier-Stokes Equation . . . 14
2.2.2 Resolving turbulent structures by Detached Eddy Simulation . . . 16
2.3 Equations for invsicid and irrotational flow . . . 17
2.4 Numerical flow solution . . . 18
2.4.1 Finite volume method . . . 18
2.4.2 Boundary element method . . . 20

3 Numerical Framework **27**

3.1 Motion solver . . . 27
3.2 DP controller . . . 31
3.3 Allocation . . . 32
3.4 Integrated platform for closed-loop DP simulation . . . 33

4 Wind loads in DP operations **37**
4.1 Implementation of wind loads in the DPTool . . . 37
4.1.1 Dynamic wind speed and direction . . . 38
4.1.2 Coefficient based wind loads . . . 41
4.2 Experimental approach . . . 43
4.2.1 Experimental setup . . . 44
4.2.2 Preconditions . . . 45
4.2.3 Results of the wind tunnel experiments . . . 49
4.3 Numerical assessment of wind loads . . . 57
4.3.1 Numerical setup . . . 58
4.3.2 Computational domain . . . 58
4.3.3 Mesh grid study . . . 59
4.3.4 Influence of wall function . . . 62
4.3.5 Influence of the domain size . . . 63
4.3.6 Influence of wall shear stress at test section floor . . . 64
4.3.7 Scale effects . . . 68
4.3.8 Influence of transient and turbulent flow . . . 70
4.4 Comparison of wind load coefficients from CFD and experiments . . . 70
4.5 Discussion . . . 73

5 Current loads **75**
5.1 Implementation of current loads in the DPTool . . . 76
5.2 Experimental approach . . . 77
5.2.1 Experimental setup and procedure . . . 77
5.2.2 Modal analysis . . . 78
5.2.3 Results . . . 79
5.3 Numerical approach . . . 81
5.3.1 Numerical setup . . . 81
5.3.2 Turbulent effects in the flow around ships . . . 84
5.3.3 Influence of the tank walls . . . 88
5.3.4 Influence of free surface . . . 88
5.4 Comparison of current load coefficients from CFD and experiments . . . 89
5.5 Discussion . . . 91

6 Wave loads **93**
6.1 Implementation of wave loads in the DPTool . . . 93
6.2 Experimental approach . . . 95
6.2.1 Experimental setup . . . 95
6.2.2 Influence of wave steepness on wave drift force . . . 97
6.3 Numerical approach . . . 98
6.3.1 Linear strip method . . . 99

6.3.2 Three dimensional panel method . . . 100
6.3.3 Field method for viscous flows . . . 101
6.4 Comparison of numerical and experimental results . . . 103
6.4.1 Ship motion . . . 103
6.4.2 Wave loads . . . 104
6.5 Discussion . . . 105

7 Application **107**
7.1 Allocation . . . 107
7.2 Setup of the controller . . . 108
7.3 Verification maneuvers . . . 111
7.4 Static and dynamic assessment . . . 115

8 Conclusion and perspectives **117**

Bibliography **121**

Nomenclature

The following notation is adopted throughout the thesis, unless otherwise explicitly stated. It is not exhaustive. Any other notation introduced will be defined when required.

Latin symbols

$\mathbf{a}(\omega)$	:	Frequency-dependent sectional added mass matrix
$\mathbf{b}(\omega)$	:	Frequency-dependent sectional damping matrix
d_L	:	Linear roll damping factor
d_Q	:	Quadratic roll damping factor
$\vec{f}_x(\dot{\vec{\xi}})$	:	Sectional hydrodynamic force vector
p	:	Dynamic pressure
u_c	:	Current velocity
u_{10}	:	Mean wind velocity speed at a height of 10 m above reference level
v_w	:	Wind velocity
$\mathbf{A}$	:	Hydrodynamic added mass matrix
AL	:	Lateral area of superstructure above waterline
$\mathbf{B}$	:	Hydrodynamic damping matrix
Bft	:	Beaufort wind scale
C_{Dy}	:	Horizontal sectional drag coefficient
C_{Dz}	:	Vertical sectional drag coefficient
$F_\xi(\dot{\xi}_0)$	:	Longitudinal damping force
L_{OA}	:	Length over all
L_{PP}	:	Length between perpendiculars
$\mathbf{M}$	:	Rigid body mass matrix
M_ϕ	:	Viscose quadratic roll moment
$\mathbf{S}$	:	Restoring force matrix
T_x	:	Sectional draft
B_x	:	Sectional beam

Greek symbols

$\epsilon(t)$	:	Wind direction angle
$\hat{\zeta}$	:	Complex wave amplitude
η	:	Position and heading vector of vessel
λ	:	Wave length
μ_s	:	Seaway encounter angle
μ_w	:	Wind encounter angle
μ_c	:	Current encounter angle
ν	:	Velocity rates of vessels motion
$\vec{\xi}$	:	Motion vector
τ	:	Retardation time
τ	:	Allocation force vector
ω	:	Motion frequency
ω_e	:	Frequency of encounter

Abbreviations

API	:	American Petroleum Institute
CFD	:	Computational Fluid Dynamics
DES	:	Detached Eddy Simulation
DP	:	Dynamic Positioning
EFD	:	Experimental Fluid Dynamics
ERN	:	Environmental Regulatory Number
$FMEA$	:	Failure Mode Effect Analysis
FVM	:	Finite Volume Method
HIL	:	Hardware-in-the-Loop
$IDDES$	:	Improved Delayed Detached Eddy Simulation
$IMCA$	:	International Marine Contractor Association
LES	:	Large Eddy Simulation
$RANSE$	:	Reynolds-Average-Navier-Stokes Equation
SIL	:	Software-in-the-Loop
VSP	:	Voith-Schneider Propulsor

List of Figures

1.1 Total capacity of installed wind farms from 2012 to 2022 [40] and [22] 1
1.2 Geometry and sectional discretization - left: Offshore Supply Vessel, right: Tug . 10

3.1 Scheme of the DP simulation time loop 27
3.2 Added mass and damping of the roll motion for the OSV in frequency domain (left) Retardation function $B(\tau)$ for a single impulse of the roll motion (right) . . 28
3.3 Experimental and numerical decay test $\varphi_0 = 9.64°$ 30
3.4 (a)Voith Schneider Propulsor [88], (b)Radial Propeller [87], (c)Inline Thruster [86] 32
3.5 Sketch of VSP driving pitch and rudder pitch [47] 32
3.6 Sketch of the project management platform of the *DPTool* 34
3.7 GUI of the *DPTool* job manager 35

4.1 Comparison of Frøya and Davenport wind spectrum for wind of Beaufort 5 . . . 39
4.2 Wind velocity (top), wind encounter angle (bottom) 40
4.3 Coordinate system of wind forces and moments 41
4.7 Sketch of wind tunnel [39] 43
4.8 Model of an OSV (top) and a tug (bottom) mounted in the wind tunnel 44
4.9 Sketch of test section and location of the shear flow measurements on the floor . 45
4.10 Comparison of the mean velocity in the boundary layer of the wind tunnel test section at pivot point (x=0.0m) 46
4.11 Arrangement of the pitot tubes for measuring the velocity profile on the deck house of the OSV model (left), polar diagram of the normalized velocity distribution (right) 48
4.12 Visualization of the TUG model boundary flow 49
4.13 Visualization of turbulent flow at the tug's funnel (left), wake behind the deck house of the OSV (right) 49
4.14 Time series of transverse wind loads 50
4.15 Effect of angle increment (left), effect of sense of rotation (right) 51
4.16 Absolute deviation from repeated measurement of wind loads at $v_w = 20m/s$ (OSV) 52
4.17 Absolute deviations of the force measurements in repeat measurements (TUG) . 53
4.18 Tug in heel condition 54
4.19 Influence of heeling on the wind load coefficients 54
4.20 Absolute deviations of the force coefficients due to heeling influence 55
4.21 Crane arrangement on main deck 56

4.22 Influence of a working crane on the wind load coefficients 56
4.23 Flow field around superstructure of an offshore supply vessel 57
4.24 Computational domain and boundary condition 58
4.25 Comparison of hexahedral and polyhedral performance for 45 deg 59
4.26 Comparison of wind load coefficients for $\epsilon = 45deg$ (left), CPU performance of different mesh types (right) 60
4.27 Grid study of both mesh types 60
4.28 Grid configuration with polyhedron cells (top) and tetrahedron cells (bottom) . . 61
4.29 Side view of prism layer grid 62
4.30 Cell distribution of Y+ 62
4.31 Y+ value with varying incident flow velocities and constant boundary layer grid 63
4.32 Variation of domain size with an oblique headwind 64
4.33 Mesh configuration of test section floor 64
4.34 Comparison of wind profile 65
4.35 Pressure distribution in beam wind with non-slip condition (top) and without (bottom) (OSV) 66
4.36 Pressure distribution in beam wind with non-slip condition (top) and without (bottom) (TUG) 67
4.37 Scale effects of the wind load coefficients of the OSV for varying encounter angles 68
4.38 Reynolds effects in head winds and deviation of shear and pressure share of the total load 69
4.39 Comparison of the longitudinal velocity distribution in head winds between steady state RANS (bottom) and DES (top) 69
4.40 Comparison of wind load coefficients with experiments (OSV) 71
4.41 Comparison of wind load coefficients with experiments (TUG) 72
4.42 DP set point assessment for winds encountering from $\epsilon = 135deg$ - ship motion (left), required power (right) 73

5.1 Turbulent flow around hull exposed in oblique current flow 75
5.2 OSV model mounted below the carriage(a), 6DOF load balance (b) 78
5.3 Fourier transform of a modal analysis of the experiment setup 79
5.4 Measured forces in tank fixed coordinate system $(\mu_c = 75deg), v_c = 0.7m/s$ . . . 79
5.5 Current loads in tank reference system 80
5.6 Velocity dependency of current load coefficients 80
5.7 Vortex development on the hull in current flow - $\mu_c = 90$ deg, $v_c = 0.5$ m/s . . . 81
5.8 Grid study of current loads 82
5.9 Domain setup for current loads (top), mesh refinement and prism layers (bottom) 83
5.10 Visualization of vortical structures in current flow 85
5.11 Pressure distribution RANS simulation (top), velocity in symmetry plane (bottom) 86
5.12 Pressure distribution DES simulation (top), velocity in symmetry plane (bottom) 87
5.13 Normalized velocity with tank walls (left) - without tank walls (right) 88

5.14 Visualization of the free surface with current flow ($\mu_c = 75deg$, $v_c = 0.7m/s$) . . 89
5.15 Results of numerical methods and experiments in ship fixed coordinate system . 90
5.16 DP set point assessment for currents encountering from $\epsilon = 135deg$ - ship motion (left), required power (right) 91

6.1 Wave elevation and wave envelope of a Pierson Moskowitz Seaway with 12.7 sec and 2.5 m 94
6.2 Drift forces in time domain for μ=135 deg 95
6.3 Sketch of the experimental setup for measuring the wave drift forces 96
6.4 Measured heave (top) and pitch motion (bottom) in head waves under consideration of different wave steepness 97
6.5 Measured drift forces in head waves under consideration of different wave steepness 98
6.6 Response Amplitude Operators of the drift forces in head waves under consideration of different wave steepness 98
6.7 Volume fraction and overset mesh 102
6.8 Simulation of the ship motion and forces for a wave length of $\lambda/L = 0.6$: (left) surge motion, (center) wave elevation, (right) longitudinal forces 102
6.9 Response amplitude operator in quartering head waves 103
6.10 Comparison of wave drift loads in quartering head waves 104
6.11 DP set point assessment for waves encountering from $\epsilon = 135deg$ - ship motion . 105
6.12 DP set point assessment for waves encountering from $\epsilon = 135deg$ - required power 106

7.1 Typical thruster arrangement of the OSV model 107
7.2 Comparison of footprint between allocation set with azimuth thruster (left) and VSP (right) 108
7.3 Identified trajectory of standard identification procedure 109
7.4 Controler setup (left) and example of a footprint (VSP) with LQ parametrization for Beaufort 5 encountering from beam side 110
7.5 Filtered motion by extended Kalman filter algorithm 110
7.6 GUI for parameter input for the observer and wave filter design 111
7.7 DP simulation environmental loads encountering from 135 deg (BFT 5) 111
7.8 DP simulation environmental loads encountering from 135 deg (BFT 5) 112
7.9 Resulting ship motion of DP simulation with encountering loads of 180 deg at Bft 6 113
7.10 Resulting environmental loads in time domain for a DP simulation of Bft 6 with encountering direction of 180 deg 113
7.11 Allocation forces of propulsion plants for Bft6 and encountering direction of 180 deg 114
7.12 Resulting control parameter of VSP and bow thruster 114
7.13 Comparison between static and dynamic capability in a polar diagram (VSP allocation) 115

8.1 Froude Krylov and diffraction force λ/L_{PP}=1.0 129
8.2 Added mass matrix **A** of OSV in model scale [$t\ m^2$] 131
8.3 Damping matrix **B** of OSV in model scale [$t\ /\ s^2$] 133
8.4 Ship motion in regular waves - μ =135deg, λ/L_{PP}=1.0 135
8.5 Response amplitude operator in following waves 136
8.6 Response amplitude operator in quatering following waves 137
8.7 Response amplitude operator in beam waves 137
8.8 Response amplitude operator in quatering head waves 138
8.9 Response amplitude operator in head waves 138
8.10 Comparison of wave drift loads in following waves ($\mu_w = 0°$) 139
8.11 Comparison of wave drift loads in quatering following waves ($\mu_w = 45°$) 140
8.12 Comparison of wave drift loads in beam waves ($\mu_w = 90°$) 140
8.13 Comparison of wave drift loads in quatering head waves ($\mu_w = 135°$) 141
8.14 Comparison of wave drift loads in head waves ($\mu_w = 180°$) 141

List of Tables

1.1 Principale dimensions of VSP vessels 10

4.1 Reference dynamic pressure 41
4.2 Principal dimensions of the wind tunnel models 43
4.3 Mean height of the lateral wind area 47
4.4 Mean wind loads 50
4.5 Comparison between RANS and DES results for head winds 70
4.6 Required power during set point analysis 73

5.1 Principle dimensions of the OSV model 77
5.2 Comparison of transversal current coefficients CY 84
5.3 Mean percentage deviations from the experiment 90
5.4 Required power during set point analysis 91

6.1 Calibration of the undisturbed waves in the wave tank 96
6.2 Required power during set point analysis 105

7.1 Thruster configuration 108
7.2 Required power during set point analysis 112
7.3 Environmental parameter according to [23] 116

1 Introduction

Due to the continuous growth of the industrial utilization of coastal and offshore waters during the past years, Dynamic-Positioning systems (DP systems) have become a natural component of new delivered modern offshore vessels in the maritime industry. One of the reasons for this development is the reorientation of energy production from using fossil fuels and nuclear sources to renewable energy sources, e.g. offshore wind power as well as current and wave energy. Figure 1.1 illustrates the enormous expansion of Germany's wind power capacity and compares the growth with the world.

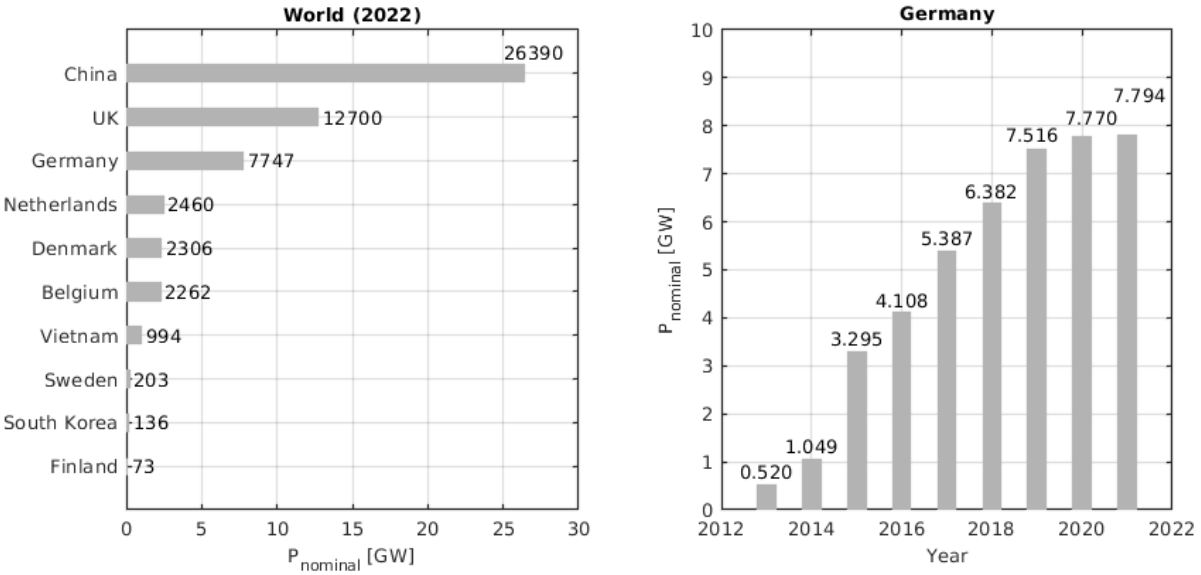

Figure 1.1: Total capacity of installed wind farms from 2012 to 2022 [40] and [22]

At the same time the oil and gas production farms outreach to more deep water sea areas. Along with the installation and maintenance of offshore installations, the demand of special crafts and platforms is increasing. Herein, the diversity of ship types and functions of DP systems is manifold. The erection and installation of new offshore wind parks e.g. employs the following typical DP vessels: Jack-up vessels, tug boats, diver support vessels, cable layer, offshore supply vessels and crew transfer vessels.
It can be stated that the market of the oil and gas as well as the wind park offshore industry is increasing. The demands for sophisticated DP systems accumulates also for passenger vessels and yachts.

1.1 Motivation

To assure safe and efficient offshore operations, many vessels have to be equipped with sophisticated DP systems. A high positioning accuracy of the system must be ensured for operations where multiple structures and vessels work together in a limited area. The reliability of all components must be guaranteed for crew transfer situations. Therefore, a standard of redundancy has to be considered in the design of DP systems. Further, modifications of the controller may enhance a lower fuel consumption and thus lower emissions.
In order to compare and evaluate the capability of Dynamic Positioning systems and for the reason of approving for DP systems for specified offshore operations, class societies, ship owners and charterers established 1977 the environmental regularity numbers (ERN) that result from static analysis. Herein, the maximum available thrust in specified directions is evaluated against the wave drift forces, a constant wind and current force. This procedure neglects all dynamic effects arising from non-steady external loads as well as the dynamics of the propulsion plant and control systems itself. However, the consideration of the dynamic behavior of the acting forces is essential for secure offshore operations and for defining the limits in keeping position and heading angle as well as accelerations. Therefore, a time-domain approach, including dynamic modeling of wave, current and wind loads, is most suitable for analyzing the dynamic positioning capability of ships. In the year 2016 a new standard has been introduced (e.g. DNVGL-ST-0111 - Assessment of Station Capability of Dynamic Positioning Vessels), that allows a consistent definition of three building upon each other levels: static, semi-static and time depended.
In contrast to the static DP assessment the capabilities of DP simulations in time domain are immense:

- The use of time varying wave, wind and current loads allow the simulation of the vessel in a realistic environment. Further, specific sea area characteristics can be considered to evaluate the risk for a defined DP operation.

- The DP capability can be quantified by overlaying the simulated trajectory with a limiting watchcircle and heading.

- The simulation of time varying forces and the controlled reaction of the actuators allows a detailed assessment of the individual influences. Herein, different controller parameter and design approaches in sense of efficiency can be studied.

- The consideration of an realistic environment with all specific forces of the actuators allow the development of a specific thrust allocation logic tailored for the propulsion system.

- The controller parameter of the DP system can be pre-configured by a numerical system identification under consideration of the specific forces acting on the vessel.

- The development of a Dynamic Positioning system is very complex due to its integrity of a large number of system components. In order to improve the reliability of the DP system the time-domain simulation may be implemented into a Software/Hardware-in-the-Loop (SIL/HIL) system. This allows a consideration of all components (sensors, actuators and power generators) in a failure mode effect analysis (FMEA).

The above listed advantages express the need for research and progress in developing time domain methods. To consider both, station keeping and seakeeping aspect from an early design stage, it is first necessary to evaluate and study properly the methods that can be used for preliminary station keeping analysis. A particular emphasis should be given on the environmental loads acting on the vessel and its modeling in such a way to ensure homogeneity and coherence between dynamic positioning and seakeeping calculations. Therefore, the aim of the thesis is both, the development of a method in time domain with all relevant components, as well as the experimental and numerical study of methods to account for realistic environmental forces.

1.2 Review on previous work

The research of numerical methods for DP simulation in the maritime industry represent a diverse field of study. Therefore, the review on previous work categorizes in both, the numerical treatment of DP simulation as well as the methods that allow the prediction of the environmental loads. The following subsections elaborate the state of the art of each field.

1.2.1 Simulation of dynamic positioning maneuvers

Today's applications of DP simulations range from static procedures for the early design stage up to high sophisticated simulation in time domain for unique defined DP operations. Further, DP simulation find their application in pre-operation testing and operational training, i.e. Hardware-in-the-Loop (HIL) to secure a problem-free installation of the system or real time simulators for the education to enhance the skills of the crew.
First simulation models for DP vessels were developed in the 1980's. These models only included low frequency loads and motions in the horizontal plane, e.g. van den Boom et al. [13] and Nienhuis et al. [61]. Further developments by Aalbers et al. [1] extended the scope to combined low and wave frequency motions. Modern simulation methods are time domain based and include all relevant DP-System components (e.g. filter, controller, allocation), i.e. the model is 6 degrees of freedom, includes a Kalman filter for filtering high-frequent mean free ship motion, uses a PID controller and a Lagrange optimized allocation algorithm (compare Serraris [75]). Donnarumma et al. [24] published a case study for the design and validation of dynamic positioning for marine systems. The motion of the vessel has been represented as the superposition of wave-frequency (theory on low frequency second order wave exciting forces by

Pinkster [67]) and low-frequency components (manoeuvering model by Oltmann and Sharma [66]). The wind and current loads were accounted by two sets of three coefficients evaluated for head, lateral and bow quartering encounter angles respectively. At the end simulation results and sea trial measurements were compared.
The most common practise is the representation of the dynamic capability in a wind envelop revealed by a static approach. Herein, the environmental condition of wind, current and wave loads is related to the acting wind speed. This is done for different angles of attack from which the environmental loads can appraoch the vessel, but is at least calculated once every 15° according to the International Marine Contractor Association (IMCA) guidlines [37]. In the static approach, the evironmental loads and the thruster forces are accounted to act colinear which may lead to overestimates of the vessels capability (compare Smogeli et al. [78]). The work of Van't Veer and Gachet [83] introduced a quasi-static approach, that relies on the benefits of a fast calculation method but considers fluctuating environmental loads by a statistical factor. The corrections take place for the wave drift force, and is therefore denoted as wave drift multiplier. Antheunisse et al. [6] published Force Multiplication Factors (FMFs) dependent on specific DP offset requirements. Another approach is the introduction of the Dynamic Margin which is introduced by the American Petroleum Institute (API)[72]. The method provides an allowance of 80% of the maximum thruster loads to account for the varying environmental loads. Lübcke et al. [52] presented a simplified time domain approach in such a way to include directly dynamic effects of wind and current by subsequent steps from static calculation into time domain.
Dynamic DP simulations improve the ongoing research in the offshore industry. Wichers et al. [90] describes the procedure used to investigate the thruster-hull and thruster-thruster interaction and the automatic closed loop control system as used for the computer simulations and model tests.

1.2.2 Wind loads on ships

The research of wind loads on ships and offshore structures started in the early 1920s. Aerodynamic resistance and wind effects have been considered in naval architecture as regards large ship superstructure influence on propulsion and maneuvering.
First basic emperical formulations are developed by Hughes [36] and modified by Taylor [79] to account for the wind resistance. The formulation adopted basic forms from flight aerodynamics for the superstructure. First multiple regression analysis for wind coefficients, as function of vessels geometric characteristics, was given by Isherwood [41]. The transversal and lateral force, together with the yaw moment considered the type of superstructure that is fitted on the hull. More details to that approach have been added by Gould [31]. Since the need for wind loads at this time dominated by typical merchant vessels, the elaborated methods are not suitable for today's DP vessels.
Blendermann [10] and [11] conducted in his work a large number of experiments of different

types of vessels, including offshore ships. In further development, the measurements were used as a database and analyzed as statistical data.
With the development of the computational rescources more and more research can be found in the direct simulation of the wind loads. As an example of recent research, Wilde et al. [91] simulated the wind loads of a complex superstructure of a FPSO with a large computational mesh with around 30 mio. cells. A comparison with experiments found a systematic error of 5%-10%. Another study to investigate the suitability of CFD methods for etimating the wind loads has been published by Janssen et al. [42]. In the underlaying experimental study (Andersen [4]), a container ship model was loaded with different configurations and the wind loads were measured for all encounter angles. For the CFD approach a tree-dimensional steady RANS numerical setup has been applied. The computational domain has been set according to the configuration of the wind tunnel experiments. The impact of geometrical simplifications has been analyzed on different grid sizes ranging from 1.5 mio. to 3.9 mio. cells. The absolute difference in relation to the measured loads varied between 37.9% for a coarse representation of the ship (simple-box shaped) to about 5.9% for the most detailed model.
Besides approaches of direct simulation of the loads, Haddara and Soares [32] proposed a procedure applying neuronal networks by using the input layers parameters similar to Isherwood. Further investigations were conducted by Valčić and Prpić-Oršić [82] using the parameters according to Blendermann. The studies showed a promising approach, however a large database is needed to improve the accuracy.

1.2.3 Current loads on ships

In contrast to wind loads, the research on current loads is dominated by CFD computations rather than regression methods based on experimental data. Both, the numerical and experimental investigation of the flow around the ship hull has been published by many researchers. Among others, Nienhuis [61] presented model test data for five vessels including an offshore supply vessel. Sen and Vinh [85] published a mathematical model to predict the current loads for ship simulator using the cross-flow principle. Empirical formulations for the current force are introduced by DNV-GL [23] and API-RP2SK [72]. Recently CFD was applied to the prediction of current loads, initiated by the Current-Affairs Joint Industry Project (JIP). The CFD current loads obtained in this JIP were validated against model test data, and found to correlate well, Vaz et al. [84] and Fathi et al. [26].
Special needs for current loads developed for mooring operations of tankers and the flow around offshore platforms. Meneghini et al. [56] investigated the flow interference between two circular cylinders for different arrangements. The effects of vortex introduced vibrations of an elastically mounted rigid circular cylinder in steady current is studied in the research of Oliveira[65].
The research resulted in the development of different methods and approximations. Earlier work was related to slender ship geometries. Today's research is concerned with the flow around bluff bodies. This is due to the development of the increasing sizes of the ships, as well as the im-

provements in the computer performance, that allow such assessment. Hence, according to the required degree of accuracy, state of the art of considering current loads is the use of empirical formulation, data of similar ship types or direct simulation as well as the conduct of experiments for specific ships.
Based on a great number of model tests of moored tankers, Remery and Van Oortmerssen [70] presented a method to predict current forces. However, due to the insufficient accuracy of the measured small longitudinal forces, the method considers the ITTC-1957 frictional resistance formula. Mercier and Huijs [58] investigated the steady current forces on a tanker-based FPSO in experiments. The model was mounted on a six-axis load scale below a tank fixed bridge. The current flow has been modeled by a multi-port jet type current generator. Dynamic force variations were detected and compared against the method proposed by Remery and Van Oortmerssen. The standard deviation of the lateral force was 33% and for the longitudinal force 129% of the mean value. Spectral analysis of the time series indicated high frequency (3 Hz) inertial oscillations of the model. Further primary sources of temporal variability indicated vortex shedding and wake flow interaction.
In a recent publication of Koop et al. [46] regarding current loads on an FPSO obtained from CFD computations a maximum error of 10% from model tests was presented. Two different approaches were used: a steady type of simulation with SST $k-\omega$ turbulence model and an unsteady simulation using DES method with IDDES sub-grid model. It is shown that, compared to the steady approach with a variance of 5% in case of the SST $k-\omega$ turbulence model, the unsteady IDDES method produced more varying results due to its sensitivity to the mesh structure and its refinements.
Arslan et. al [7] investigated the unsteady flows around different ship sections using CFD with large-eddy simulation (LES) sub-grid scale turbulence model. The work focused on the motion of vortex structures generated by separated flow.

1.2.4 Wave drift loads on ships

The wave drift loads are known as second-order wave forces. While first-order wave loads oscillate harmonically with a mean period value of zero, the mean second-order wave loads produce a steady time-averaged mean offset that exerts drift motion. The drift loads play a major role in DP. Due to the immense number of necessary computations with varying wave periods, heights and encounter angles, the research on wave drift loads is primarily concerned with methods in frequency-domain, hence potential theory is used.
Accoring to Clauss et al. [16] the determination of wave drift loads can be split in two general approaches. The first approach deals with the computation of the velocity potential and further the integration over the boundaries that are far away from the body. This method can be used only for single harmonic waves (smooth airy waves with constant wave period). The second approach applies the direct integration of the pressure potential up to second-order over the actual wetted surface of the ship hull.

Most common proceedures for the computation of the wave drift loads in DP simulation are based on a priori determined frequency-domain results. Men et al. [55] computed the second-order wave drift forces by linear summation through the second-order force Response Amplitude Operators obtained from similar vessel database. Smogeli et al. published in [78] and [60] their DynCap methodolgy based on direct pressure integration which includes the full geometry of the specific hull while using a three-dimensional Boundary Element Method to solve the velocity potential. Here, the commercial software WAMIT [38] is used. Augener and Krüger [8] have shown in their work that the potential methods such as strip theory can be a very fast and reliable method for predicting wave drift forces and moments. Deciding for selecting an appropriate method for calculating the wave drift forces, is the applicability of the slender body theory. While wave drift loads for slender offshore vessels may be determined by a simple strip method the forces for e.g. tug supply vessels have to be computed by a three-dimensional approach.
One of the first publications on wave drift forces and moments was elaborated by Maruo [54]. Here, a three-dimensional far-field method is presented for a single ship with zero forward speed in the horizontal plane. The conservation of fluid momentum and the slender-body theory was applied by Newman [59]. Salvesen [73] extended the work of Newman by establishing a hull pressure integration method.
For time domain approaches it is necessary to compute the real-time total wave drift forces. Pinkster [67] proposed using the direct relationship between low frequency wave force and relative motion around the ship. This approach has been improved by Aalbers et al. [2], [3] and Quadvlieg et al. [69]. Another direct pressure integration method for bodies with forward speed is developed by Faltinsen et al. [25].
A simple method to estimate the added resistance in waves, and hence the wave drift loads, is proposed by Boese [12]. In this method, the wave drift loads are obatined by two shares. First, the pressure is integrated up to the still water line. The second share accounts the harmonic pressure variation along the wetted waterline. Söding and Bertram [9] extended this method by the transverse wave drift force and the mean yaw moment.
When the wave lengths are small compared to the ship length, the exerted ship motion due to the waves become negligible small. Hence, the dominating share of the wave drift forces changes from motion excited forces to forces exerted by the reflection of the incident waves. Faltinsen et al. [26] published an asymptotic theory that accounts the energy of a reflecting wave at the exposed waterline on the incoming side of the waves.

1.3 Present work

Cycloidal propulsors, such as Voith-Schneider Propulsors (VSP), have the ability of controlling full thrust in any direction in very short reaction times and is therefore very suitable for DP operations. Hence, the objective of this work is to develop a state-of-the-art closed loop simulation platform for the assessment of the DP capability of typical DP vessels with VSP. The

simulation platform allows the following functions:

- Computation of hydrodynamic forces for introducing ship motion in arbitrary seaways
- Approximation and organization of numerical, experimental and empirical databases of wind and current loads
- Development of an allocation setup with cycloidal propulsors, podded azimuth and bow thruster
- Design and parametrization of DP controller optimized for the specific vessel and allocation
- Simulation of ship motion in a seaway in consideration of thruster forces and environmental loads in time-domain
- Simulation of static and dynamic DP capability plots for the assessment and evaluation of the vessel's performance

For the consideration of ship motion the method IMPRES developed and published by Detlefsen et al. [20] was used. This efficient numerical method allows the simulation of ship motions in waves under arbitrary external loads in time domain. The method is based on impulse-response-functions. Herein, the hydrodynamic forces acting on the vessel are computed by the application of efficient frequency domain based boundary element methods. Wave forces of first and second order are either obtained by the two-dimensional strip method PDSTRIP or by the three-dimensional panel method ANSYS AQWA. The wave forces are then transferred into time averaged drift force variation. Current loads are modeled by coefficients, which can be derived from empirical formulations, model tests or numerical simulations. Spectral descriptions of wind velocity and direction are used to generate fluctuating wind in time-domain. The wind forces are then computed by using coefficients.
The simulation platform has been integrated in MATLAB/SIMULINK using the MEX interface. Other components, i.e. the DP controller and Allocation of the dynamic positioning system, are then integrated in a SIMULINK model.
The dynamics of maneuvering devices, e.g. VSP and bow thrusters, are modeled as well as PID controllers and wave filters. From the obtained time series of position and heading deviations, power consumption etc. the station-keeping capability can be evaluated by means of different criteria. The dynamic positioning capability for all encounter angles is the concluded in a polar diagram.
Main features that are implemented in the platform were published by Detlefsen et al. [21] and Koschorrek et al. [48].

1.3.1 Contributions in the present work

The contributions of the present work can be summarized by the following:

- Cycloidal propulsors, e.g. VSPs, have the deciding advantage of generating accurate thrust in every required direction and at the same time the ability to change the maximum thrust from one direction into another within a few seconds. This feature is very advantageous for DP operations. The development of the current work of the DP simulation platform allows a tailor-made parametrization of the DP controller.
- A great number of experiments of a tug boat and an offshore supply vessel in the wind tunnel of the "Institute for Fluid Dynamics and Ship Theory" and in the towing tank of the "SVA-Potsdam" have been proceeded. The results provide a good basis for validating the numerical methods.
- Various numerical methods were applied to typical DP vessel with VSPs to determine the wind and current forces. In order to account turbulent viscose flow, different turbulence models were investigated. A fundamental comparison among steady-state RANS, unsteady RANS and Detached-Eddy-Simulation (DES) revealed insights of turbulent flow on the integral forces. In conclusion this work demonstrates numerical setups for the environmental loads with the reliability and accuracy in engineering practice. The setups are validated against experiments.
- The wave drift forces were obtained from three different numerical methods: a two dimensional strip method, a three-dimensional panel method and a Finite-Volume Method applying the Euler equations. The comparative study was checked with experiments conducted in the towing tank of the "SVA-Potsdam".
- With the implementation of a holistic approach of DP simulation, the influences of the individual environmental loads can be studied. Due to their different impacts compared to the total loads, uncertainties of a single component have different effects on the total performance of the DP simulation.
- Quantification of the effect of approximated current loads and vessel specific determined coefficients in DP simulation
- Application purposes are assigned to an offshore supply vessel

1.3.2 Introduction of typical DP vessels using VSP

Two typical ship designs for DP operations have been used in the work for experimental and numerical study. The main dimensions of a tug boat (TUG) and an offshore supply vessel (OSV) are summarized in Table 1.1. The design of the superstructures and the ship lines are illustrated in figure 1.2. The TUG includes two VSPs located at a section forward of the deck

house. The OSV is equipped with two VSPs at the ship end and two bow thruster in the bulbous bow section.

Table 1.1: Principale dimensions of VSP vessels

			TUG	OSV
Length over all	L_{OA}	$[m]$	$\approx$ 37.50	$\approx$ 85.30
Breadth over all	B_{OA}	$[m]$	14.00	19.20
Design Draft	T_D	$[m]$	4.10	5.20
Volume molded	∇	$[m^3]$	1 245	4 820

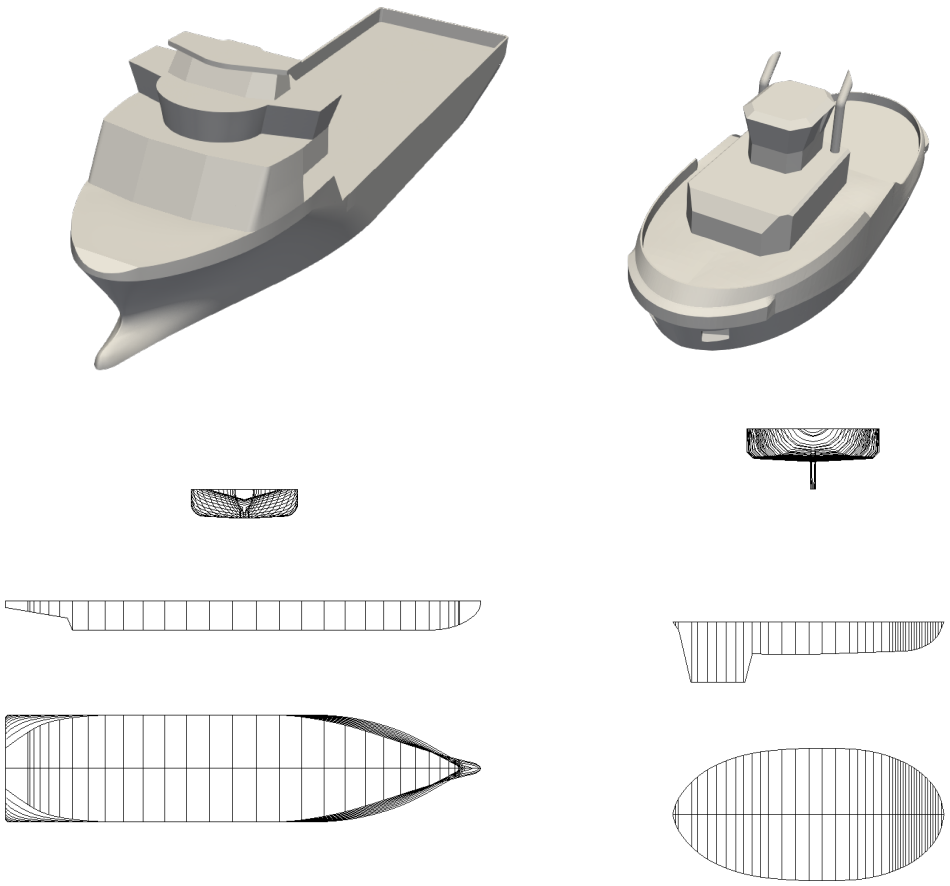

Figure 1.2: Geometry and sectional discretization - left: Offshore Supply Vessel, right: Tug

1.3.3 Layout of the thesis

The outline of the present thesis is divided into the following chapter:

Chapter 2 - Fundamentals introduces the governing equations and their numerical treatment which are involved in the further elaboration of DP simulation and its environmental loads. The chapter is divided into equations to model viscose turbulent flow and inviscid irrotational flow. Further, the numerical flow solution applying the Finite-Volume-Method and the Boundary-Element-Method is described.

Chapter 3 - Numerical framework describes the holistic approach of the DP simulation platform *DPTool*. Herein, the transfer from frequency-domain motion into time-domain motion using the impulse-response-functions is presented. Further, the treatment of the controller algorithm and the allocation is described.

Chapter 4 - Wind loads is concerned with the experimental and computational assessment of wind loads. At first, the procedure and the results of experiments in the wind tunnel are presented. Prior the experiments, the velocities of the natural boundary layer on the test section have been evaluated at different positions and velocities. The effect on the wind load coefficients were discussed and compared with CFD results. Measurements of the velocities on top of the wheel house and smoke tests in combination with laser sheets outlined the complex flow around the superstructure. For CFD analysis different numerical solvers were applied. Together with a grid study, a high performance simulation setup is elaborated. The chapter closes with a conclusion of the impact of differing wind load coefficients on the DP simulation.

Chapter 5 - Current loads contains the description of the experimental setup and the evaluation of experiments for the determination of flow forces, as well as the numerical simulation. A CFD study applying different turbulence models reveals the impact of turbulent flow. Further, the CFD assessment includes the investigation of blockage and free surface effects.

Chapter 6 - Wave loads outlines the challenges for both, the experimental and numerical determination of wave drift forces. The experimental setup is described and the influence of different wave steepness is investigated. Three different numerical methods are compared with the experimental results.

Chapter 7 - Application shows the usability of the *DPTool* in form of a DP capability analysis for an offshore supply vessel. The workflow includes all methods that are presented in the previous chapters. A comparison between a static capability and a dynamic DP simulation in time-domain outlines the various applications and pre- and postprocessings that are established by the holistic approach of the current thesis.

Chapter 8 - Conclusion and perspectives resumes the current work. A brief summary is given and future research topics are suggested.

2 Fundamentals

The numerical prediction of a vessel's DP capability in time-domain under arbitrary environmental loads require individual methods for calculating the flow of each load component and therefore distinct theories of fluid dynamics are employed. While common approaches for the simulation of ship motion in a seaway may neglect viscous and rotational flow effects, for the air flow around the superstructure of the ship as well as the flow around the underwater hull turbulent effects have to be accounted.
This work includes a comparison between numerical methods for each environmental load, i.e. the treatment of turbulence. Therefore, this chapter provides in general the description of fundamental equations and the numerical solution methods. Whereas, details of the numerical setups resulting from the individual requirements are decribed in the corresponding sections. The following methods for viscose flow are implemented in the PLM software Simcenter Star-CCM+ (version 11.06 [77]) and the potential methods are covered by the 2D strip method PDSTRIP (version 2014-12 [9]) and the 3D panel code ASYS AQWA (release 16.0 [5]).

2.1 Governing equations

The computational methods to describe the flow characteristics are based on the Navier-Stokes equations. The flow underlays the principle of conservation of mass and momentum.
The continuity equation which preserves the conservation of mass states, that any amount of flow enters the computational domain flows out at the same time. For a control volume V with its boundaries S the integral form is revealed by:

$$\int_V \frac{\partial \rho}{\partial t}\, dV + \oint_S (\rho \hat{u}_i)\, dS_i = 0. \tag{2.1}$$

Herein ρ denotes the density, $\hat{u}_i$ represents the vector of the instantaneous velocity components in Cartesian coordinates $i = 1, 2, 3$.
The conservation of momentum states that the sum of momentum and flux convection inside the computational domain is caused by external forces that act on the domain:

$$\int_V \frac{\partial (\rho u_i)}{\partial t} dV + \oint_S (\rho u_i \hat{u_j})\, dS_j = \oint_S \sigma_{ij}\, dSj + \int_V f_i dV \tag{2.2}$$

where σ_{ij} is the surface stress tensor and f_i describes the volume specific forces acting on the fluid. The stress tensor can be expressed in terms of the hydrostatic pressure $p\delta_{ij}$ and a viscose

deviator τ_{ij}:

$$\sigma_{ij} = \tau_{ij} - p\delta_{ij} \tag{2.3}$$

The viscous stresses of Newtonian fluids are modeled dependent on the strain-rate-tensor $s_{ij} = \nabla u_i$ and the dynamic viscosity μ:

$$\tau_{ij} = \mu\left(\frac{\partial u_i}{\partial x_j} + \frac{\partial u_j}{\partial x_i}\right) \tag{2.4}$$

All conservation equation can be written in form of a generic transport equation:

$$\int_V \frac{\partial(\rho\phi)}{\partial t} dV + \oint_S (\rho\phi\hat{u}_j) dS_j = \oint_S \Gamma \frac{\partial\phi}{\partial x_j} dS_j + \int_V q dV \tag{2.5}$$

Because of the velocities that are involved in DP manoeuvres for both, the ship motion as well as the flow around the ship's structure, the fluids can be assumed to be incompressible, i.e. the density is constant. Therefore, the influence of a variable density can be neglected.

2.2 Equations for viscose turbulent flow

An efficient technique for solving the above introduced Navier-Stokes equations and the continuity equation is to divide the velocity and pressure into time averaged and a fluctuation part. This approach yields to the Reynolds-Averaged Navier-Stokes Equations (RANSE).

2.2.1 Reynolds-Averaged Navier-Stokes Equation

In case of turbulent flows, i.e. high-Re flows around ships, the velocity and the pressure are frequently decomposed into a time-averaged and a statistically fluctuation part, formally known as Reynolds decomposition:

$$u_i = \bar{u_i} + u_i', \quad p = \bar{p} + p'. \tag{2.6}$$

By inserting this decomposition into the above introduced momentum and continuity equation the Reynolds-Averaged Navier-Stokes Equations are formed.

Turbulence model

The subsequent averaging of the Navier-Stokes equation yield to the unclosed nonlinear correlation $\bar{u_i'}\phi$, which are modeled by generalized Boussinesq viscosity models:

$$\bar{u_i'}\bar{u_j'} = \frac{2}{3}k\delta_{ij} - \mu_t(\frac{\partial\bar{u_i}}{\partial x_j} + \frac{\partial\bar{u_j}}{\partial x_i}) \tag{2.7}$$

where μ_t is the turbulence eddy viscosity and $k = \frac{1}{2}\bar{u_i'}\bar{u_i'}$ denotes the turbulent kinetic energy. The Reynolds-averaging yields to the above introduced turbulent eddy viscosity and kinetic

energy which represent two additional unknowns to represent the turbulent flow. In the present work, two common approaches for coupling the Reynolds stresses with the gradient of the average velocities are applied: $k-\epsilon$ and $k-\omega$-SST. While the $k-\epsilon$ model is essentially a high Reynolds model, which means that a wall function has to be applied in the near wall region and is very sensitive to adverse pressure gradients, the $k-\omega$-SST model improves this drawback through the Shear Stress Transport (SST) concept.

Realizable two-layer $k-\epsilon$ - turbulence model

An alternative approach of the standard $k-\epsilon$ model is introduced by the realizable two-layer model. In contrast to the standard model, the two-layer scheme allows the $k-\epsilon$ model to be applied in the viscous sublayer. Here, the computation is divided into two layers. Hence the turbulent dissipation rate ϵ and the turbulent viscosity μ_t are specified as function of wall distance and blended smoothly with values computed far away from the wall.
The standard $k-\epsilon$ turbulent model relates the turbulent kinetic energy k and the turbulence dissipation ϵ to the turbulent viscosity:

$$\mu_\tau = \rho C_\mu \frac{k^2}{\epsilon} \tag{2.8}$$

A two-layer approach invented by Rodi [71] has been used for resolving the viscose sublayers. The quantities of k and ϵ are solved by two additional transport equations:

$$\frac{\partial(\rho k)}{\partial t} + \frac{\partial(\rho k u_j)}{\partial x_j} = \frac{\partial}{\partial x_j}\left[\left(\mu + \frac{\mu_t}{\sigma_k}\right)\frac{\partial k}{\partial x_j}\right] + P_k + \rho(\epsilon - \epsilon_0) + S_k \tag{2.9}$$

$$\frac{\partial(\rho \epsilon)}{\partial t} + \frac{\partial(\rho \epsilon u_j)}{\partial x_j} = \frac{\partial}{\partial x_j}\left[\left(\mu + \frac{\mu_t}{\sigma_\epsilon}\right)\frac{\partial \epsilon}{\partial x_j}\right] + \frac{1}{T_e} C_{\epsilon 1} P_\epsilon - C_{\epsilon 2}\, f_2\, \rho \left(\frac{\epsilon}{T_e} - \frac{\epsilon_0}{T_0}\right) + S_\epsilon \tag{2.10}$$

where

$$C_{\epsilon 1} = max\left[0.43, \frac{\eta}{\eta + 5}\right], \quad \eta = S\frac{k}{\epsilon}, \quad S = \sqrt{2 S_{ij} S_{ij}}$$

and the model coefficients typically read

$$C_{\epsilon 2} = 1.9, \quad C_\mu = 0.09, \quad \sigma_\epsilon = 1.2, \quad \sigma_k = 1 \tag{2.11}$$

Further information can be obtained from Shih et al. [76].

SST Menter $k-\omega$ - turbulence model

The ϵ transport equation can be transformed into an ω transport equation by variable substitution. Menter suggested using a blending function to include a cross-diffusion term far from walls, but not near walls. This approach allows a blending of a $k-\epsilon$ model in the far-field with k_ω near the wall.

The turbulent viscosity is calculated as

$$\mu_t = \rho k T \tag{2.12}$$

where T is the turbulent time scale

$$\begin{aligned} T &= min\left(\frac{\alpha^*}{\omega}, \frac{a_1}{SF_2}\right) \\ \alpha^* &= 1, \quad a_1 = 0.31 \end{aligned} \tag{2.13}$$

The transport equations for the SST $k-$Omega model are [57]:

$$\frac{\partial(\rho k)}{\partial t} + \frac{\partial \rho u_j k}{\partial x_j} = \frac{\partial}{\partial x_j}\left[(\mu + \sigma_k \mu_t)\frac{\partial k}{\partial x_j}\right] + P_k - \rho\beta^* f_{\beta^*}(\omega k - \omega_0 k_0) + S_k \tag{2.14}$$

$$\frac{\partial(\rho \omega)}{\partial t} + \frac{\partial(\rho \mu_j \omega)}{\partial x_j} = \frac{\partial}{\partial x_j}\left[(\mu + \sigma_\omega \mu_t)\frac{\partial \omega}{\partial x_j}\right] + P_\omega - \rho\beta f_\beta(\omega^2 - \omega_0^2) + S_\omega \tag{2.15}$$

with the coefficients and relations

$$\sigma_k = 1 - 0.15 \cdot F_1, \quad \sigma_\omega = 1 - 0.356 \cdot F_1, \quad \beta^* = 1, \quad \beta = 1 - 0.0078 \cdot F_1$$

The blending factor F_1 combines the near-wall contribution of a coefficient with its value far away from the wall. Details of F_1, the turbulent production rate P_k and the specific dissipation production rate P_ω can be found in the user manual [77].

F_2 is a blending function. Further details can be found in [77].

2.2.2 Resolving turbulent structures by Detached Eddy Simulation

The Detached Eddy Simulation (DES), introduced by Tarvin et al. [81], represents a hybrid method that combines the solution of a Large Eddy Simulation (LES) for structures only away from the walls and the averaged flow solution computed with RANS in the wall boundary layer and irrotational flow regions. Thereby, the turbulent structures in space are resolved down to the grid limit, where subgrid models approximate the impact of the subrid structures on the flow field. In this work, the SST $k-\omega$ DES model has been used for the RANS solution and the Improved Delayed Detached Eddy Simulation (IDDES) for the DES variant.
In contrast to the RANS equations, where the solution variables are averaged, the equations solved by large eddy method are obtained by spatial filtering. Hence, each solution variable ϕ is separated into a filtered $\tilde{\phi}$ and a sub-grid value ϕ':

$$\phi = \tilde{\phi} + \phi' \tag{2.16}$$

The filtering of the generic flow variable $\phi(x,t)$ is defined as:

$$\tilde{\phi}(t,x) = \iiint_{-\infty}^{\infty} G(x-x',\Delta)\phi(t,x')dx' \tag{2.17}$$

Here, $G(x,\Delta)$ is a filter function with a filter width of $\Delta_f = (\Delta_x\Delta_y\Delta_z)^{1/3}$.
By inserting the above decomposition into the Navier-Stokes equations and rearranging the equations into a form that are identical to the unsteady RANS equations the following is obtained:

$$\frac{\partial(\rho\tilde{u}_i)}{\partial t} + \frac{\partial}{\partial x_j}(\widetilde{u_i u_j}) = -\frac{1}{\rho}\frac{\partial\tilde{p}}{\partial x_i} + \mu_t\frac{\partial}{\partial x_j}\left(\frac{\partial\tilde{u}_i}{\partial x_j} + \frac{\partial\tilde{u}_j}{\partial x_i}\right) \tag{2.18}$$

The filtered advection term can be split up as, so that the turbulent stress tensor now represents the subgrid scale stresses:

$$\widetilde{u_i u_j} = \tau_{ij} + \tilde{u}_i\tilde{u}_j \tag{2.19}$$

For the RANS model the Reynolds-stress tensor is a function of time- and length-scale

$$T_t^{RANS} = f(\nabla\cdot\bar{v}, k, \epsilon) \tag{2.20}$$

and for LES

$$T_t^{LES} = f(\nabla\cdot\tilde{v}, \Delta_f) \tag{2.21}$$

A unified approach is used to solve for a quantity $\hat{v}$ that is dependent on the local definition:

$$\frac{\partial(\rho\hat{v}_i)}{\partial t} + \frac{\partial}{\partial x_j}(\widehat{v_i v_j}) = -\frac{1}{\rho}\frac{\partial\hat{p}}{\partial x_i} + \mu_t\frac{\partial}{\partial x_j}\left(\frac{\partial\tilde{u}_i}{\partial x_j} + \frac{\partial\tilde{u}_j}{\partial x_i}\right) \tag{2.22}$$

where the model stress tensor is defined as:

$$T_t^{model} = f_\Delta\left(\frac{\Delta}{l_k}\right)T_t^{RANS} \tag{2.23}$$

with f_Δ is a damping function, l_k denotes the turbulent length scale and Δ is the local measure of the grid size ($\Delta = \max(\Delta_x, \Delta_y, \Delta_z)$). Further details of the considered models can be find in StarCCM+ User Manual [77].

2.3 Equations for invsicid and irrotational flow

In case of inviscid irrotational flow the Navier-Stokes equation may be greatly simplified. The viscose term is omitted and the rotation is zero. Hence, the velocity can be described by a

scalar potential ϕ:

$$\vec{v} = \left\{ \begin{array}{c} u \\ v \\ w \end{array} \right\} = \nabla\phi \tag{2.24}$$

The continuity equation simplifies to Laplace's equation for potential flow:

$$\Delta\phi = \phi_{xx} + \phi_{yy} + \phi_{zz} \tag{2.25}$$

If the volumetric forces are limited to gravity forces, the conservation of the linear momentum can be written as:

$$\nabla \left(\phi_t + \frac{1}{2} \left(\nabla\phi\right)^2 - gz + \frac{1}{\rho}\, p \right) = 0 \tag{2.26}$$

The integration yields to Bernoulli's equation:

$$\phi_t + \frac{1}{2} \left(\nabla\phi\right)^2 - gz + \frac{1}{\rho}\, p = const. \tag{2.27}$$

2.4 Numerical flow solution

The numerical methods differ in the type of discretisation of the computational domain and the solution of the corresponding equations. While the turbulent flow is solved by a finite volume method for the inviscid irrotational flow a boundary element method is applied.

2.4.1 Finite volume method

In order to solve the flow problem by the governing equations, the transport equations have to be discretised in space and time. The numerical solution method of the turbulent flow is adopted from the Finite-Volume Method (FVM). Hence, the computational domain is represented by a finite number of contiguous and arbitrary shaped control volumes. All quantities of the transport equations are stored cell centered. The objective is to obtain a set of linear algebraic equations according to the number of finite volumes in the representative grid.
For the convective flux and the diffusion, a scheme of second order discretization scheme is applied. In case of the convection, the value ϕ has to be determined at the center of each cell face. In order to consider a more dominant directed upstream an upwind scheme is used:

$$\phi_f\, \dot{m} \quad = \quad \left\{ \begin{array}{ll} \dot{m}_f\, \phi_{f,0} & \text{for } \dot{m}_f \geq 0 \\ \dot{m}_f\, \phi_{f,1} & \text{for } \dot{m}_f < 0 \end{array} \right. \tag{2.28}$$

where the face values $\phi_{f,0}$ and $\phi_{f,1}$ are obtained from linear interpolation from the cell center to either side of the face:

$$\phi_{f,0} = \phi_0 + s_0 \cdot (\nabla\phi)_{r,0} \tag{2.29}$$

$$\phi_{f,1} = \phi_1 + s_1 \cdot (\nabla\phi)_{r,1} \tag{2.30}$$

where

$$s_0 = x_f - x_0 \tag{2.31}$$

$$s_1 = x_f - x_1 \tag{2.32}$$

The indices 0 and 1 denote the adjacent cell-0 and cell-1 with the cell centers x_0 and x_1.
For the diffusive fluxes, an approximation of the gradient at the cell face is required. To obtain an accurate second order expression for an interior face gradient that implicitly involves the cell values ϕ_0 and ϕ_1 the following is used:

$$\nabla\phi_f = (\phi_1 - \phi_0)\vec{\alpha} + \overline{\nabla\phi} - (\overline{\nabla\phi} \cdot ds)\vec{\alpha} \tag{2.33}$$

where

$$\vec{\alpha} = \frac{a}{a \cdot ds} \tag{2.34}$$

$$ds = x_1 - x_0 \tag{2.35}$$

$$\overline{\nabla\phi} = \frac{(\nabla\phi_0 + \nabla\phi_1)}{2} \tag{2.36}$$

The expressions for the convective and diffusive fluxes are valid for all interior cell faces. On the boundaries of the computational domain, boundary conditions are applied. The integrals over the boundary surface are then solved with the known boundary data and the cell data from the domain inside. For the Dirichlet boundary condition the convective and diffusive fluxes are computed by replacing the face values ϕ_f and ϕ_1 by the known boundary value ϕ_b as well as the gradient $\overline{\nabla\phi}$ by $\overline{\nabla\phi_0}$. In case of the Neumann boundary condition, the diffusive fluxes are calculated directly with the variable values at the boundary being obtained from the discretised approximation.
The approximation of the time derivatives that was used is of second order. The temporal scheme uses the solution at the current time level n+1, as well as the solution from the previous two time levels, n and n-1:

$$\frac{d}{dt}(\rho\phi V)_0 = \frac{3\left[(\rho\phi V)_0^{n+1} - (\rho\phi V)_0^n\right] + \left[(\rho\phi V)_0^{n-1} - (\rho\phi V)_0^n\right]}{2\Delta t} \tag{2.37}$$

With incorporated discrete equations a linear equation system can be formed. For the transported variable ϕ applies:

$$\frac{a_p}{\omega}\Delta\phi_p + \sum_n a_n \Delta\phi_n = r \tag{2.38}$$

with the transported variable at iteration $k+1$ (current step) and k (previous step) follows:

$$\Delta\phi_p = \phi_p^{k+1} - \phi_p^k \tag{2.39}$$

The summation is over all neighbors n of cell p. The right handed side of the equation is formulated by:

$$r = -\left[\frac{d}{dt}(\rho\phi V) + \sum_f (\rho\phi\vec{v}\cdot\vec{a})_f - \sum_f (\Gamma\nabla\phi\cdot\vec{a})_f - S_\phi V\right] = 0. \tag{2.40}$$

r represents the discretised from of the transport equation at iteration k.
The non-linearities require an iterative solution procedure. Hence, there are two levels of iteration: an outer iteration loop controlling the solution update and an inner loop governing the iterative solution of the linear system. Hereby, the solution of the linear system is only approximated at each outer iteration. The iterative solution of the linear system is accomplished using Algebraic Multigrid (AMG).
The integral conservation equations of mass and momentum are solved in a sequential manner by the segregated flow solver. Thereby, a pressure-velocity coupling algorithm, where mass conservation constraint on the velocity field is fulfilled by solving a pressure correction equation. Thus, a predicted velocity field is needed to comply the continuity equation which is then achieved by the pressure correction. This work uses the pressure-velocity coupling algorithm SIMPLE.

2.4.2 Boundary element method

For potential flows, the integrals over the whole fluid domain can be transformed to integrals over the boundaries of the fluid domain. With the linearity of the Laplace equation, the potential Φ inside the computational domain can be decomposed into a potential of the incident wave Φ_i, a potential Φ_r of the radiated wave caused by the motion of the structure and a diffraction potential Φ_d that accounts the impact of the present body in the incident wave:

$$\Phi \quad = \quad \Phi_i + \Phi_r + \Phi_d \tag{2.41}$$

The flow problem is solved in frequency domain. Hence, the potential of the incident wave for deep water is known from linear wave theory expressed in a right handed Cartesian coordinate

system with z directed into the fluid:

$$\Phi_i = \frac{-i\zeta_a g}{\omega} \cdot e^{kz} \cdot e^{i(k(xcos(\psi)+ysin(\psi))-\omega t)} \tag{2.42}$$

The potentials for radiation Φ_r and diffraction Φ_d are determined numerically by using the following boundary conditions:

1. Decaying velocity with water depth
2. Atmospheric pressure prevails everywhere on the free surface (dynamic condition)
3. There is no flow through the free surface (kinematic condition)
4. There is no flow through the body contour
5. Waves created by the body must radiate away from the body

The numerical solution can be applied for the two-dimensional and three-dimensional flow problem. A brief description is given.

Two dimensional panel method

The radiation and diffraction flow problem is computed in a two-dimensional cross-section in harmonic elementary waves, hence the number of force directions reduces to transversal, vertical force and a moment around the longitudinal ship symmetry axis [9].
In frequency domain the harmonic time dependency is used and the Laplace equation as well as the relevant boundary conditions can be formulated by the time-independent complex amplitudes $\hat{\phi}$ of the potential. The boundary conditions then yield to:

Laplace equation:

$$\hat{\phi}_{yy} + \hat{\phi}_{zz} = 0 \quad for z < 0 \tag{2.43}$$

Decay condition:

$$\lim_{z\to\infty} \nabla\hat{\phi} = 0 \tag{2.44}$$

The kinematic and dynamic boundary condition at the free surface can be combined by differentiation of the dynamic condition with respect to time and omitting nonlinear terms.

Combined dynamic and kinematic boundary condition:

$$\frac{\omega^2}{g}\,\hat{\phi} + \hat{\phi}_z = 0 \quad at\ z = 0 \tag{2.45}$$

Body boundary condition:

$$\begin{aligned} \vec{n} \cdot \nabla \hat{\phi}_i &= \hat{\vec{v}}_i \cdot \vec{n}_i \\ i &= 1, 2, 3 \end{aligned} \tag{2.46}$$

Here, $\hat{\vec{v}}$ is the complex amplitude of the body motion velocity with $\hat{\vec{v}}_1 = i\omega(1; 0)$ for sway, $\hat{\vec{v}}_2 = i\omega(0; 1)$ for heave and $\hat{\vec{v}}_3 = i\omega(-z; y)$ for the roll motion. The latter uses the corresponding coordinates $(-z; y)$ of the section contour.
The body boundary condition is treated for the radiation and diffraction solution slightly different. For the radiation the in-homogeneous terms of equation 2.46 are the fluxes which would occur at the sections if the body will oscillate in the corresponding direction in calm water. In the diffraction calculation, the flux due to the incoming wave has to be canceled by the source-induced flow.

Radiation condition:

$$\hat{\phi}_y = \pm ik\hat{\phi} \tag{2.47}$$

The patch method approximates the flow potential as a superposition of point sources

$$\hat{\phi}(y, z) = \sum_{i=1}^{n} q_i \frac{1}{2} ln[(y - y_i)^2 + (z - z_i)^2] \tag{2.48}$$

where q_i are the Rankine source strengths of the nth source at location (y_i,z_i). This formulation automatically fulfills the Laplace equation and decay condition. In order to avoid singularities at the location of the sources itself, the method uses desingularized sources located inside the body and above the free surface. Further, the strip method PDSTRIP uses a patch method to numerically enforce the boundary condition, i.e. the integral of the corresponding boundary condition over discrete segments of the boundary is used. The source strengths q_i may be numerically solved by a linear equation system consisting of the geometric discrete section offsets and the correlating boundary conditions [9].
The resulting complex amplitudes of all source strengths obtained from the solution of the linear equation system are then used to compute the complex amplitude of the pressure by applying Bernoulli's equation:

$$p = -\rho\phi_t \tag{2.49}$$

The complex amplitudes of the forces and moment are obtained by integration of the pressure amplitude over the section contour. Considering the solution with unit amplitude the following proportionality between the force and the motion amplitude is derived:

$$\hat{f} \propto constant \cdot \hat{u} \tag{2.50}$$

In order to distinguish between forces in 180° phase relative to the motion, i.e. added mass, and forces in phase with the velocity, i.e. damping, the proportionality is formulated by:

$$\hat{f} \;=\; -\hat{m}\,(-\omega^2\hat{u}) \tag{2.51}$$

with

$$\hat{m} \;=\; m - \frac{id}{\omega}. \tag{2.52}$$

The hydrodynamic forces, i.e. added mass and damping, and the wave excitation forces, i.e. sum of Froude-Kriloff (force contribution of the incident wave) and diffraction force, for the ship are then obtained by integration of the sectional forces over the ship length.

Three dimensional panel method

The potential flow for the radiation and diffraction is calculated on a three-dimensional representation of the hull surface. Hence, the surface of the subjected vessel is discretised into N panels in the shape of squares (QPPL) and triangles (TPPL). A control point $\vec{\xi}$ is located at the center of each panel. Analogous to the two-dimensional boundary conditions described in the previous section, the panel method considers the extension by the third dimension [5]:

Laplace equation:

$$\Delta\phi \;=\; \frac{\partial^2\phi}{\partial X^2} + \frac{\partial^2\phi}{\partial Y^2} + \frac{\partial^2\phi}{\partial Z^2} = 0 \tag{2.53}$$

Body surface conditions:

$$\frac{\partial\phi}{\partial n} \;=\; \begin{cases} -i\omega\vec{n}, & \text{for radiation potential} \\ -\frac{\partial\phi}{\partial n}, & \text{for diffraction potential} \end{cases} \tag{2.54}$$

In order to solve the the velocity potential, an integration approach is employed. In the computational domain Ω the pulsating Green's function $G(\vec{X},\vec{\xi},\omega)$ is applied, which automatically satisfies the Laplace equation and the other boundary conditions:

$$\Delta G(\vec{X},\vec{\xi},\omega) \;=\; \frac{\partial^2 G}{\partial X^2} + \frac{\partial^2 G}{\partial Y^2} + \frac{\partial^2 G}{\partial Z^2} = \delta(\vec{X}-\vec{\xi}) \quad \text{where } X \in \Omega \text{ and } \xi \in \Omega \tag{2.55}$$

The vector $\vec{\xi} = (\xi,\eta,\zeta)$ denotes the position of each panel. The Dirac function defines:

$$\delta(\vec{X}-\vec{\xi}) \;=\; \begin{cases} 0 & \text{where } \vec{X}-\vec{\xi} \neq 0 \\ \infty & \text{where } \vec{X}-\vec{\xi} = 0 \end{cases} \tag{2.56}$$

In this approach the frequency domain pulsating Green's function is introduced by [5]:

$$G(\vec{X},\vec{\xi},\omega) = \frac{1}{r_1}+\frac{1}{r_2}+H(Z,d,\omega) \tag{2.57}$$

where $H(Z,d,\omega)$ is a harmonic decaying function (compare [5]), and

$$R = \sqrt{[(X-\xi)^2+(Y-\eta)^2]} \tag{2.58}$$
$$r_1 = \sqrt{[R^2+(Z-\zeta)^2]} \tag{2.59}$$
$$r_2 = \sqrt{[R^2+(Z+\zeta-2d)^2]} \tag{2.60}$$

The Second Green theorem is used for transforming the necessary integral over volume to integral over surface:

$$\iiint_\Omega [\phi(\Delta G)-G(\Delta\phi)]dV = \iint_S (\phi\frac{\partial G}{\partial n}-G\frac{\partial\phi}{\partial n})\,dS \tag{2.61}$$

The velocity potential of the diffraction and radiation waves can then be expressed as a Fredholm integral equation of the second kind over the surface of the hull S_0:

$$c\,\phi(\vec{X}) = \int_{S_0}\phi(\vec{\xi})\frac{\partial G(\vec{X},\vec{\xi},\omega)}{\partial n(\vec{\xi})}-G(\vec{X},\vec{\xi},\omega)\frac{\partial\phi(\vec{\xi})}{\partial n(\vec{\xi})}\,dS \tag{2.62}$$

where

$$c = \begin{cases} 0 & \vec{X}\notin\Omega\cup S_0 \\ 2\pi & \vec{X}\in S_0 \\ 4\pi & \vec{X}\in\Omega \end{cases} \tag{2.63}$$

Since the Green's function already obeys the condition at the domains boundaries, the solution can be obtained only by applying the body boundary condition:

$$\frac{\partial\phi(\vec{X})}{\partial n(\vec{X})} = -\frac{1}{2}\sigma(\vec{X})+\frac{1}{4\pi}\int_{S_0}\sigma(\vec{\xi})\frac{\partial G(\vec{X},\vec{\xi},\omega)}{\partial n(\vec{X})}\,dS \quad \text{where } \vec{X}\in S_0 \tag{2.64}$$

The Hess-Smith panel method [34] is used to solve the equations. The source strength over each panel surface is constant and taken as the corresponding average values. The discrete form yields to:

$$\varphi(\vec{X}) = \frac{1}{4\pi}\sum_N^{m=1}\sigma_m G(\vec{X},\vec{\xi}_m,\omega)\Delta S_m \tag{2.65}$$

$$-\frac{1}{2}\sigma_k+\frac{1}{4\pi}\sum_N^{m=1}\sigma_m\frac{\partial G(\vec{X}_k,\vec{\xi}_m,\omega}{\partial n(\vec{X}_k)}\Delta S_m = \frac{\partial\varphi(\vec{X}_k)}{\partial n(\vec{X}_k)} \tag{2.66}$$

where N panels are distributed over the mean wetted body surface with a discrete area ΔS_m of the m-th panel. The geometric center of of the m-th and k-th panel are noted by $\vec{\xi}_m$ and $\vec{X}_k$. The Bernoulli's equation may then be used to calculate the hydrodynamic pressure distribution:

$$p = -\rho \frac{\partial \Phi(\vec{X}, t)}{\partial t} = i\omega\rho\phi(\vec{X})e^{-i\omega t} \tag{2.67}$$

The fluid forces are then obtained from the integration of the pressure over the wetted surface of the body. For the j-th radiation force caused by the radiation wave induced by the k-th unit amplitude body rigid motion the following fluid force is obtained:

$$F_{rjk} = -i\omega\rho \int_{S_0} \phi_r k(\vec{X}) n_j \, dS \tag{2.68}$$

By expressing the wave potential in real and imaginary parts the added mass an damping coefficients may be obtained with:

$$A_{jk} = \frac{\rho}{\omega} \int_{S_0} Im[\phi_{rk}(\vec{X})] n_j \, dS \quad ; \quad B_{jk} = -\rho \int_{S_0} Re[\phi_{rk}(\vec{X})] n_j \, dS \tag{2.69}$$

3 Numerical Framework

A holistic approach of numerical DP simulation platforms consists of three basic components: a module that represents the dynamics of the vessel, an algorithm that covers the guidance and control and an allocation module that optimizes the direction and thrust of the available maneuvering and propulsion devices. In figure 3.1 a principal scheme of the closed-loop DP simulation is illustrated. An interface allows the integration of arbitrary external loads, i.e. wind, wave and current loads. Together with the generated thrust of the allocation module, the mathematical model of the vessel computes the updated position and orientation. The DP controller module holds the filter algorithm of the vessels motion and the feed-back controller. By comparing the current position of the ship with the set position, the controller algorithm computes the forces and moments that are required to achieve the target. The simulation loop is closed by the allocation module which determines the optimal control parameter for all devices.
The following sections sketches the methods of the motion solver, the components of the DP controller as well as the allocation algorithm.

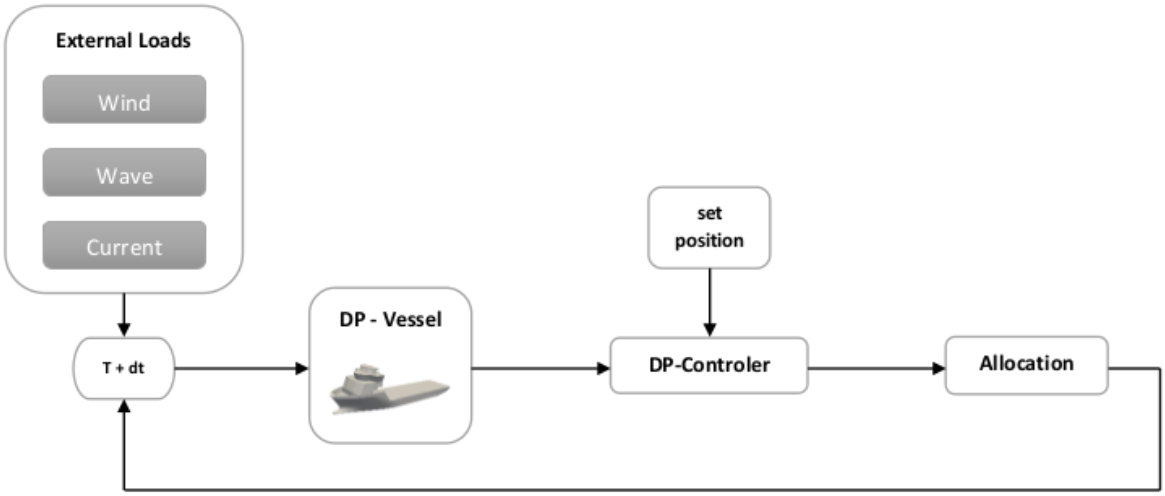

Figure 3.1: Scheme of the DP simulation time loop

3.1 Motion solver

For the closed-loop DP simulation the ship motion needs to be solved in time domain. An efficient procedure for the calculation of the acting hull forces is to determine those in frequency

domain and transfer the results into the time domain by using the impulse response functions. This method models the hydrodynamic damping forces and fluid memory effects due to radiated waves by applying the convolution integral $\int_0^\infty \mathbf{B}(\tau)\dot{\vec{\xi}}(t-\tau)\,d\tau$. Hence, this term can be interpreted as the superposition of decreasing reaction forces from all former impulses until the evaluated time. The governing equation is based on the formulation by Cummins [17]:

$$(\mathbf{M}+\mathbf{A})\ddot{\vec{\xi}}(t) + \int_0^\infty \mathbf{B}(\tau)\dot{\vec{\xi}}(t-\tau)\,d\tau + \mathbf{S}\vec{\xi}(t) = \vec{F}(t). \tag{3.1}$$

Here $\mathbf{M}$ and $\mathbf{A}$ represent the bodys inertia and the added mass matrix. $\mathbf{B}$ is the damping matrix. The matrix $\mathbf{S}$ denotes the restoring forces. A major advantage of the method is that arbitrary external forces can be easily taken into account by $\vec{F}(t)$. The position of the vessel is described by $\vec{\xi}$.

The matrices $\mathbf{A}$ and $\mathbf{B}$ can be determined by comparing the solution of equation 3.1 for a harmonic oscillation with unit amplitude, descibed by $\xi = 1.0 \cdot cos(\omega t)$, within the frequency domain solution. Ogilvie showed that the added mass and damping matrices can be obtained from frequency domain as follows [64]:

$$\mathbf{A} = \mathbf{a}(\omega) + \frac{1}{\omega}\int_0^\infty \mathbf{B}(\tau)sin(\omega\tau)\,d\tau \tag{3.2}$$

For infinity frequency the hydrodynamic damping vanishes (compare figure 3.2, left). Since the added mass converges asymptotically against a value, according to Journée and Massie [44] the following can be assumed for the hydrodynamic mass matrix in time domain:

$$\mathbf{A} = \mathbf{a}(\omega = \infty) \tag{3.3}$$

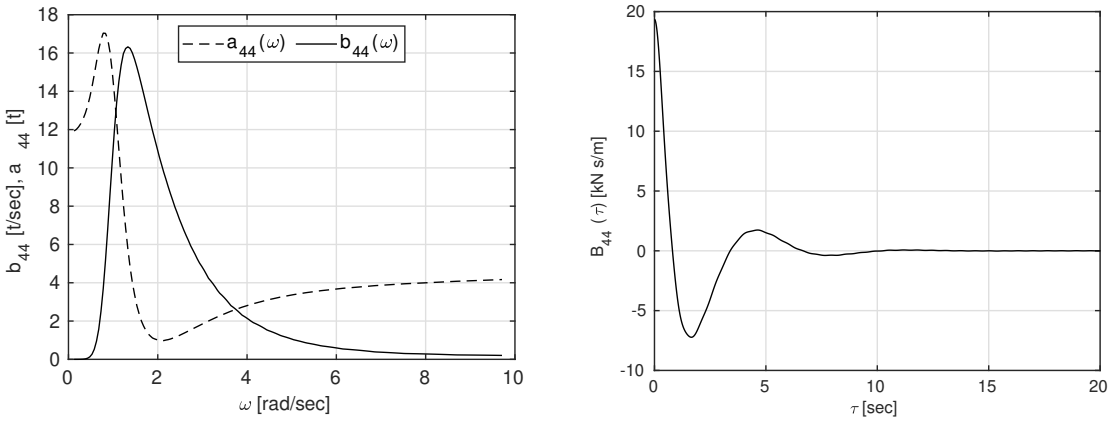

Figure 3.2: Added mass and damping of the roll motion for the OSV in frequency domain (left) Retardation function $B(\tau)$ for a single impulse of the roll motion (right)

Further, the coefficient comparison of the frequency domain solution with equation 3.1 reveals the description of the hydrodynamic mass in time domain, denoted as the retardation:

$$\mathbf{B}(\tau) = \frac{2}{\pi}\int_0^\infty \mathbf{b}(\omega)cos(\omega\tau)\ d\omega. \tag{3.4}$$

The decaying impulse, e.g. of the roll motion, is represented in figure 3.2 (right). For typical DP vessels a retardation time of $\tau_{max} = 20sec$ resulted in a sufficient time interval.
The above equations account for potential flow theory and therefore do not consider viscose damping effects. However, at low ship speeds, the flow separation at bilges and skeg accounts for a considerable proportion of the damping contribution. These flow effects are especially related to the longitudinal and transversal as well as the roll and yaw motion. To account for viscous damping effects an additional variable $\vec{F}_Q$ has been added:

$$(\mathbf{M}+\mathbf{A})\ddot{\vec{\xi}} + \vec{F}_{\mathbf{B}}(\dot{\vec{\xi}},t) + \vec{F}_Q(\dot{\vec{\xi}}) + \vec{S}(\vec{\xi},t) \quad = \quad \vec{F}(t) \tag{3.5}$$

For considering the damping effects on the roll motion, a quadratic damping moment with a linear d_L and a quadratic d_Q damping coefficient are introduced by Kröger [49] :

$$M_\varphi \quad = \quad (d_Q|\dot{\varphi}| + d_L)\dot{\varphi}. \tag{3.6}$$

Here, the quadratic and linear damping coefficients are either obtained from experiments, CFD simulations for viscous flow or prediction methods or i.e. emperical methods using neuronal networks (compare Wassermann et al. [89]).
For the ship motions in the horizontal plane the damping is accounted based on a two dimensional sectionwise approach (Brix [15] and Detlefsen [19]). Vertical and horizontal damping forces develop at cross sections of the hull and depend on the relative velocity between ship hull and fluid velocity:

$$\vec{f}_x(\dot{\vec{\xi}}) \quad = \quad \begin{bmatrix} 1 & 0 \\ 0 & 1 \\ z_x & y_x \end{bmatrix} \begin{pmatrix} T_x\ C_{Dy}\ u_{y,x}\ |u_{y,x}| \\ B_x\ C_{Dz}\ u_{z,x}\ |u_{z,x}| \end{pmatrix}. \tag{3.7}$$

The above determination of the sectionwise drag forces and roll moment uses the center coordinates of each section z_x and y_x. C_{Dy} and C_{Dz} are drag coefficients which can be determined by experiments or numerically. Typical values for the drag coefficients are $C_{Dy} \approx 0.8...1.2$ and $C_{Dz} \approx 0.6$ (Bertram and Söding [9]). The relative velocities are denoted by $u_{y,x}$ and $u_{z,x}$ in the sectional plane. T_x and B_x are the respective draft and beam of the considered section.
By integrating over the ship length L the global drag forces and moments are obtained:

$$\vec{F}_q(\dot{\vec{\xi}}) \quad = \quad \int_L \mathbf{V}(x)\ \vec{f}_x(\dot{\vec{\xi}})\ dx \tag{3.8}$$

The matrix $\mathbf{V}(x)$ transforms the sectional forces into the ship fixed system.
In fact, a two dimensional strip method is not able to calculate damping forces in logitudinal

direction. Therefore, a concept according to Fossen [27] is applied:

$$F_\xi(\dot{\xi}_0) = -\frac{1}{2}\,\rho\,S\,(1+k_f)\,C_f(\dot{\xi}_0)\,|\dot{\xi}_0|\,\dot{\xi}_0 \tag{3.9}$$

Herein, S represents the wetted surface area, k_f a viscous form factor and C_f a modified friction drag coefficient.
The viscous damping components are then combined in

$$\vec{F}_Q(\vec{\dot{\xi}}) = \vec{F}_q(\vec{\dot{\xi}}) + (F_\xi(\dot{\xi}_0)\ 0\ 0\ M_\varphi(\dot{\varphi})\ 0\ 0)^T \tag{3.10}$$

In figure 3.3, the roll angle of a roll decay simulation is shown and compared with the experimental data. The linear and quadratic damping coefficients are obtained by evaluating the logarithmic decrement of the decaying roll angle. The simulation has been conducted twice: a simulation using hydrodynamic coefficients obtained by the two dimensional strip method PDSTRIP and another simulation using the coefficients computed by the three dimensional panel method ANSYS AQWA.

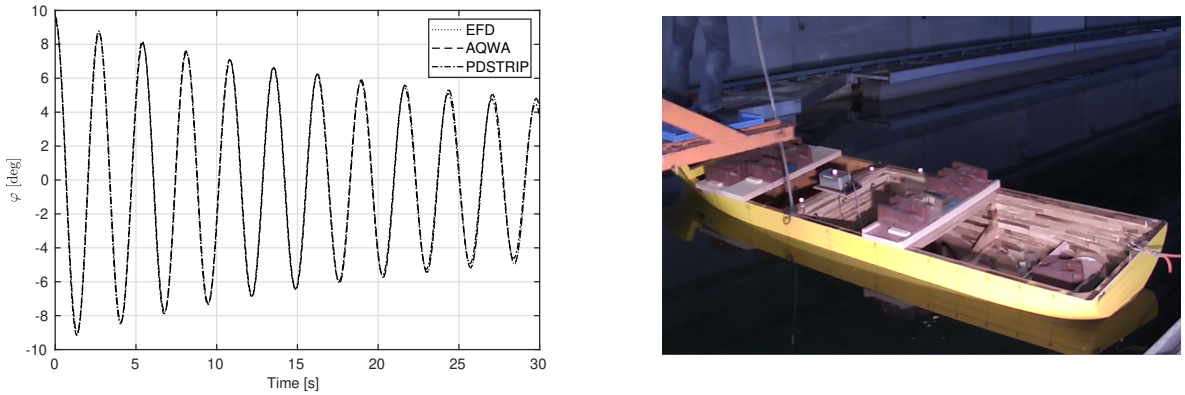

Figure 3.3: Experimental and numerical decay test $\varphi_0 = 9.64°$

The force vector $\vec{F}(t)$ of equation 3.1 can be decomposed into the following:

$$\vec{F}(t) \;=\; \vec{F}^{(1)}_{Wave}(t) + \vec{F}^{(2)}_{Wave}(t) + \vec{F}_{Wind}(t) + \vec{F}_{Current}(t) + \vec{F}_{thrust}(t) + \vec{F}_{ext}(t) \tag{3.11}$$

In linear theory, the first order wave excitation forces can be calculated by the superposition of the regular wave components (compare to Kröger [49] and Detlefsen [19]):

$$\vec{F}^{(1)}_{Wave}(t) \;=\; \sum_{j=1}^{N} Re[(\hat{\vec{F}}_{FK,j} + \hat{\vec{F}}_{DF,j})\,\hat{\zeta}_j\,e^{i\omega_{e,j}t}] \tag{3.12}$$

Here, the harmonic oscillation of the Froude-Krilov and the respective diffraction of the $j-$th wave component reveal together with the complex wave amplitude $\hat{\zeta}_j$ and the encounter frequency $\omega_{e,j}$ to the first order wave excitation force. The derivation of the second order wave

forces, wind and current can be found in the respective following sections.
An example of the first order wave forces for varying encounter angles and a wave length equal to the ship length is given in the appendix A.

3.2 DP controller

As it is decribed in the introduction of this chapter, the module of DP controler includes both, the controler and the observer with the filter. The controller algorithm has been developed by the Institute of Automation (IAT, University of Rostock) [43].
DP systems are feedback control systems, i.e. the control system continuously compares the actual position of the vessel being controlled with the set point and considers the difference as a control signal to the allocation. For the *DPTool* the most common feedback controller for DP application was selected: non-linear PID.
The relation between the ship dynamics in planar motion and the external forces, e.g. the propulsors, is described by an equation of motion according to Fossen [27]:

$$\dot{\eta} = \mathbf{R}(\psi)\nu \tag{3.13}$$

$$\mathbf{M}\dot{\nu} + \mathbf{D}\nu = \tau. \tag{3.14}$$

In the above equations η denotes the position and heading of the vessel, ν represents the respective velocities and rates. The rotation matrix $\mathbf{R}(\psi)$ transforms the scalars from body-fixed into earth-fixed coordinates. The dynamic behavior of the vessel is expressed by the mass and damping matrices $\mathbf{M}$ and $\mathbf{D}$. Finally, τ includes the forces and moments acting on the vessel.
For DP controllers wave-filtering is necessary to reduce high-frequent control errors caused by the mean free oscillatory motion of the ship in a seaway. Further, high-frequent controll subjects to an increase of the wear and tear of the mechanical components of the propulsion plant. Therefore, observer structures have been implemented. The most common technique is the use of Kalman Filter-based observer [28].
Using the controller inputs, as they are the desired set point $\eta_{\mathbf{set}}$ and the filtered position, headings and velocities, respectively $\hat{\eta}$ and $\hat{\nu}$, the control law for the DP controller can be formulated by

$$\tau_{\mathbf{PID}} = \mathbf{R^T}(\hat{\psi})\,\mathbf{K_P}\hat{\mathbf{e}} - \mathbf{K_D}\hat{\nu} + \mathbf{R^T}(\hat{\psi})\,\mathbf{K_I}\int_0^T \hat{\mathbf{e}}\,dt, \tag{3.15}$$

where $\mathbf{K_P}, \mathbf{K_D}, \mathbf{K_I}$ are the controller gains for the proportional, integral and differential parts. The control error $\hat{\mathbf{e}}$ is defined as $\eta_{\mathbf{set}} - \hat{\eta}$. Among other parametrization methods, the pole placement procedure and the LQ method are implemented in the DP tool for parametrizing the PID controller.
DP objective of disturbance rejection leads to strong controller reactions. Therefore, for the

set point processing a combination of a rate limiter and a linear system has been applied to smooth step-like set point changes for each degree of freedom.

3.3 Allocation

Due to the redundancy of any DP system, this problem is over-controllable. That means, appropriate analysis is needed, to establish which kind of allocation procedure is more indicated to cover specific tasks that can rise up during early design stage.

(a) (b) (c)

Figure 3.4: (a)Voith Schneider Propulsor [88], (b)Radial Propeller [87], (c)Inline Thruster [86]

The thrust allocation module used in this work has been developed by Voith Turbo GmbH & Co. KG [35]. Three different propulsors are availabe (compare figure 3.4). While the first two plants are in competition of each other for the steering and driving forces, the Inline Thruster is used to increase the yaw stability.

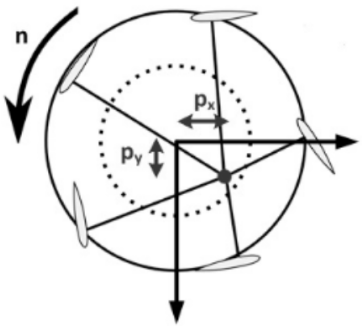

Figure 3.5: Sketch of VSP driving pitch and rudder pitch [47]

Contrary to conventional propellers, where the open water characteristic can be used to determine the propeller revolution and in case of controllable pitch propeller the pitch to achieve the

required thrust of the propulsors, the VSP accounts for a x/y-logic.
The thrust and side force of the VSP are obtained from pre-determined look-up tables. By interpolating the values of the database a connection between the resulting thrust and the controlled pitch vector $\mathbf{p} = [p_x, p_y]^T$, revolution rate $\mathbf{n}$ and inflow under open-water characteristic ($\mathbf{v^b} = [v_x^b, v_y^b]^T$, body-fixed) is produced:

$$\begin{bmatrix} F_x \\ F_y \\ P_D \end{bmatrix} = VSP(\mathbf{p}, n, \mathbf{v^b}). \tag{3.16}$$

F_x and F_y are the forces of the VSP in x- and y- direction and P_D respresents the deliverd power.
The thruster forces are obtained from experiments under open water condition, i.e. considering wide and deep water, neglecting interaction effects, etc. Therefore, the allocation module includes further corrections for:

- Interaction between hull and propeller by a loss factor distribution
- Forbidden zones for each actuator
- Reduction factor in case of propeller racing and bow thruster ventilation
- Advanced velocity correction, i.e. current velocity and orbital velocity of wave components

Brandner [14] and Jürgens et al. [45] introduced the calculation method of the actuator settings. A constrained, multi-criteria optimization is used in order to compute at first the parameters to obtain the desired forces in a short period of time, but also in an energy-efficient way. The sequential two-step procedure can be described by:

$$(I)\ J_1(x) \rightarrow min \Rightarrow \hat{x} \tag{3.17}$$

$$(II)\ J_2(x) \rightarrow min, s.t. J_1(x) = J_1(\hat{x}) \tag{3.18}$$

$$J_1(x) = \int_0^T ||\hat{\tau} - \tau_{thr}(x)||_2^2 \, dt \tag{3.19}$$

$$J_2(x) = \int_0^T ||P(x) - P_{min}||_2^2 \, dt \tag{3.20}$$

3.4 Integrated platform for closed-loop DP simulation

In context of this work the integrated platform *DPTool* with a graphical user interface for closed-loop DP simulation was developed. The platform enables the complete processing of a project for the numerical design of a DP system. The *DPTool* is divided into a project management database and a job manager.
The project management holds five modules, see figure 3.6. Basic data and load cases can be

created by the initial "Project" module. This interface collects all relevant input data for the following computations.
With the "Hydrodynamics" module the objective geometry can be discretized into sections for the hydrodynamic computation of the first and second order wave forces in frequency domain as well as the radiation forces. The underlaying subprogram *CASCO* for the discretization extracts sections from STL-based geometry descriptions, for further information see Theilen [80]. The interface allows both, the use of the PDStrip results and the results obtained by ANSYS AQWA. Finally the current load coefficients, as part of the under water hull forces, can either be imported from external sources, i.e. CFD computations, or approximated by an emperical formulation accoriding to DNV-GL [23].
The "Misc." module generates required data for viscous roll damping, imports wind load coefficients and creates the required data for the preparation of the simulation of the seaways.
The setup of the thruster can be initialized and adjusted in the "Propulsion" module. As it is described in section 3.3 three types of propulsion plants are available. The underlying open water performance can be modified by interaction factors, depending on the thrust direction. Further forbidden zones according to the rules of the class society DNV-GL can be set.
With the last module "GNC", the project setup is concluded by designing the controller. The dynamics of the vessel are identified by a system identification method. Here, either pre-defined excitation forces for the three planar motions can be used. Together with the identified mass and damping matrix the unique controller parameter can be parametrized by various methods. For the setup of the wave filter and observer a three dimensional response surface can be computed by using the motion model.

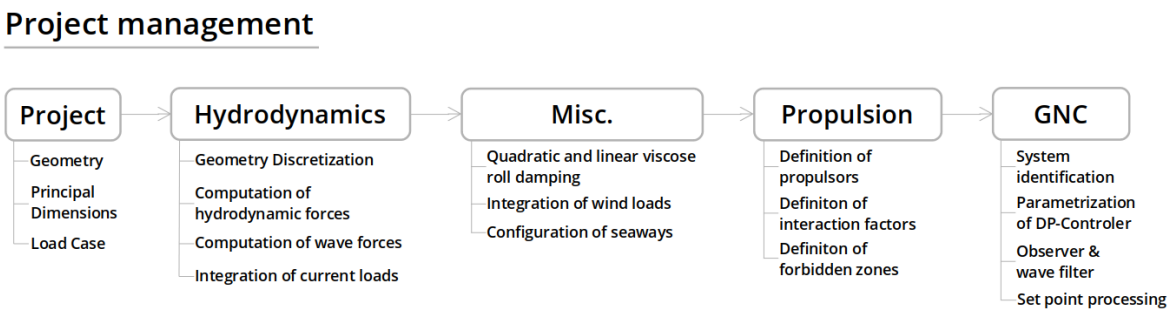

Figure 3.6: Sketch of the project management platform of the *DPTool*

The task of the job manager are manifold, but with the goal to allow a detailed assessment of the vessels dynamics exerted to single environmental loads up to a closed-loop accounting for all components dynamically.

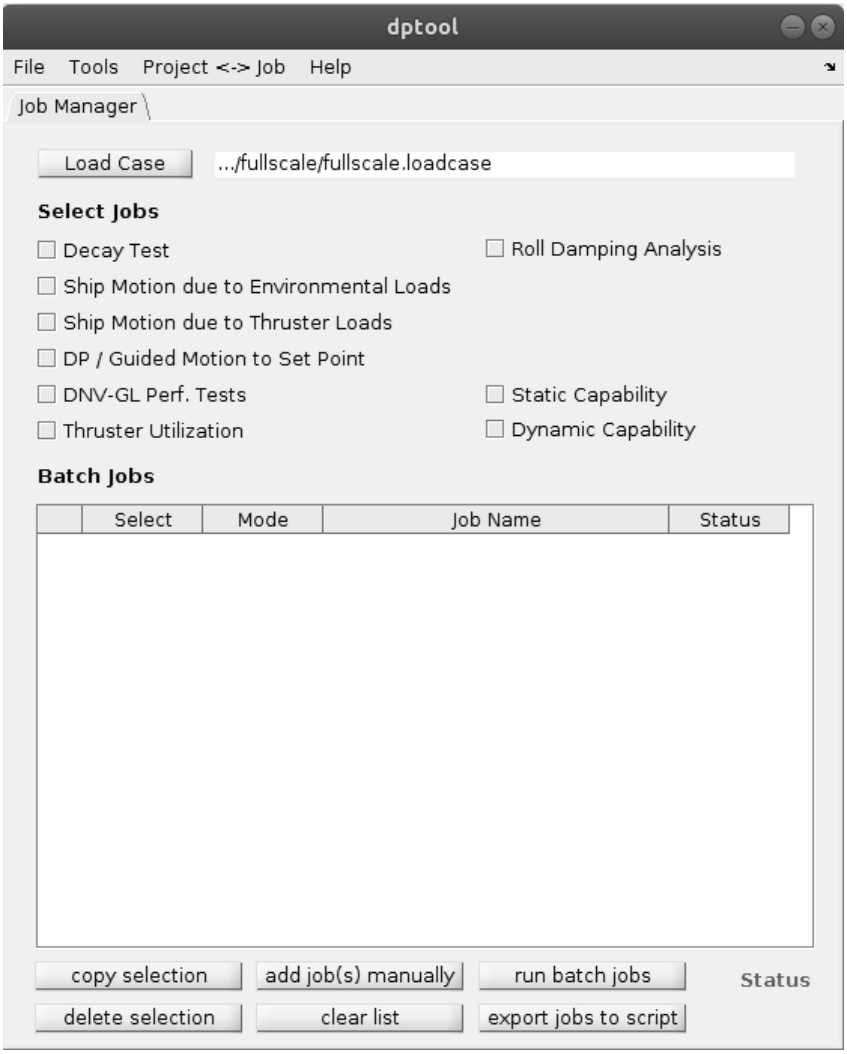

Figure 3.7: GUI of the *DPTool* job manager

4 Wind loads in DP operations

Although the impact of wind loads on ships represent only a fraction of the total environmental forces, wind forces play a significant role during station keeping operations. Typical designs of working vessels in the offshore industry, i.e. offshore supply vessels (OSV) or anchor handling tug supply vessels (AHTS), are known for their longitudinally asymmetric superstructure shapes and therefore wind loads lead to high yaw moments, passenger ships or mega yachts with high lateral expansion experience transversal forces of high magnitude during DP operations.
Due to the high degree of details, i.e. ladders, railings, antennas and other deck equipment, as well as the geometric extensions of deck houses with sharp edges and bluff body forms, the aerodynamics of ship's superstructures are characterized by complex flow structures. For an accurate assessment of the aerodynamic flow around the ship, either experiments or numerical simulations can be applied. However, simulations that account all effects are expensive and time-consuming. But, in contrast to experiments, numerical simulations have the advantage of extensive analysis, e.g. visualization of velocities and pressure. Further, experiments i.e. suffer from inaccuracies due to scale effects, corrections for wind tunnel blockage and the boundary at the floor of the test section.
The following section is concerned with the experimental and numerical assessment of wind loads for the use in DP simulations. At first, the implementation of wind loads in the *DPTool* is described. This is followed by an elaboration of wind load coefficients by experiments in a wind tunnel. Afterwards, the results of the wind tunnel tests are used for validating the proposed numerical setup. The chapter concludes with a comparison of the experimental and numerical approach and quantifies the impact of wind load uncertainty on the DP operation.

4.1 Implementation of wind loads in the DPTool

Dynamic wind loads are taken into account using a coefficient-based approach in the *DPTool*. The consideration of ship-specific coefficients obtained from experiments, a direct calculation and the use of a database of similar ships are integrated in the *DPTool*. Further, parametric wind loading functions according to Blendermann [10] and trigonometric series loading functions developed by Fujiwara [29] are implemented. A realistic time series of wind speed and direction is achieved through the use of wind spectra.

4.1.1 Dynamic wind speed and direction

The variation of wind speed $u(t)$ can be expressed by a constant mean flow speed and a time varying component:

$$u(t) = \bar{u} + u'(t). \tag{4.1}$$

Herein, $\bar{u}$ denotes the constant mean wind speed. The fluctuation $u'(t)$ can be described by wind spectra, which define the frequency-wise distribution of turbulent energy in the wind. Two principle types of wind spectra are implemented in the *DPTool*: Davenport and Frøya wind spectrum.
Davenport evaluated measurements of wind velocity from three land sites. This includes the roughness of the ground. From spectral analysis of the horizontal components of gustiness, Davenport provides the following formulation [18]:

$$S_u(f) = \frac{u_{10}^2 C_{10}}{f} \cdot \frac{4\bar{f}^2}{\left(1+\bar{f}^2\right)^{4/3}} \tag{4.2}$$

with

$$\bar{f} = \frac{f \cdot L}{u_{10}}. \tag{4.3}$$

In the above $\bar{f}$ is the nondimensional fluctuation frequency, u_{10} represents the mean hourly wind speed at a reference height of $z = 10m$ and L is a length parameter which is estimated to be $L = 1200m$ for wind over ocean. The influence of the roughness of the ground can be modified by C_{10}. Following Garrat [30], for seaways this parameter can be set as:

$$C_{10} = (0.75 + 0.067 \cdot u_{10}) \cdot 10^{-3}. \tag{4.4}$$

Another description of wind spectra is based on measurements of a meteorological station on the island of Frøya on the western coast of Norway [62]. This area represents an exposed coastal wind climate with open sea. Based on the measured data Anderson and Løvseth developed a formulation of a wind spectrum accounting realistic seaway boundary layer during weather conditions with relevance for marine structures [63]:

$$S_u(f) = \frac{320 \cdot \left(\frac{z}{10}\right)^{0.45} \cdot \left(\frac{u_{10}}{10}\right)^2}{\left(1+\bar{f}^n\right)^{5/3n}} \tag{4.5}$$

with

$$\bar{f} = 172 \cdot f \cdot \left(\frac{z}{10}\right)^{2/3} \left(\frac{u_{10}}{10}\right)^{-3/4} \tag{4.6}$$

$$n = 0.468. \tag{4.7}$$

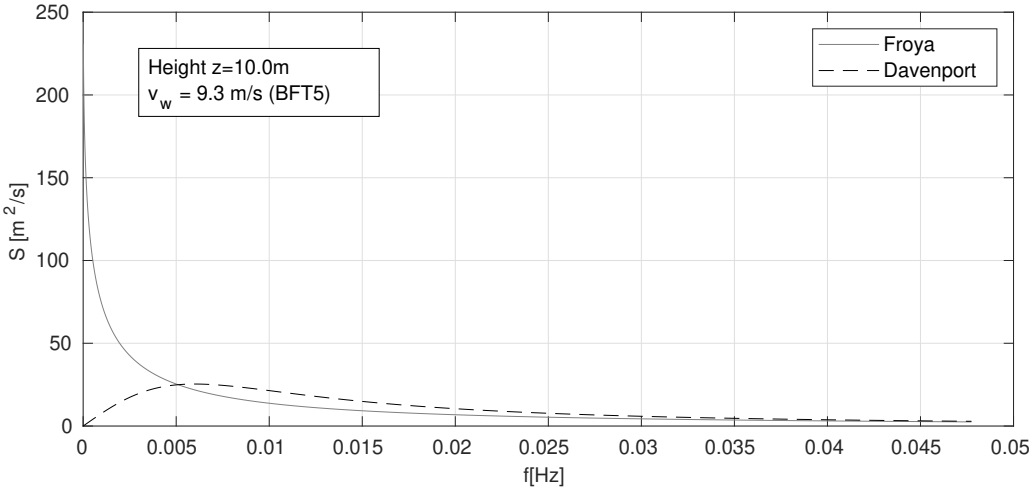

Figure 4.1: Comparison of Frøya and Davenport wind spectrum for wind of Beaufort 5

Figure 4.1 shows the energy density distribution of the wind speed fluctuations according to Davenport and Frøya accounting the same mean wind speed. The low-frequency range (f <0.005 Hz) of the Frøya spectrum is significantly more energetic than indicated by land-based studies. Over land the formation of large eddies in the air stream is prevented by obstacles, e.g. by mountains and buildings. Therefore, small-scale vortex structures dominate here at higher frequencies, while larger vorticies on the open sea are retained, which lead to low-frequency fluctuations in speed.
Then, the time varying wind speed is composed of a superposition of single harmonics:

$$u'(t) \quad = \quad \sum_{i=1}^{N} u_i \cdot cos\left(2\pi f_i t + \varphi_i\right) \tag{4.8}$$

The amplitudes and frequencies can be determined by discretising the wind energy density spectra. Thereby, the energy density is calculated over a frequency interval f_i with the boundary frequencies f_a and f_b. This yields to the energy-equivalent fluctuation amplitude u_i:

$$\int_{f_a}^{f_b} S_u(f)df \quad = \quad \frac{1}{2} \cdot u_i^2 \tag{4.9}$$

For the discretisation of the energy density spectra, the use of at least 200 harmonic components is recommended. The phase φ_i of the fluctuation components is chosen random (normally distributed).
The wind speed amplitude u_i and the corresponding frequency ω_i of the frequency band are derived by:

$$u_i \quad = \quad \sqrt{2\int_{\omega_a}^{\omega_b} S_u\left(\omega\right) d\omega} \approx \sqrt{2 \cdot S_u\left(\omega_i\right) \Delta\omega_i} \tag{4.10}$$

$$\omega_i \quad = \quad \frac{\omega_a + \omega_b}{2} \tag{4.11}$$

With an equidistant distribution of $\Delta\omega$ the wind speed is derived by:

$$u(t) = u_{10} + \sum_{i=1}^{N} \sqrt{2 \cdot S_u(\omega_i)\Delta\omega_i} \cdot cos\left(\omega_i t + \varphi_i\right) \tag{4.12}$$

Analogous to the wind speed, the fluctuation of the wind angle can also be determined by means of energy density spectra (compare Mahrt [53]). According to the results of large-scale measurements (Lübcke [50]) for the energy density spectrum of wind direction fluctuations a Weibull distribution can be used (Lübcke [51]):

$$S_\epsilon(\omega) = \frac{bc}{a}\left(\frac{\omega}{a}\right)^{c-1.0} \cdot \exp\left(-\left(\frac{\omega}{a}\right)^{c}\right) \tag{4.13}$$

with

$$a = 1.11 \cdot \exp\left(-0.12 \cdot u_{10}\right) \tag{4.14}$$

$$b = 0.08 \cdot \exp\left(-0.18 \cdot u_{10}\right) \tag{4.15}$$

$$c = 1.2 \tag{4.16}$$

In contrast to wind speed fluctuations, the energy density of the directional fluctuations vanishes with increasing mean wind speed. The wind direction ϵ is obtained from the mean wind angle $\bar{\epsilon}$ and the superposition of the fluctuating components

$$\epsilon(t) = \bar{\epsilon} + \sum_{i=1}^{N} \sqrt{2 \cdot S_\epsilon\left(\omega_i\right) \Delta\omega_i} \cdot cos\left(\omega_i t + \varphi_i\right). \tag{4.17}$$

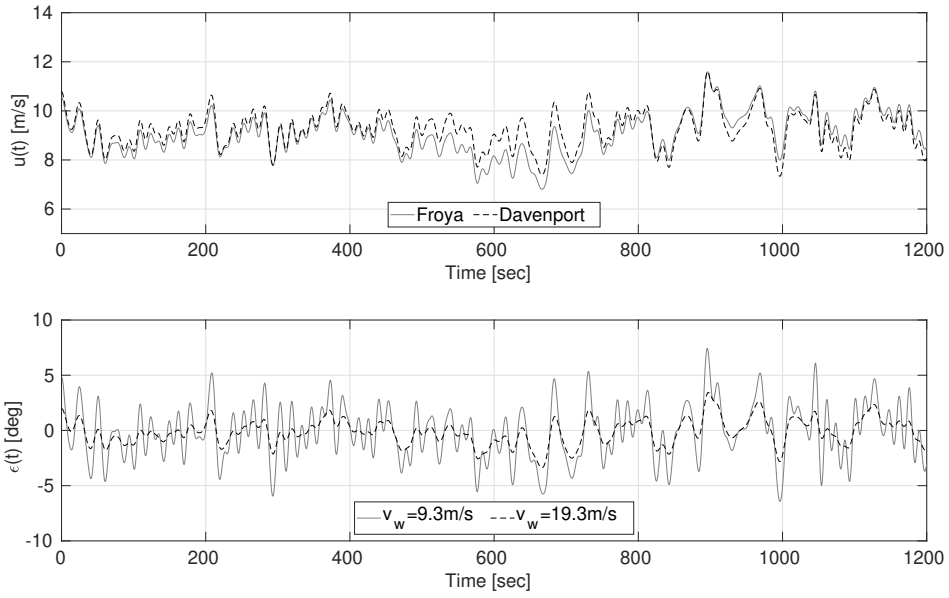

Figure 4.2: Wind velocity (top), wind encounter angle (bottom)

For demonstration, the wind speed and the wind direction fluctuation is illustrated in figure 4.2. The wind speed fluctuation shows a comparison between the wind speeds obtained from the Frøya and from the Davenport wind energy density spectrum. For better comparability identical frequencies and phases for the realization were used. The mean wind speed was set to $v_w = 9.3m/s$. The chart of the changing wind direction indicates fluctuation of about $\pm$ 5 deg for a wind speed of $v_w = 9.3m/s$, while the bandwidth reduces to $\pm$ 2.5 deg for an increment in mean wind speed of $\Delta v_w = 10m/s$.

4.1.2 Coefficient based wind loads

For the description of forces and moments due to wind loads a right handed Cartesian coordinate system is used. Its origin is located amidships in the waterline at bisecting the length between perpendiculars. The axis point forward to front perpendicular, starboard and downwards respectively. The coordinate system follows the motion of the ship. However, the horizontal axis remain parallel to the still water level. The encounter angle between air stream and ships heading ϵ is denoted positive counter-clockwise and $\epsilon = 0°$ means head winds (see fig. 4.3).

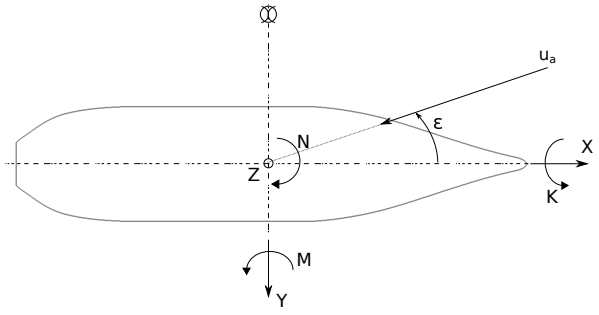

u_a : apparent wind
ϵ : angle of attack

X	:	Longitudinal Force	K	:	Roll Moment
Y	:	Lateral Force	M	:	Pitch Moment
Z	:	Vertical Force	N	:	Yaw Moment

Figure 4.3: Coordinate system of wind forces and moments

Table 4.1: Reference dynamic pressure

Longitudinal force	X	$q_{ref} = q_{\bar{H}}$
Lateral force	Y	$q_{ref} = k_q q_{\bar{H}} + (1 - k_q) q_{\bar{H}}, k_q \approx 0.6$
Yaw moment	N	$q_{ref} = k_q q_{\bar{H}} + (1 - k_q) q_{\bar{H}}, k_q \approx 0.6$
Roll moment	K	$q_{ref} = q_{\bar{H}}$

A common way is to express the wind load coefficients in non-dimensional form as it is declared by equations 4.20 - 4.25. Here, the dynamic pressure

$$q = \frac{1}{2} \cdot \rho_{air} \cdot u_A^2, \tag{4.18}$$

the lateral area of the vessels structure above the waterline AL, the length over all L_{OA} and the mean height of the lateral plane

$$\bar{H} = \frac{AL}{L_{OA}} \tag{4.19}$$

are used to non-dimensionalise the forces.

$$CX = \frac{X}{q \cdot AL} \tag{4.20}$$

$$CY = \frac{Y}{q \cdot AL} \tag{4.21}$$

$$CZ = \frac{Z}{q \cdot AL} \tag{4.22}$$

$$CK = \frac{K}{q \cdot AL \cdot \bar{H}} \tag{4.23}$$

$$CM = \frac{M}{q \cdot AL \cdot L_{OA}} \tag{4.24}$$

$$CN = \frac{N}{q \cdot AL \cdot L_{OA}} \tag{4.25}$$

Since wind loads vary with the encounter angle ϵ, it is necessary to determine the coefficients for the whole range of angles of wind attack from bow to stern. In general, the coefficients account for uniform flow. Therefore, a correction is needed when wind loads are computed for a vessel in its natural environment. Blendermann proposed the consideration of the natural boundary layer by introducing an individual reference dynamic pressure for each force component [11]. For the lateral force this approach yields to:

$$q_{ref} = k_q q_{\bar{H}} + (1 - k_q)\, q_{\bar{H}}, \tag{4.26}$$

where k_q represents a share that accounts forces on the windward and leeward side and adopts a value between $0 \leq k_q \leq 1$. The reference pressure for all force components is summarized in table 4.1. The mean dynamic pressure $q_{\bar{H}}$ refers to the mean height $\bar{H}$ of the ship (respectively q_{10} refers to a height of z =10 m)

$$\frac{q_{\bar{H}}}{q_{10}} = \frac{1}{\bar{H}} \int_0^{\bar{H}} \left(\frac{z}{10}\right)^{2/n} dz \tag{4.27}$$

The flow profile is modeled according to the power law (high winds at sea $5 \leq n \leq 10$ above open land or harbor areas)

Followed by the determination of the reference pressure, the wind loads can be computed with:

$$X = CX \cdot q_{ref} \cdot AL \quad (4.28) \qquad Y = CY \cdot q_{ref} \cdot AL \quad (4.30)$$
$$N = CN \cdot q_{ref} \cdot AL \cdot L_{OA} \quad (4.29) \qquad K = CK \cdot q_{ref} \cdot AL \cdot \bar{H} \quad (4.31)$$

4.2 Experimental approach

The experiments were carried out in the wind tunnel of the Institute for Fluid Dynamics and Ship Theory of Hamburg University of Technology, Germany. The wind tunnel is operated in a closed low-speed configuration with a maximum possible speed of $v_{max} = 30m/s$ equipped with an open test section (compare figure 4.7). The dimensions of the test section are 5 m in length, 3 m in beam and 2 m in height. The force measurement is carried out by a 6-component load balance.

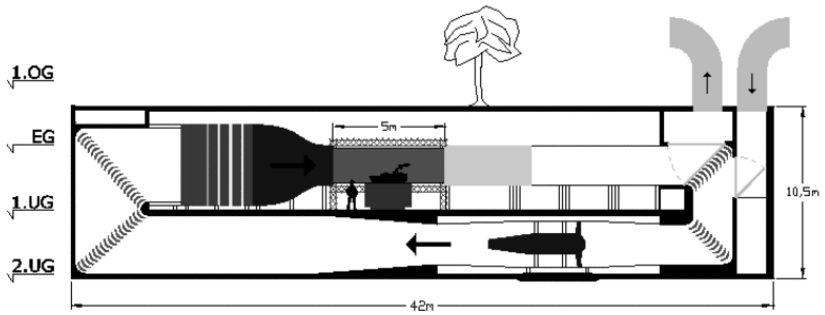

Figure 4.7: Sketch of wind tunnel [39]

Wind loads were measured for both previously introduced vessels, a typical offshore supply vessel (OSV) and a tug (TUG) (see chapter 1, section 1.3). Figure 4.8 shows the arrangement of the models in the test section. The relevant main dimensions of the models are listed in table 4.2.

Table 4.2: Principal dimensions of the wind tunnel models

			TUG	OSV
Model scale	λ	[-]	18	48
Length over all	L_{OA}	[m]	1.76	1.78
Beam over all	B_{OA}	[m]	0.65	0.40
Height over all	H_{OA}	[m]	0.60	0.45
Height of main deck	H_{MD}	[m]	0.12	0.14
Lateral wind area	AL	[m^2]	0.42	0.33

Prior the wind load measurements, the shear flow was measured on the bottom of the test section. Additionally, the flow around the wind tunnel models was visualized by a laser sheet. The influence of heeling on the wind introduced forces was tested with the tug model. The effect on the total wind loads of movable superstructure has been quantified by considering a crane of varying position and orientation on the main deck of the OSV.

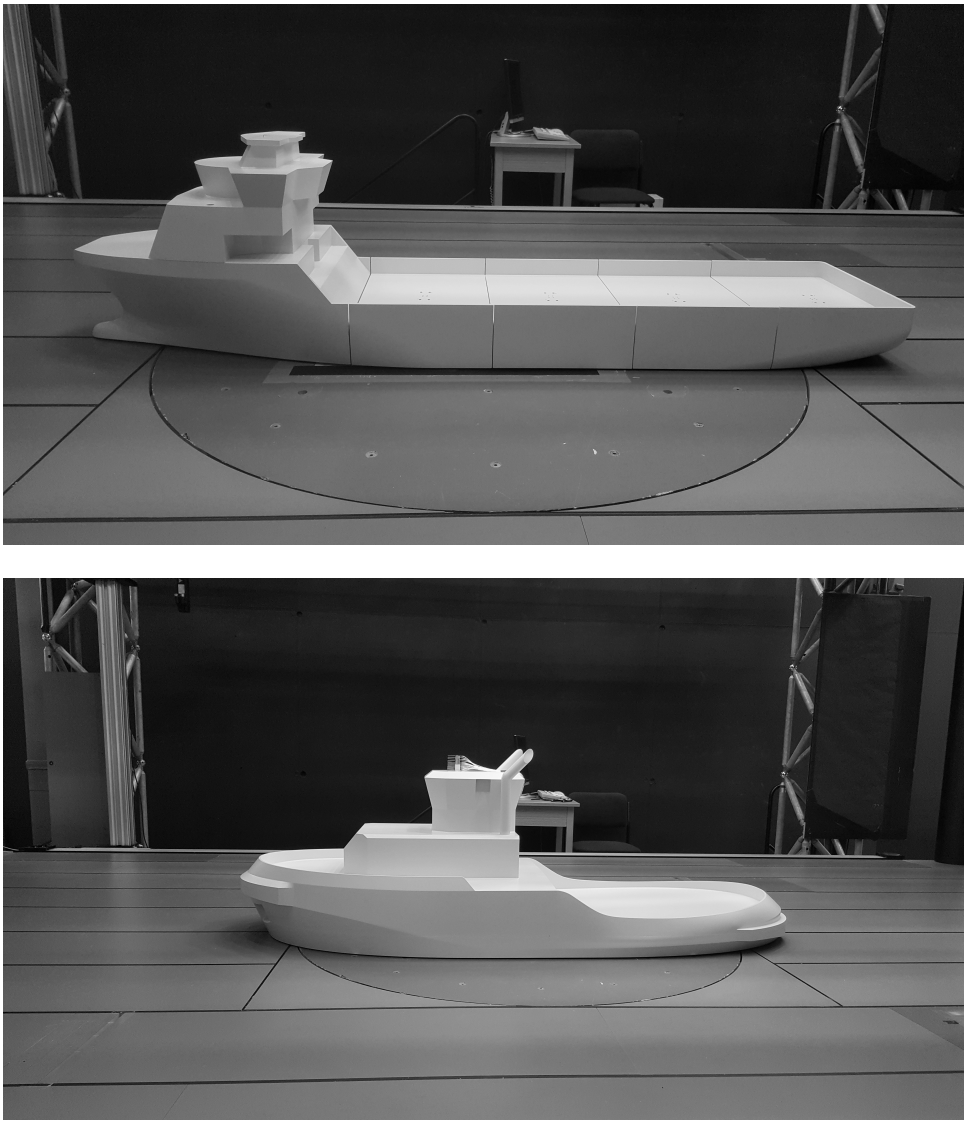

Figure 4.8: Model of an OSV (top) and a tug (bottom) mounted in the wind tunnel

4.2.1 Experimental setup

The wind tunnel models were connected to the load balance with a small shaft. The balance is pivoted so that the encounter angle of the incoming wind can be controlled by a precise motor gear. The experimental setup is shown in a sketch of figure 4.9.
In order to avoid any frictional effects at the connection with the floor of the test section, a small gap of 2-3mm height between the model and the floor has been realized. The models were

manufactured hollow from the inside so that no negative pressure arises in the air gap and thus influences the measurement.

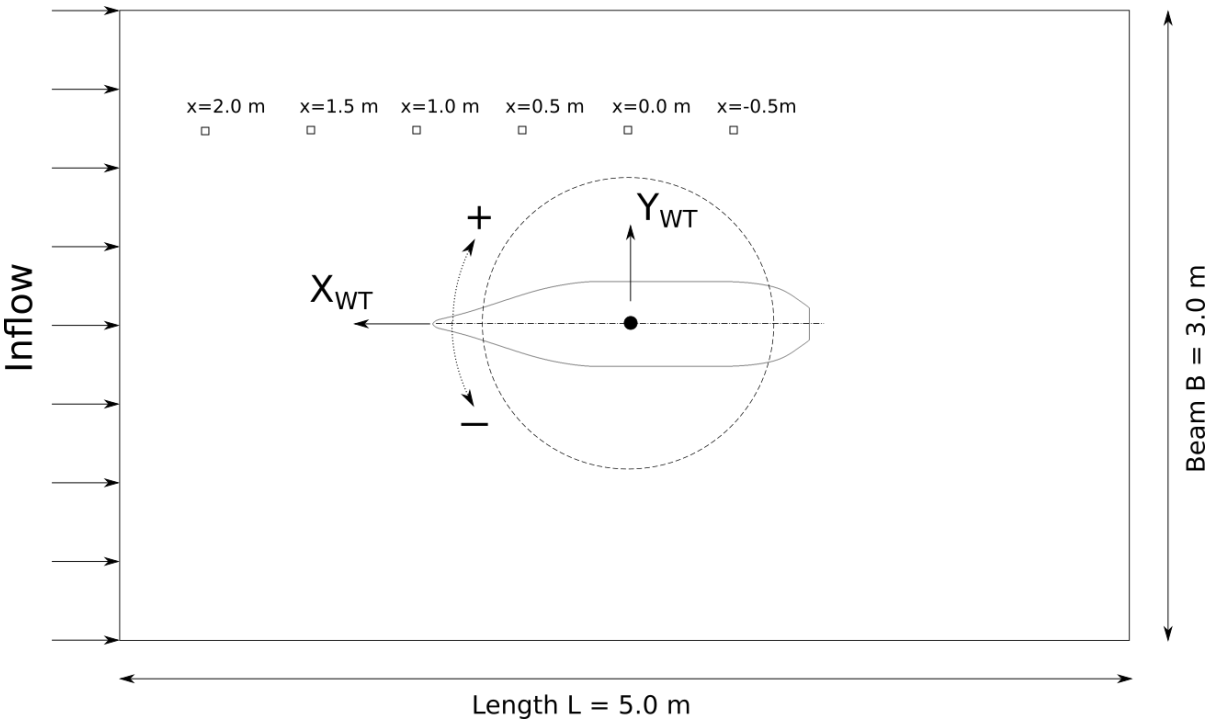

Figure 4.9: Sketch of test section and location of the shear flow measurements on the floor

4.2.2 Preconditions

In preparation for the experiments, tests and measurements were carried out to analyse the flow in the wind tunnel and on the model.

4.2.2.1 Bottom boundary layer of the wind tunnel

In order to appraise the influence of the boundary layer of the test section, a measurement of the wind speed at the wind tunnel bottom has been conducted. The velocity distribution was derived from an arrangement of 16 pitot tubes ranging from $z_0 = 1mm$ up to $z_{16} = 95mm$. The distribution was measured at six positions (sketched in figure 4.9) and each with three velocities: $v_w = 10.0m/s, 15.0m/s, 20m/s$.

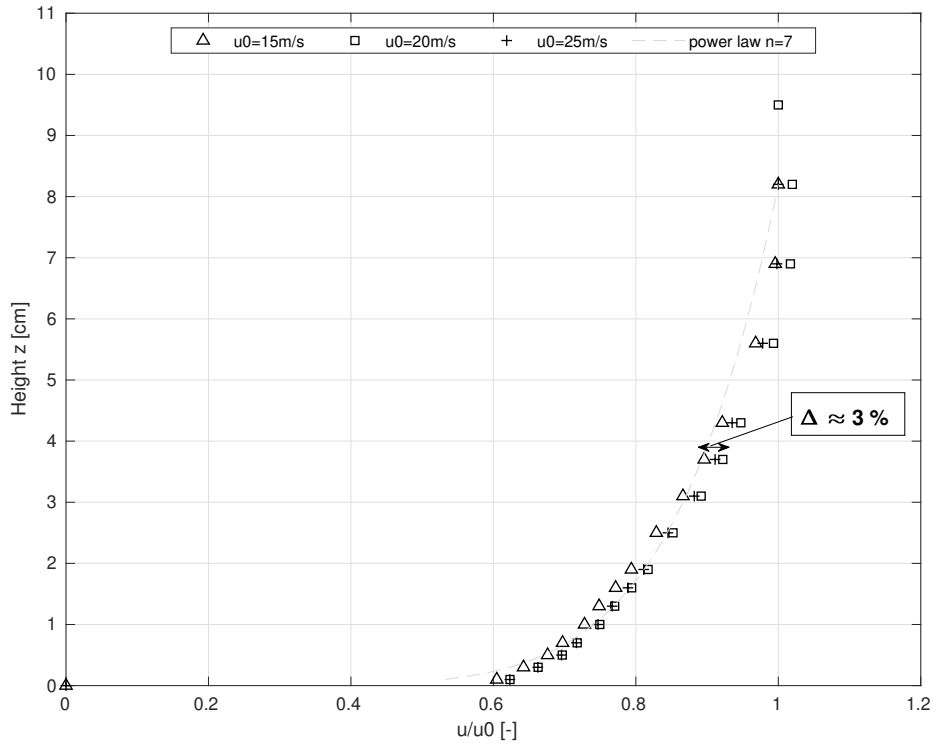

Figure 4.10: Comparison of the mean velocity in the boundary layer of the wind tunnel test section at pivot point (x=0.0m)

A measurement of the velocities at the pivot point of the test section for all three tested inflow velocities in normalized form is shown in figure 4.10. The wind speed was measured for a time span of $\Delta t = 10sec$. A deviation of approximately 3% is obtained by comparing the normalized velocities at the corresponding heights. The wind profile at the exemplified test location can analytically be approximated by the power law with an exponent of $n = 7$

$$u(z) \quad = \quad \left(\frac{z}{\delta}\right)^{1/n}, \tag{4.32}$$

where δ is the height of the boundary layer. Assuming an undisturbed flow continuing from the upper measuring level, the turbulent boundary layer measures about $\delta_{measured} \approx 7cm$.
A common approach for accounting the turbulent boundary layer is the analytical solution of the flow on a flat plate. By comparing both results a discrepancy is obtained. From analytical approach and assuming a turbulent layer from the beginning of the test section, the boundary layer constitutes approximately

$$\begin{aligned} \delta_{turb} &\approx 0.37 \cdot \frac{x}{\sqrt[5]{Re_x}} \\ &\approx 0.37 \cdot \frac{2.5m}{\sqrt[5]{\frac{20.0m/s \cdot 2.5m}{1.5E{-}5m^2/s}}} \\ &\approx 4.6cm \end{aligned} \tag{4.33}$$

with a distance of the inlet of the test section to the pivot point of $l_{pivot} = 2.50$ m and an inflow velocity of $v_w = 20.0 m/s$. This deviation may be caused by small obstacles, such as edges of floor plates or the roughness.
The boundary layer of the test section effects the pressure distribution on the model an thus the wind loads. Thus the measurements have to be corrected. The ratio of the height of the model to the boundary layer is decisive for the effect on the wind loads and hence the correction. The mean heights of the superstructures are listed in table 4.3.

Table 4.3: Mean height of the lateral wind area

	OSV	TUG
$\bar{H}$	0.187	0.241

According to Blendermann [11] the influence of the turbulent layer on the lateral force can be quantified by a comparison of the reference dynamic pressure and the pressure of the ambient undisturbed flow:

$$\frac{q_{ref}}{q_0} = 1 - k_q \cdot \frac{2}{2+n} \cdot \frac{\delta}{\bar{H}}. \tag{4.34}$$

For the models the following corrections are obtained under consideration of the measured boundary layer with n=7:

$$\frac{q_{ref}}{q_0}^{OSV} = 0.950 \tag{4.35}$$

$$\frac{q_{ref}}{q_0}^{TUG} = 0.961 \tag{4.36}$$

This means that the lateral forces of the OSV needed to be increased by about 5% and of the TUG by about 3.9%. Taking the analytical height of boundary layer into account the corrections may be about 3.2% for the OSV and 2.5% for the TUG.

4.2.2.2 Flow around the superstructure

The coefficient based computation of the wind loads underlay the assumption of an undisturbed flow. In case of the installed DP system on board, the model depend on the wind sensors that are positioned i.e. on top of the superstructure. Due to the blockage of the structure and the friction of the surface a boundary flow develops. A measurement of the flow on the top of the OSV's deck house illustrates the influence of the structure.
On the left side of figure 4.11 the measurement setup with the pitot tubes on top of the deck house is shown, as well as the resultant velocity distribution in a polar diagram on the right side. In the diagram the vertical position is considered by the radial distribution, the encounter angles are marked in 15 degree steps. The velocities are represented by colors and isolines.

Herein, red denotes an undisturbed flow, green marks the areas of zero wind speeds and blue areas indicate a backflow.
The measurement indicates that an undisturbed flow area (assuming $v \geq 0.95 \cdot v_w$) is met at a height of about $z \geq 1.5m$ above the roof of the deck house in fullscale. Strong backflow areas can be observed at encountering wind from quartering astern, due to the sharp edges of the roof. Another area of wind reduction and backflow is obtained for head winds. However, the impact is not as high owing to the introduction of a large radius on the roof.

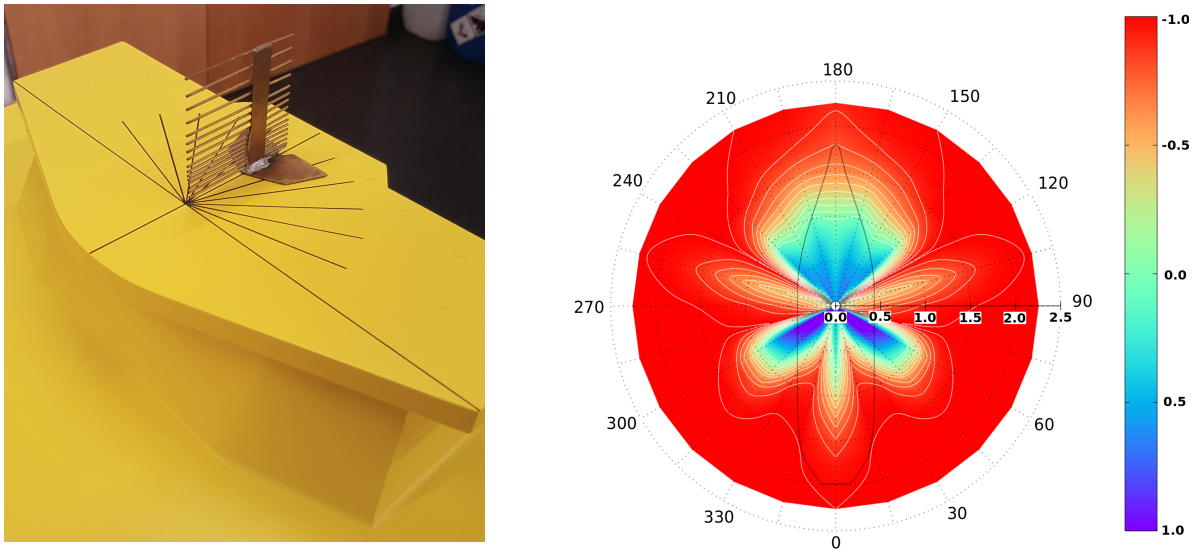

Figure 4.11: Arrangement of the pitot tubes for measuring the velocity profile on the deck house of the OSV model (left), polar diagram of the normalized velocity distribution (right)

The flow around the superstructure has been visualized by a smoke lance and laser sheets. Figure 4.12 indicates the transition between the undisturbed flow and the flow of the boundary layer of the TUG model.
Another visualization of flow phenoma is shown in figure 4.13. The tubes of the funnel of the TUG model introduce a vortex that can be observed in the lateral plane. The unsteady vortex develops for wind encounter angles between 60 and 70 degrees and around 130 degrees. The wake field of the flow behind the deck house of the OSV model is visualized on right side. The smoke lance is placed on the back wall. The air stream transports the smoke upwards to the transition of undisturbed flow and the wake the structure. A turbulent flow is expected in this area.

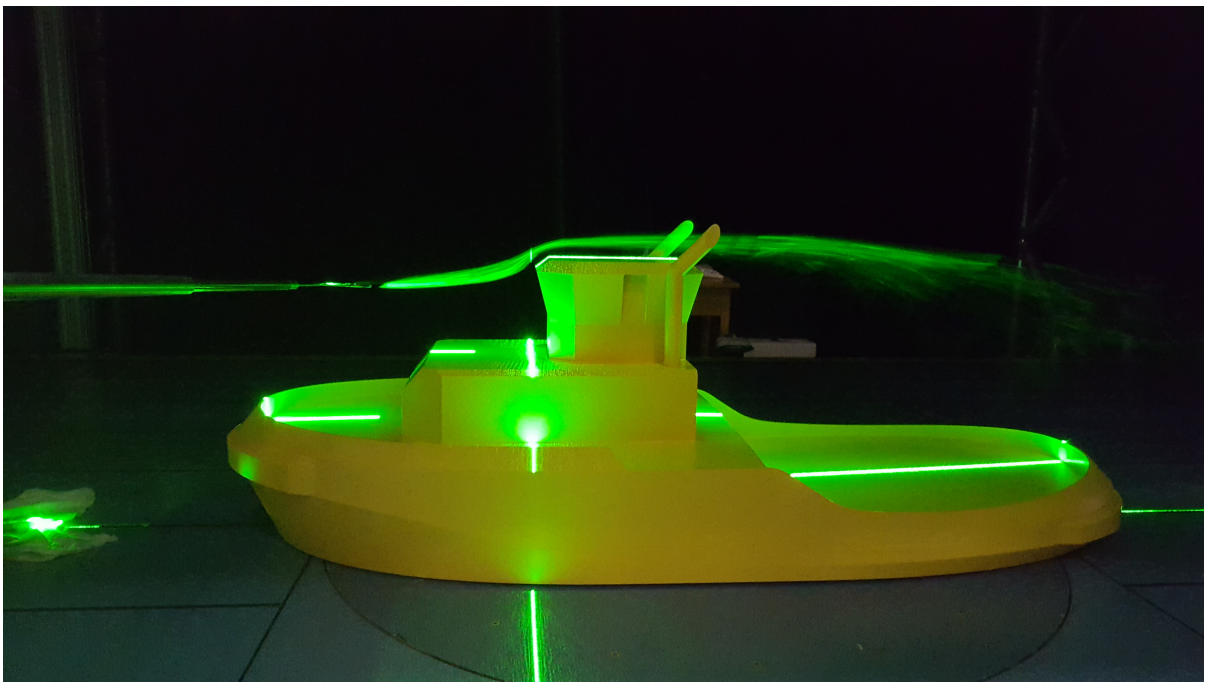

Figure 4.12: Visualization of the TUG model boundary flow

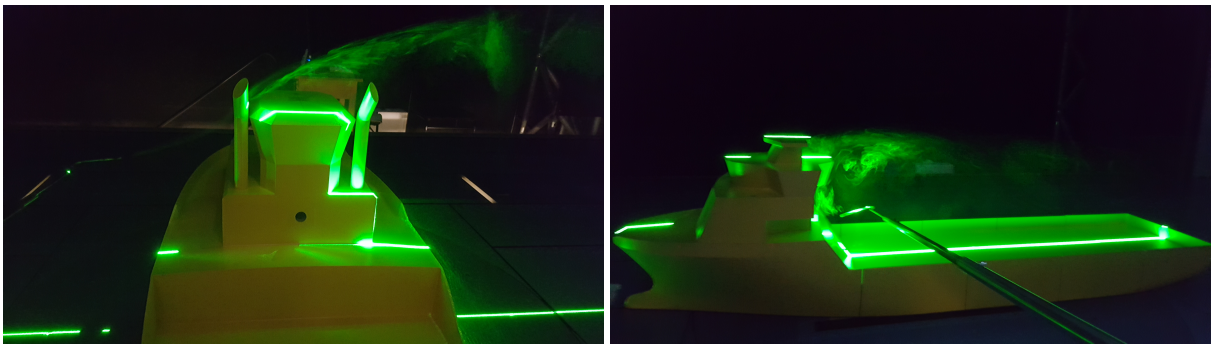

Figure 4.13: Visualization of turbulent flow at the tug's funnel (left), wake behind the deck house of the OSV (right)

4.2.3 Results of the wind tunnel experiments

A large number of experiments were conducted with the intend to elaborate the uncertainty of wind tunnel experiments for wind loads. The influence of the following aspects have been assessed:

- Various flow effects lead to fluctuating wind loads, e.g. flow separation at sharp edges and turbulent flow. Therefore, the time windows for the averaging may have influence on the results.

- The underlying wind speed of the test may have influence on the flow separation due to the variation of the Reynolds number.

- The wind encounter angle in the wind tunnel is set with continuous flow. The flow separation can be different for large and for small change of angle as well as for the sense of rotation.
- The measurement setup can have influence on the quality. Here, a set of repeated measurements were conducted

4.2.3.1 Uncertainty caused by time window

In order to assess the influence of the length of the time window for the evaluation of the wind loads, three time spans were investigated: Δt = 10sec, 15sec and 20sec. In table 4.4 the mean wind loads for the longitudinal and transversal direction are summarized ($\epsilon = 140°$). The evaluation shows a difference of 0.25 % for the longitudinal force and about 1.7 % for the transverse force, which is is range of repeated measurements. The fluctuation about the mean transversal loads is illustrated in figure 4.14. The loads vary with approximately 25 %. For further investigations, a time interval of Δt = 10 sec was chosen.

Table 4.4: Mean wind loads

Δt [sec]	FX [N]	FY [N]
10	24.129	45.678
15	24.075	46.433
20	24.067	45.998

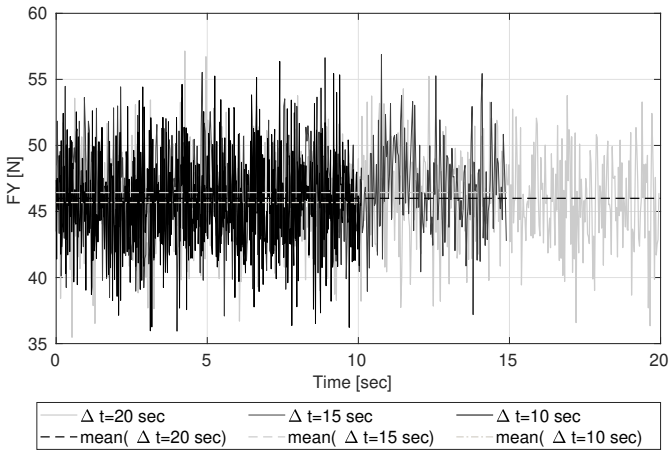

Figure 4.14: Time series of transverse wind loads

4.2.3.2 Dynamic effects during wind load measurements

In order to measure the wind loads at different wind encounter angles, the model was rotated in the test section. Although the measurement for each encounter angle was processed in a sufficient time window, dynamic effects were obtained for critical angles of attack, i.e. encounter angles where vortices detaches (compare representation of votices on TUG model in figure 4.13 (left)). Between each rotation and measurement a time span of $\Delta t = 5sec$ has been applied. Depending on the sense of rotation and the angle increment of the model, vortices behind the structure may be attached to the seperation point longer. Therefore, additional measurements

were carried out for the TUG model to quantify this effect on the wind loads.
The results of the additional measurements are shown in figure 4.15. On the left side, the angle increment has been varied from $\Delta\epsilon = 2deg$ to $\Delta\epsilon = 15deg$. The transversal force FY (model fixed) experiences an abrupt reduction between the encounter angles of $\epsilon = 60deg$ and $\epsilon = 70deg$, as it is typically the case when a vortex detaches. A comparison between the measurement with $\Delta\epsilon = 2deg$ and $\Delta\epsilon = 5deg$ show a difference of $\Delta FY \approx 6\%$. Two observations lead to the assumption that a vortex detachment is involved: While the abrupt reduction of the force takes place in case of the increment of $\Delta\epsilon = 5deg$ the smaller angle increment reveals a reduced drop in force at a higher encounter angle. The deviation of the measurements at $\epsilon = 60$ deg and $\epsilon = 75$ deg almost vanish.

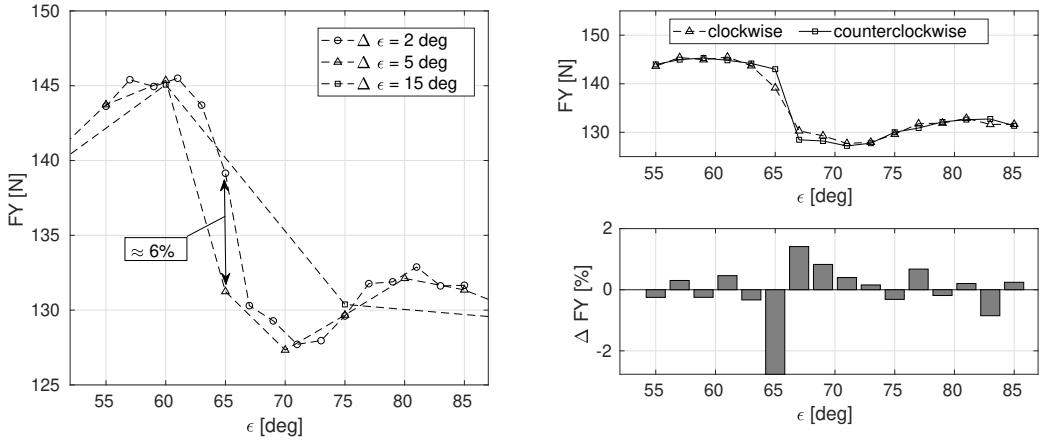

Figure 4.15: Effect of angle increment (left), effect of sense of rotation (right)

The sense of rotation for the same encounter angles again illustrate the effect of a vortex detachment. The counterclockwise sense of rotation denotes the rotation from lower to higher angles of attack. The difference between both rotation senses result in more than 2%.
The results of further measurements for the OSV model are shown in the figure 4.16. Here, both directions of rotation were tested with three repetitions each. The absolute deviations are represented in the corresponding figures at the bottom. In case of head winds ($\epsilon \approx 120deg$) the deviation for the transversal load and the roll moment between counter-clockwise and clockwise rotation are of higher magnitude compared to the average. The largest deviations from the mean are found for CX with 4.6 %, CY and CK with 2.3 % each and CN with 1.9 %.

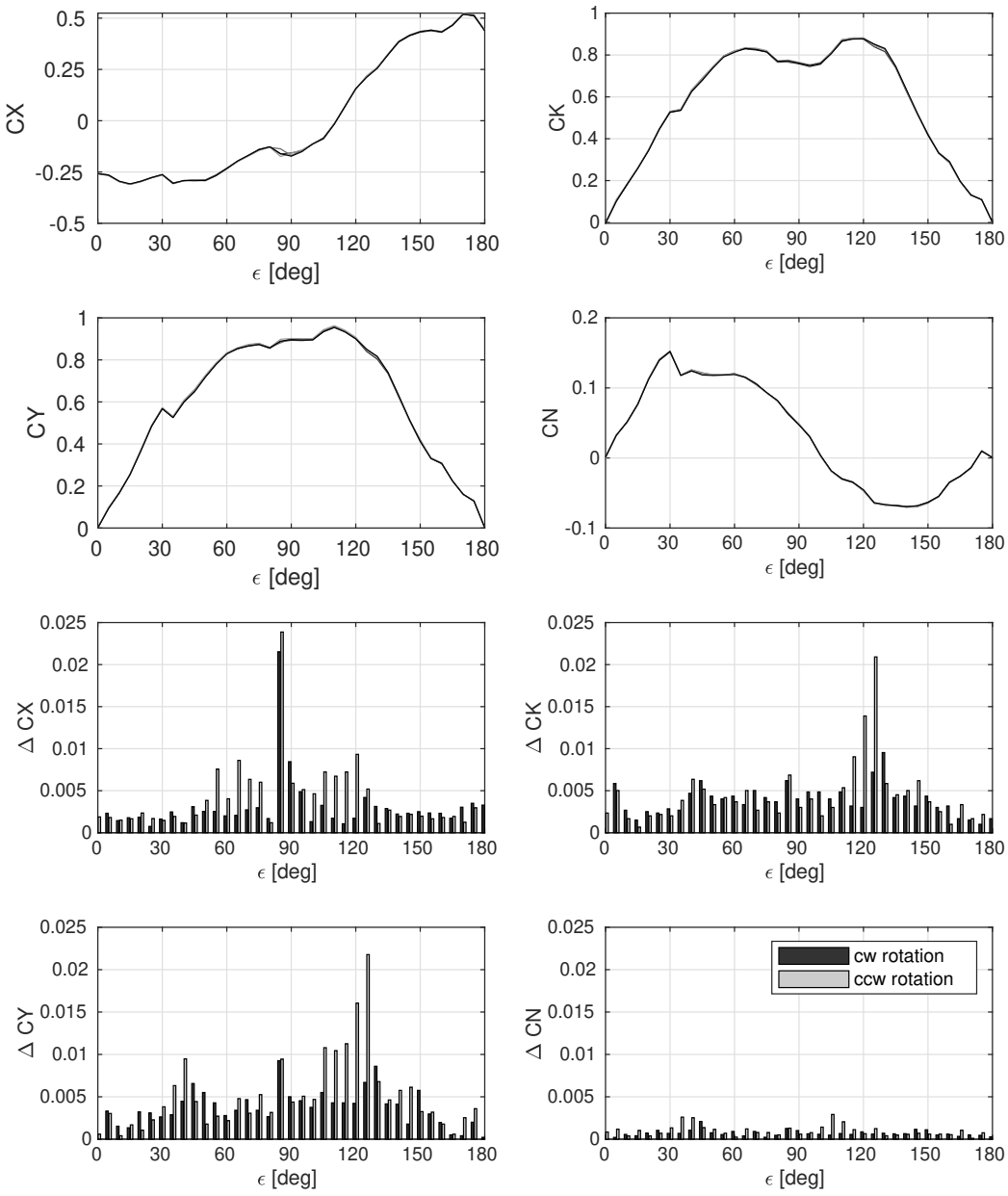

Figure 4.16: Absolute deviation from repeated measurement of wind loads at $v_w = 20m/s$ (OSV)

4.2.3.3 Influence of wind speed

The forces on the TUG model were measured at four different wind speeds to determine the influence of the Reynolds number on the wind loads ($Re = 0.95, 1.4, 1.89, 2.37\ x10^6$). A summary of the whole range of wind encounter angles and inflow velocities is given in figure 4.17. The greatest influence is observed for the transverse load and the rolling moment in oblique wind from astern. For these force components, deviations of 16.6 % for CY and 17.7 % for CK result. The influence of the speed on the longitudinal component CX is relatively low at 6.8 %. The lowest deviation was measured for the yaw moment CN with 3.3 %.

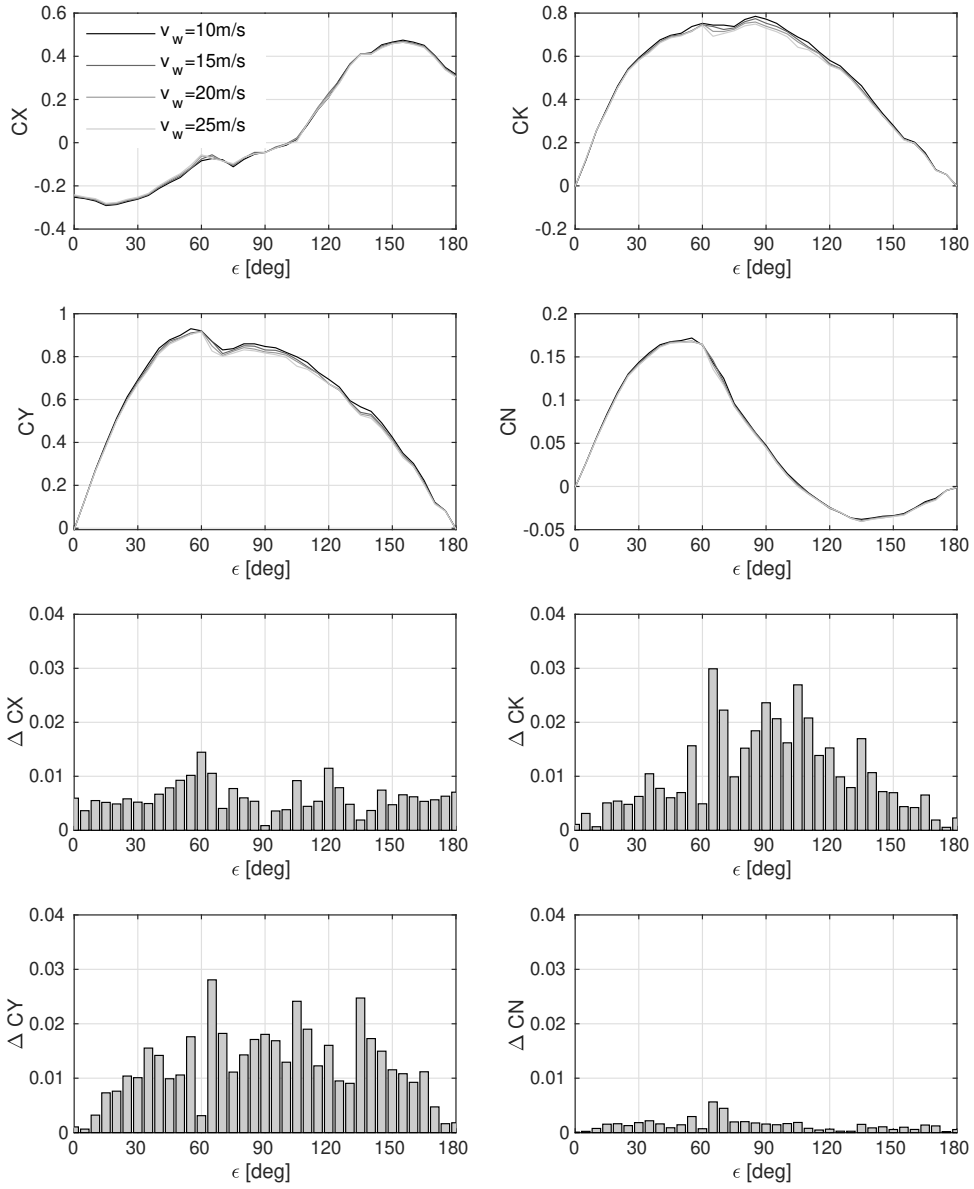

Figure 4.17: Absolute deviations of the force measurements in repeat measurements (TUG)

4.2.3.4 Influence of heel

During DP operation roll motion are expected. The current approach does not include varying wind load coefficients due to heeling. However, experiments were conducted to quantify the influence. The influence has been measured with the TUG model. Three separate wedges of 0, 5 and 10 degrees were mounted on the bottom of the model (see figure 4.18).

Figure 4.18: Tug in heel condition

The measured wind load coefficients for all three conditions are summarized in figure 4.19. For the estimation of the coefficients the ship parameter of the upright condition has been used for all heelings. The influence of the heeled conditions is asymmetric since the model is lowered to the windward side for negative encounter angles and raised for positive encounter angles.

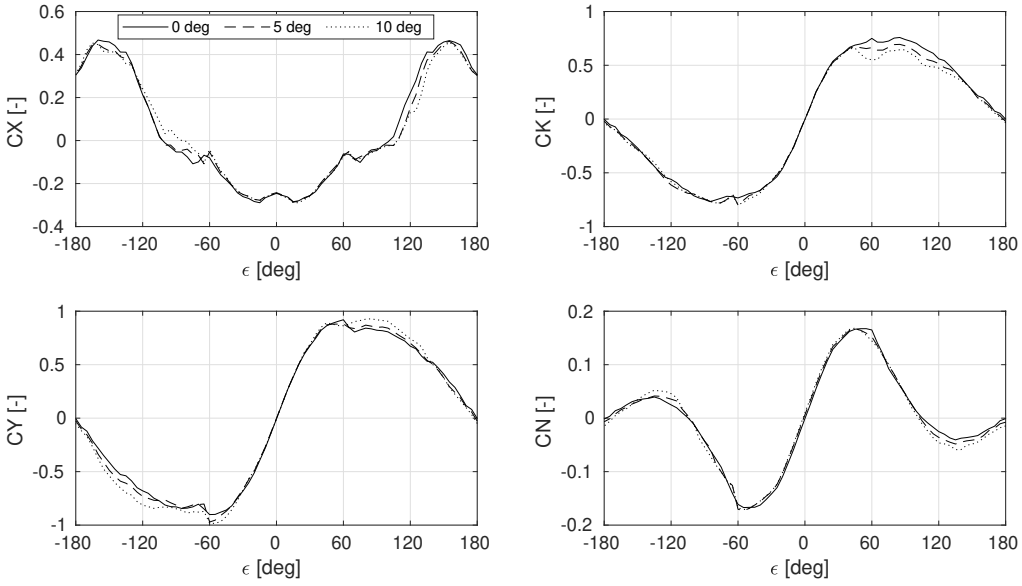

Figure 4.19: Influence of heeling on the wind load coefficients

The strongest effect on the forces are obtained for oblique conditions from front and aft winds. The absolute differences are comprised in figure 4.20. In order to quantify the the influence, the absolute deviations were set in relation to the respective maximum forces. The longitudinal force and the roll moment experience with 16.2% and 13% the strongest impact. However, the deviation for the longitudinal force does not follow a clear trend. This may be caused by turbulent flow of higher intense. Though, for the transversal forces, higher forces are obtained for increasing heeled conditions. The same holds for the yaw moment. For the deviation of the roll moment the angle of the hull sides is relevant.

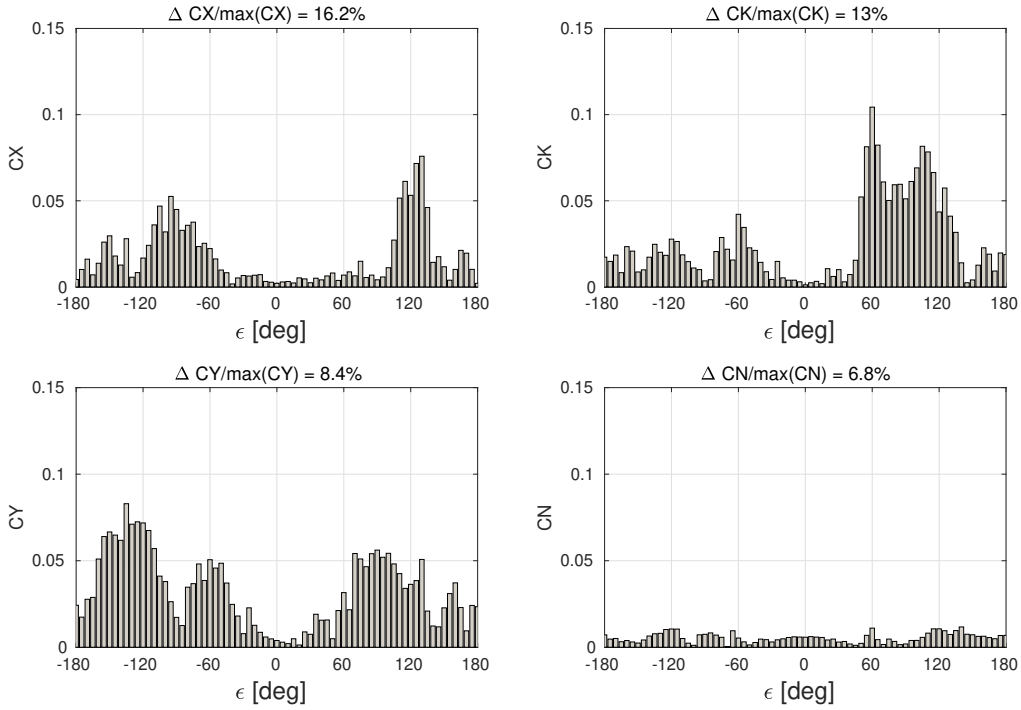

Figure 4.20: Absolute deviations of the force coefficients due to heeling influence

4.2.3.5 Influence of a mounted crane on the working deck

Offshore supply vessels and other service vessels are typically designed with a working deck for the transport of container units and other equipment from and to offshore platforms. The loading represent additional wind resistance and hence the wind loads may vary significantly. Further, the deck can be equipped with a crane or an A-frame at the aft part.
Additional measurements in the wind tunnel were carried out to determine the influence of a crane mounted on the working deck. The location of the crane and the orientation of the extended arm has been varied. In figure 4.21 the arrangement of the aft location is illustrated. The longitudinal position has been varied in four steps from the aft end of the deck house up

to the position represented on the figure.

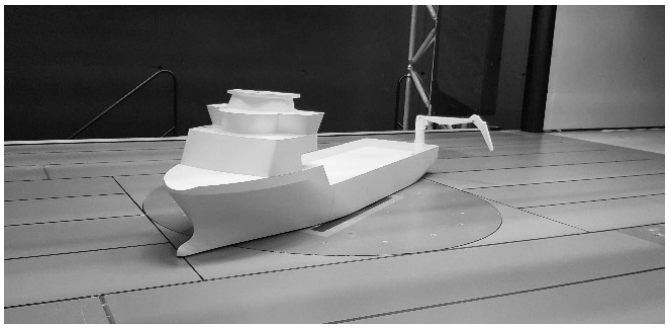

Figure 4.21: Crane arrangement on main deck

The resultant wind load coefficients are shown in figure 4.22. The line with squares indicate the loads without the crane, whereas the error bars denote the deviation range of all measured crane positions and orientations. The influence vary for each force component. For the yaw moment, the highest deviation is derived with 25.4 %. The smallest effect with about 10% could be observed with the transverse forces.

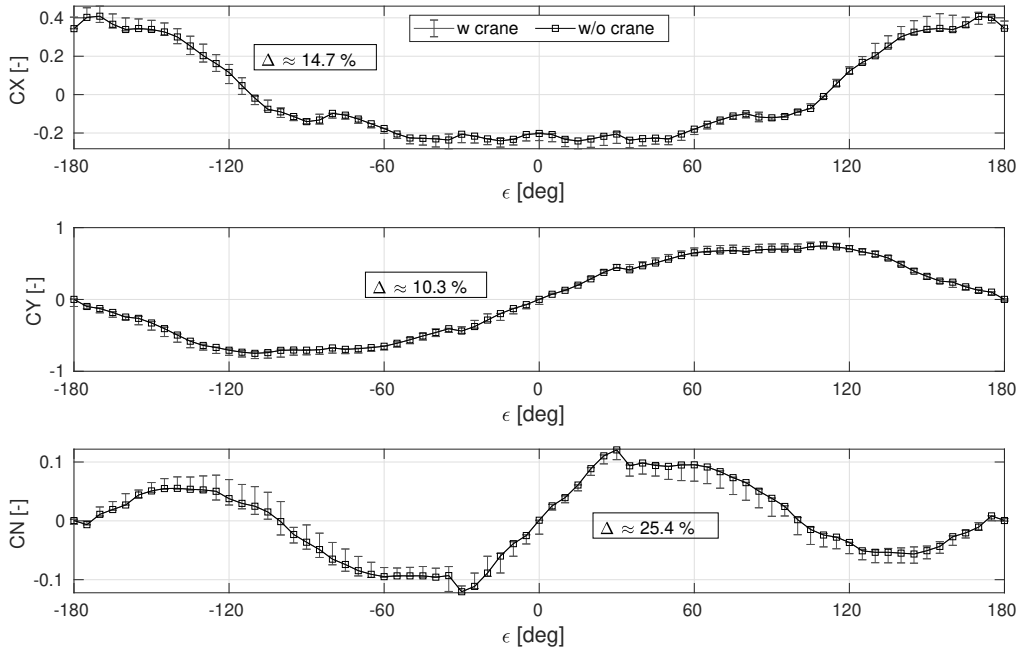

Figure 4.22: Influence of a working crane on the wind load coefficients

4.3 Numerical assessment of wind loads

The aerodynamic of ships is characterized by turbulent flow. Reasons for that are, inter allia, typical flow phenomena of bluff bodies, such as vortex shedding, wake flow and flow separation, as well as three dimensional effects that result from the interaction between reduced flow by friction and accelerated flow by blockage effects. In figure 4.23 typical streamlines exemplify the complex flow field around an offshore supply vessel. Herein, (a) represents a streamline that ends frontal on a wall, (b) shows a circular flow behind the deck house. The lower flow field (c) around the hull can be compared with a flow around a foil with truncated end. The two section planes provide a sketch of the vortex flow that result from lateral flow in interaction with reduced velocity flow behind the deck house (compare (d)).

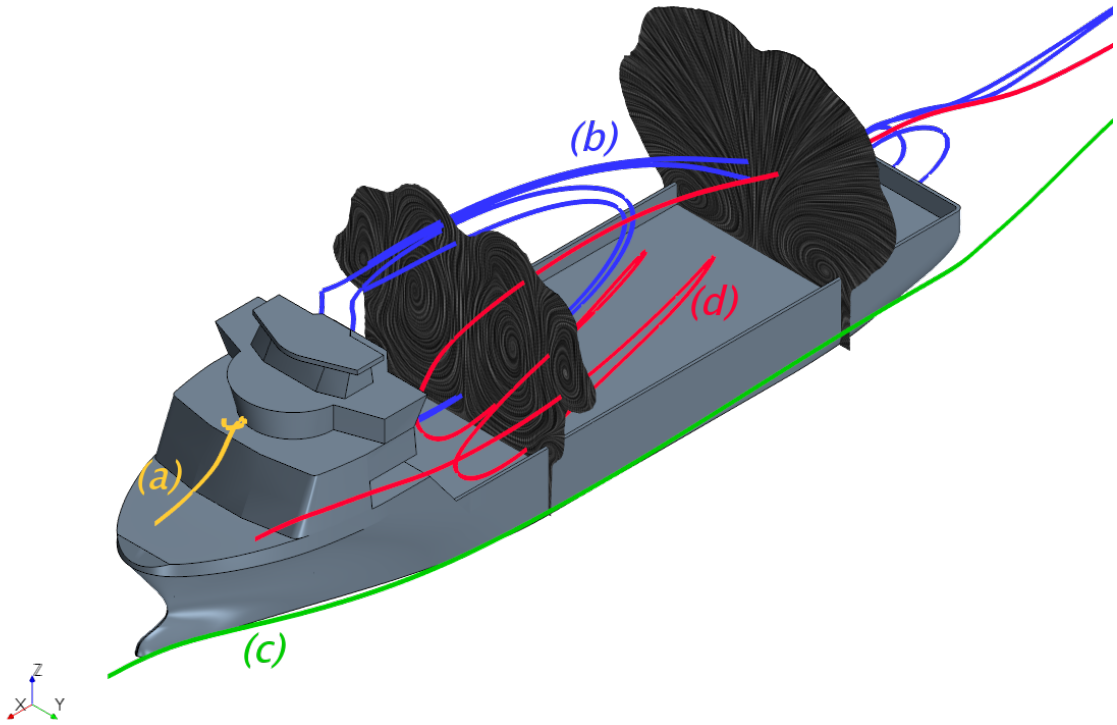

Figure 4.23: Flow field around superstructure of an offshore supply vessel

In the following a validation of an efficient numerical setup for the computation of wind loads is presented. First, the solver and the setup of the computational domain is described. Then, a CFD assessment of the flow elaborates scale effects, wall shear flow of the bottom of the test section and compares different numerical solvers. This section concludes with the comparison of wind load coefficients gained by CFD and EFD.

4.3.1 Numerical setup

For the simulation of the aerodynamic flow around the superstructure the 3D steady-state RANS equations are solved using the control volume method which is described in chapter Fundamentals. The realizable $k-\epsilon$ model is used to provide closure. Second-order discretisation schemes are used for both the convective and viscous terms of the governing equations. The SIMPLE algorithm is used for pressure-velocity coupling and standard pressure interpolation is used.

4.3.2 Computational domain

The size of the domain for the computation of the wind load coefficients was set according to the wind tunnel dimensions. This allows a valid comparison between the wind loads obtained from experiments and from the numerical approach. The blockage influence is assess with different domain sizes and discussed in a separate section.
The domain setup is presented in figure 4.24. At the inflow and the domain sides the velocity is prescribed. The pressure is set to zero at the outlet. The top and the bottom of the domain are modeled as walls, hence the bottom is set to no-slip condition to account for the natural boundary layer influence.

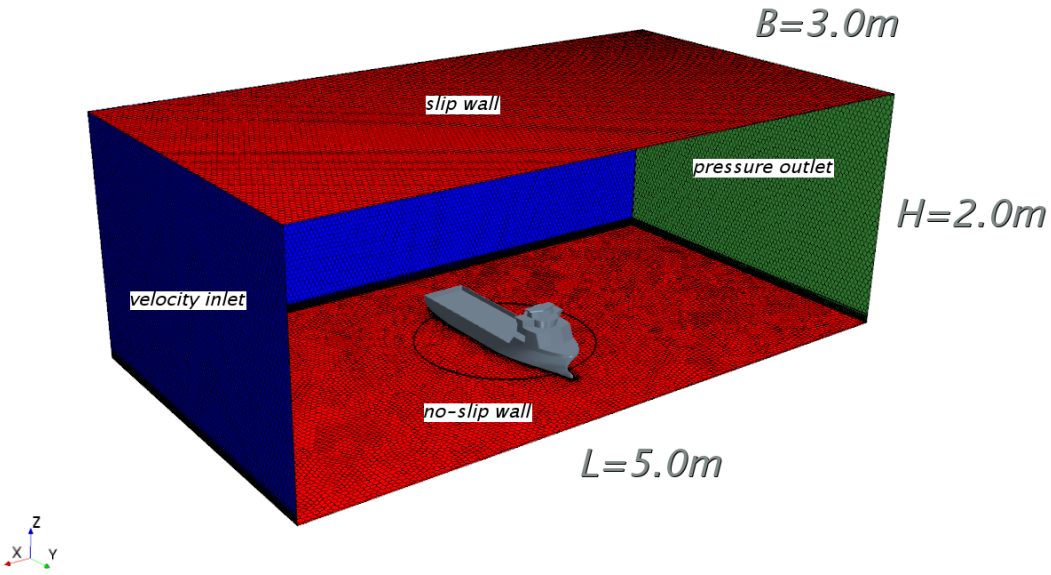

Figure 4.24: Computational domain and boundary condition

4.3.3 Mesh grid study

Two mesh types were investigated: hexaedral and polyhedral mesh type. The most common mesh used for CFD computation using the FVM is represented by a hexaedral mesh type. The applied software StarCCM+ provides a various number of automatic mesh algorithms. The hexaedral mesh can be generated by the trimmed cell mesher which produces a high-quality grid for both simple and complex mesh generation problems. However, polyhedral meshes offer a balanced solution in terms of mesh size and result accuracy for complex mesh generation problems.

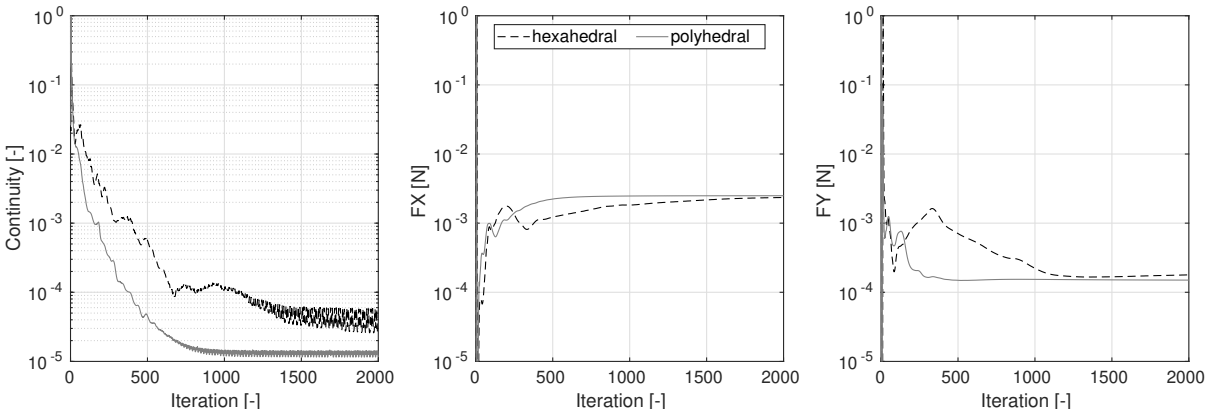

Figure 4.25: Comparison of hexahedral and polyhedral performance for 45 deg

Prior the simulation of all encounter angles a study for various grid settings has been conducted. Figures 4.25 and 4.26 show that polyhedral meshes produce equivalent accuracy results compared to hexahedral mesh types with the following added benefits:

- Faster converge with fewer iterations
- Robust convergence to lower residual values
- Shorter solution runtimes

Two typical grid configurations of the study are depicted in figure 4.28. The hexahedral mesh setup has a three refinement levels volume-cell size in order to maintain the wind speed gradient towards the ships without any dissipation. The refinement for the polyhedral mesh was controlled by a surface growth factor which specifies the maximum size ratio of connected mesh edges.
The grid configuration has an influence on the quality of the numerical solution. Therefore, a grid study has been performed. The result is shown in figure 4.27. The meshes have been successively refined by factor $\sqrt{2}$. The refined cells on the hull were kept constant in order to preserve the same treatment of the gradient velocities. Both mesh types converge and represent a valid setup for the simulation of wind around the superstructure. Because of the benefits of a polyhedral mesh type the setup was chosen for further investigations.

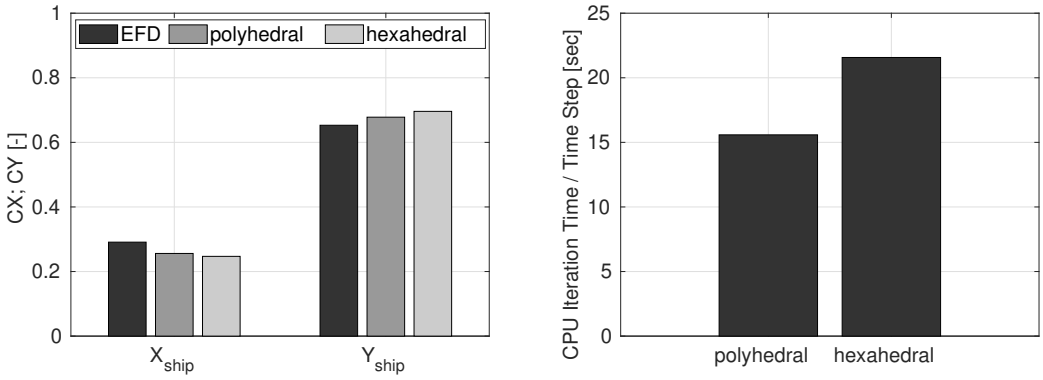

Figure 4.26: Comparison of wind load coefficients for $\epsilon = 45deg$ (left),
CPU performance of different mesh types (right)

Another important parameter of the grid setup is represented by the resolution on the models surface. The cell size on the surface has been varied from 50 cells/ship length to 500 cells/ship length. A good convergence has been obtained for about 350 cells/ship length.

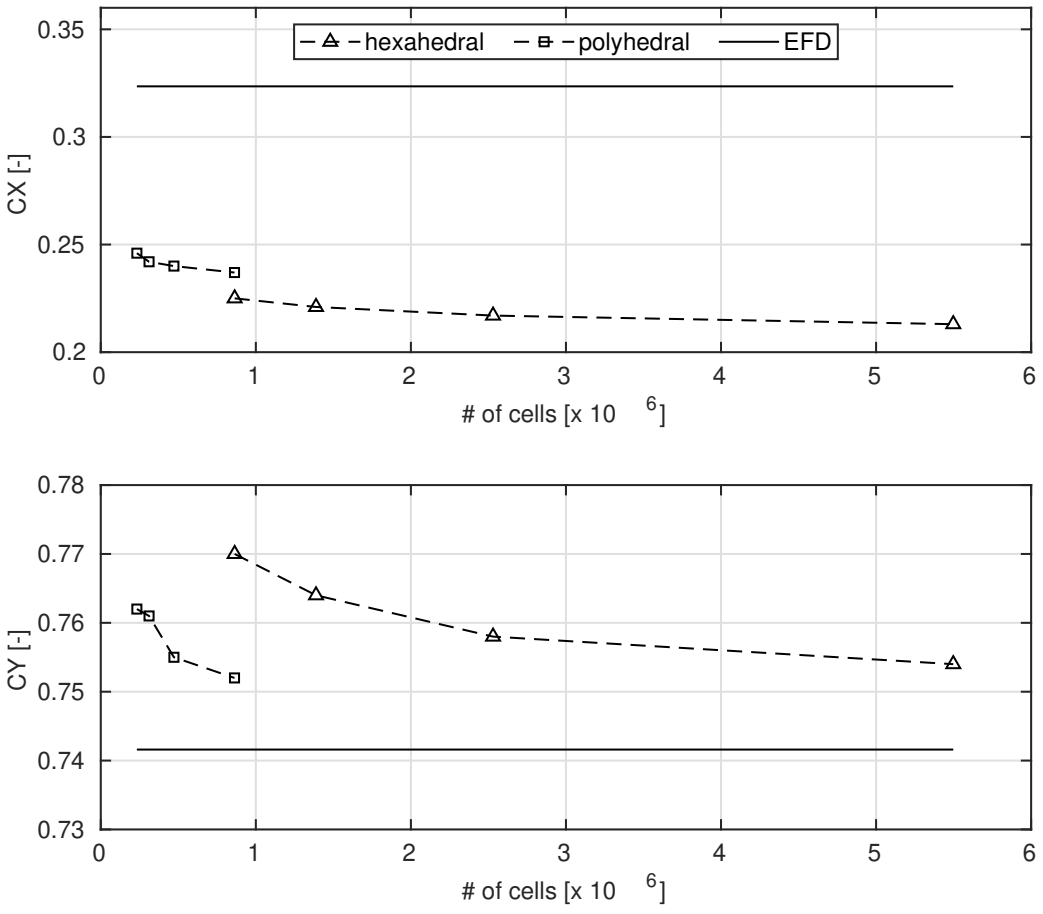

Figure 4.27: Grid study of both mesh types

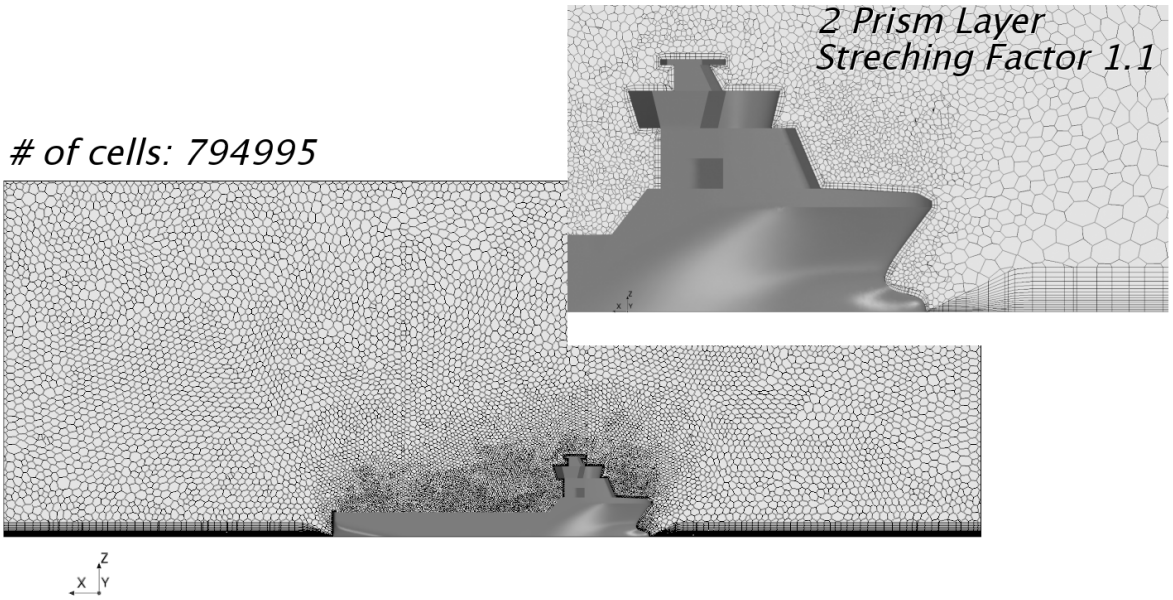

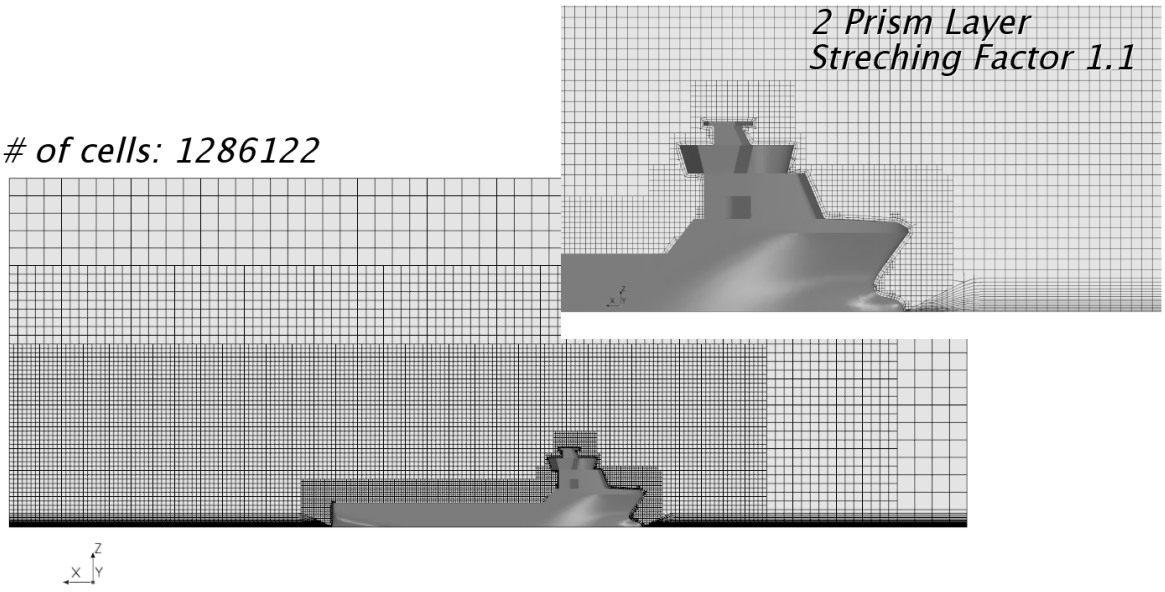

Figure 4.28: Grid configuration with polyhedron cells (top) and tetrahedron cells (bottom)

4.3.4 Influence of wall function

A wall function is used to approximate the flow near the surface of the model. The influence of the dimensionless quantity Y+ for the distance from the wall up to the center of the first grid cell is investigated in this section.
The velocity distribution around the superstructure is characterized by a strong variation in speed. While the wind speed at the leeward side almost vanishes, the velocities at the windward side increase due to the blockage. This makes it very difficult to generate a proper grid at the models surface which meet a wall Y+ value in the range for a high-Re approach, i.e. $30 \leq$ Y+ ≤ 300.
To estimate the influence of the boundary layer grid, a mesh was created on which the forces were calculated for different wind speeds. The mesh was designed with five prism layers with a stretching factor of 1.1, which means that the thickness of each cell layer increases with the specified ratio of the previous layer. The total thickness of the boundary was approximated to $\delta = 0.025m$. A side view of the mesh is illustrated in figure 4.29. The wind speeds varied between $v_w = 5m/s$ and $v_w = 25m/s$.
A threshold of cells with Y+ values in the desired range is represented in figure 4.31. In the simulation with the average of about Y+≈90 the largest number of cells is to be found in the permitted range.

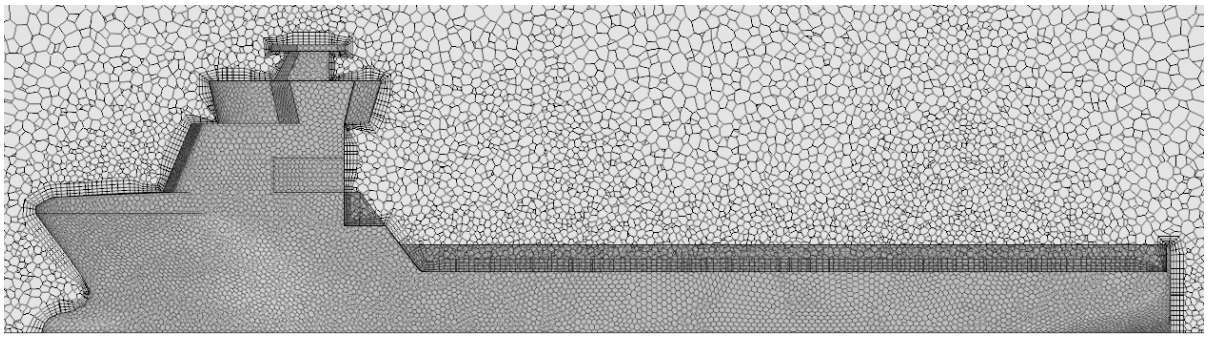

Figure 4.29: Side view of prism layer grid

Another set of simulations was conducted with a fixed wind speed of $v_w = 20m/s$ and a varying prism layer stretching factor . The result of the resultant average wall Y+ values and the percentage of cells in rage is shown in figure 4.30. For both approaches, best results are gained with a Y+ value between 80 and 120, based on the number of cells in range and the wind load coefficients compared to the experiments.

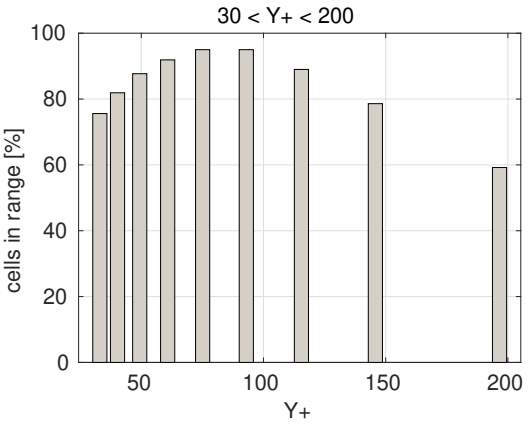

Figure 4.30: Cell distribution of Y+

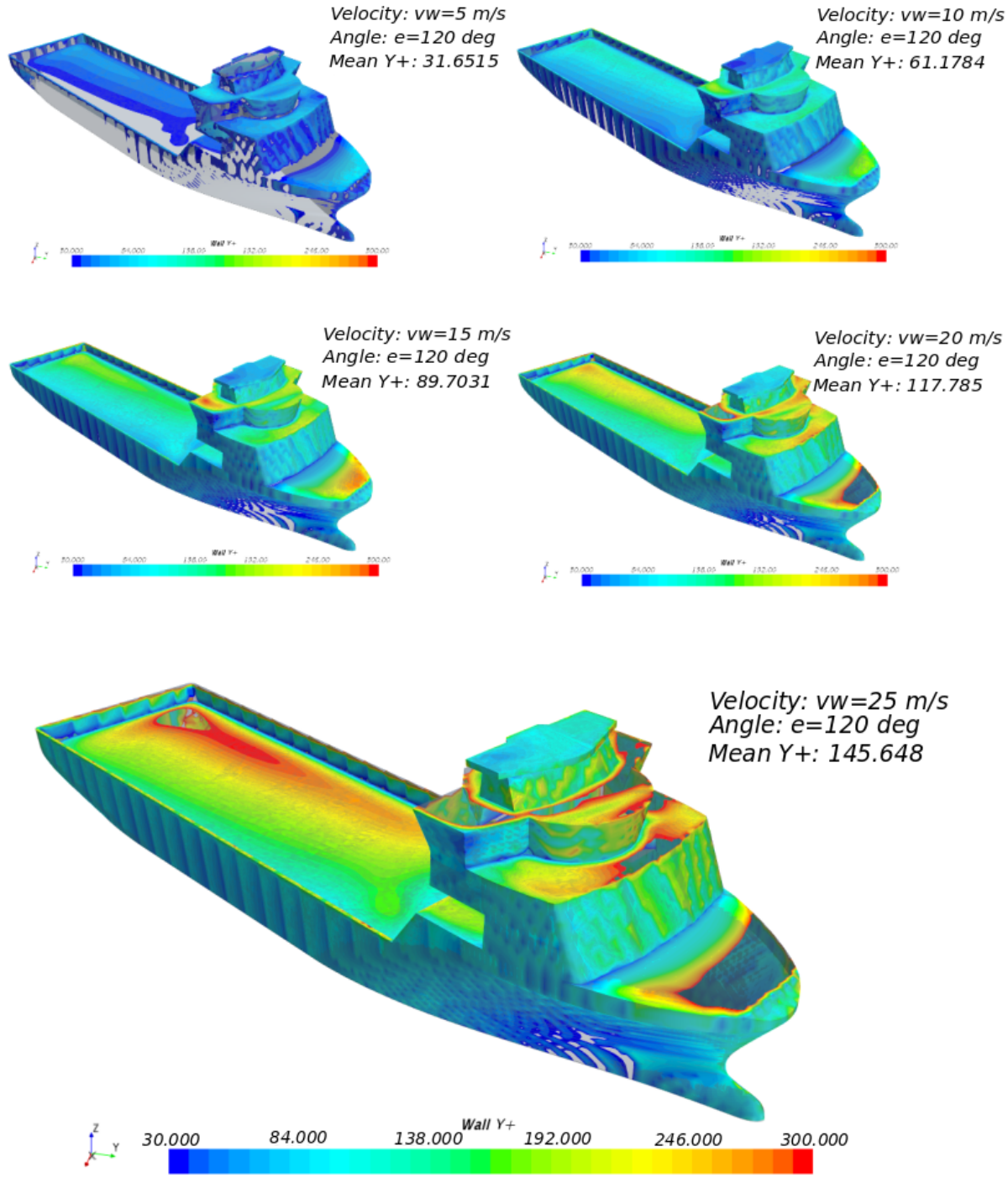

Figure 4.31: Y+ value with varying incident flow velocities and constant boundary layer grid

4.3.5 Influence of the domain size

Although the domain size was set to the di-
mensions of the wind tunnel's test section, the influence of variable domain size was studied. The resultant wind load components of the OSV model for encountering winds of $\epsilon = 135deg$

are illustrated in figure 4.32. According to this observation, the deviation caused by successively increasing the domain size is less than 1 % after the domain size reaches a size four times the model length.

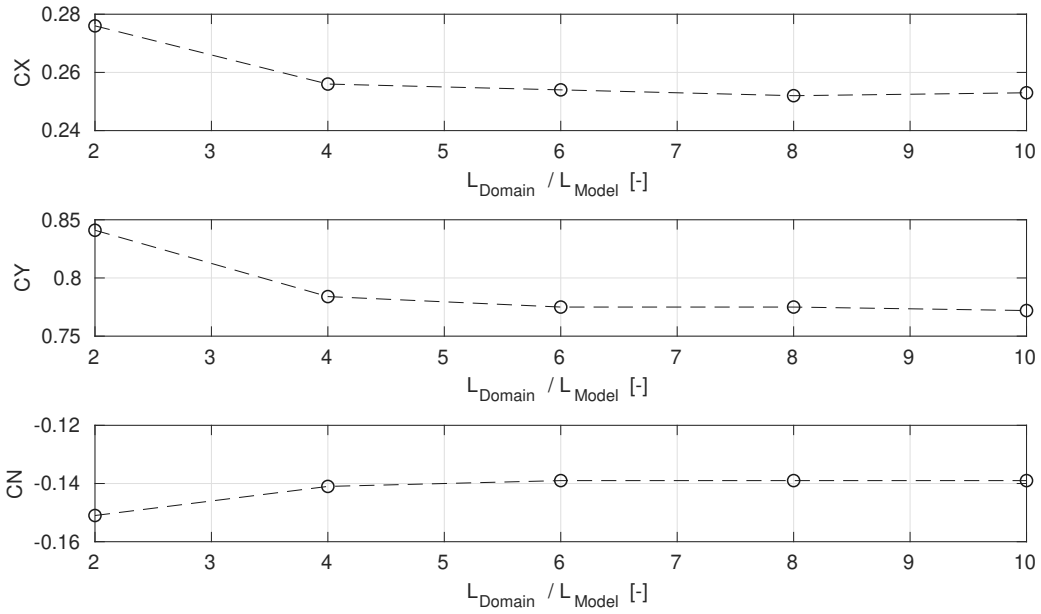

Figure 4.32: Variation of domain size with an oblique headwind

4.3.6 Influence of wall shear stress at test section floor

The influence of the developed boundary layer at the floor of the test section has been approximated according to Blendermann in section 4.2.2.1. Since it is impossible to conduct experiments without a boundary layer on the floor of the wind tunnel, in this section the CFD method has been applied to asses the effect for both, with and without a boundary layer.

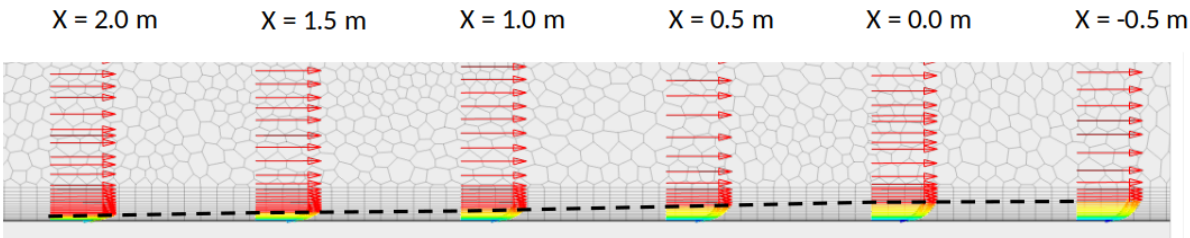

Figure 4.33: Mesh configuration of test section floor

In order to compare the theoretical boundary layer of the CFD method with the actual measured gradient velocities, simulations were conducted without the model present. In figure 4.33 the gradient velocities for each measured location is presented. The dashed line depicts the

increasing boundary layer.

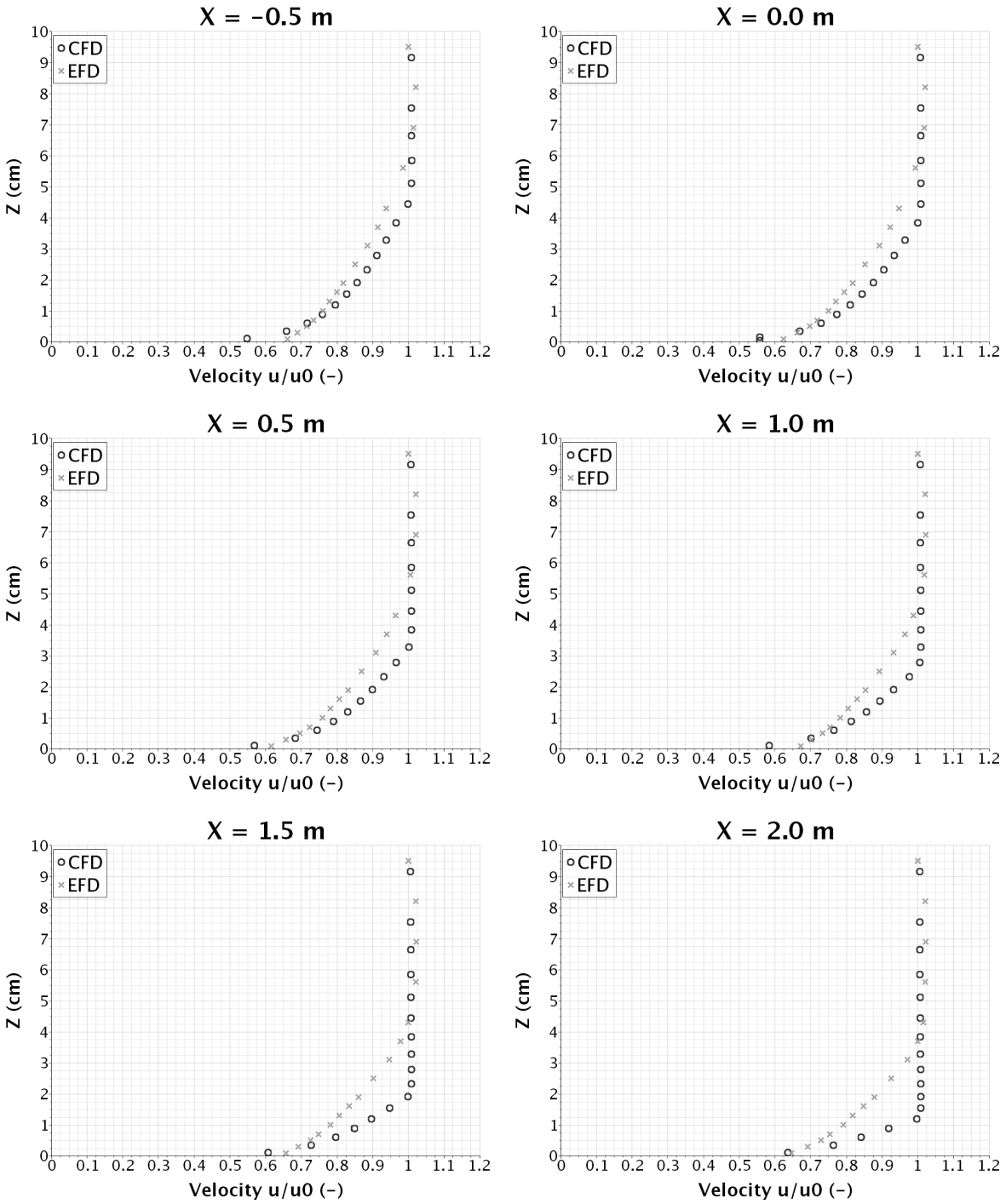

Figure 4.34: Comparison of wind profile

Deviations between the CFD simulation and the measurements were expected, since the velocity distribution follows the all y+ wall function. Adjustments of the CFD parameter were not considered, because the changes also affect the flow on the models surface. In figure 4.34 the

calculated and measured normalized velocities at the measured positions are compared with each other. While the discrepancies are high at the beginning of the test section, the gradient velocities show a fair agreement at the location, where the ship model is set in the wind tunnel ($X = 0.5m$ - $X = -0.5m$). Hence, the velocities obtained from the CFD simulation are over estimated. However, the deviation is less than 10%.

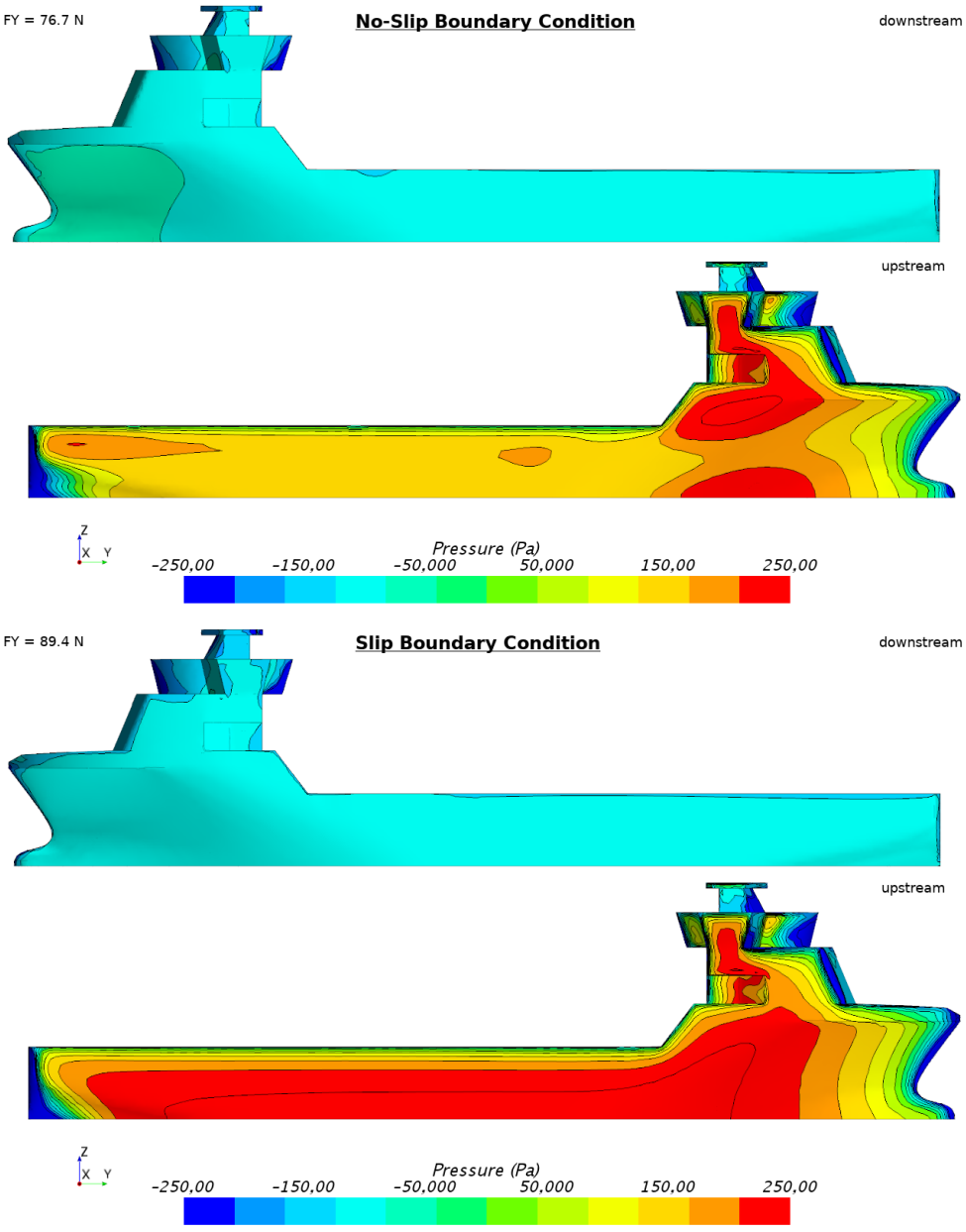

Figure 4.35: Pressure distribution in beam wind with non-slip condition (top) and without (bottom) (OSV)

In figures 4.35 and 4.36 the pressure distribution on the windward and leeward sides with and without the incorporation of the boundary layer for the OSV and the TUG model in upright condition are shown. The pressure contour range is kept identical. The greatest influence is

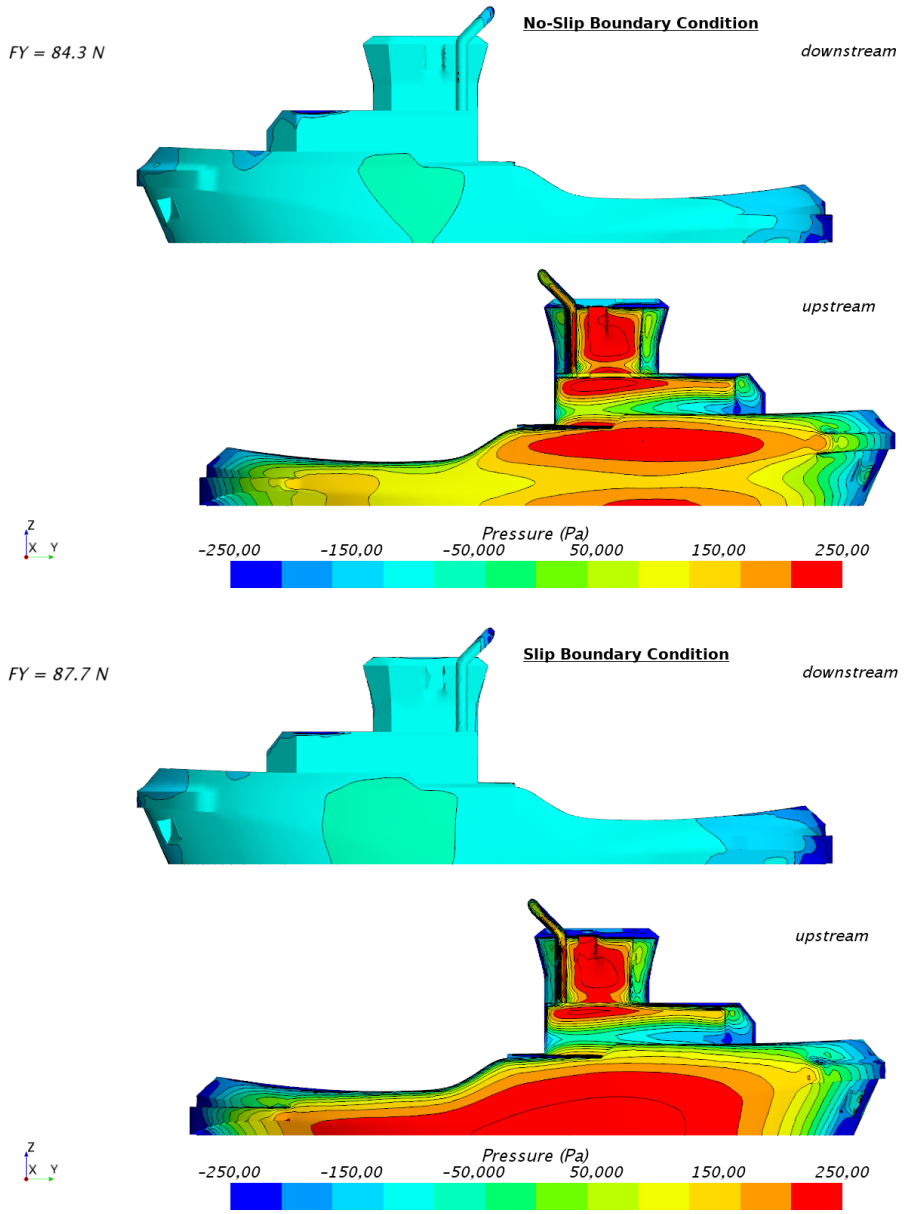

Figure 4.36: Pressure distribution in beam wind with non-slip condition (top) and without (bottom) (TUG)

obtained for the windward side. For both models it is evident, that the highest pressure level extends across the ship length. Further, it can be seen, that parts of the superstructure, that are located above the boundary layer, show a similar pressure distribution. While the main deck of both models have almost the same height, the maximum height of the TUG model is significantly higher. In addition, the deck house of the OSV model makes up about one fifth of the ship's length in contrast to the TUG model where the bridge deck extends over the half ship length. Therefore, the influence of the boundary layer is smaller for the TUG model compared to the OSV. The reduction in the induced pressure result in a deviation of the corresponding lateral force of 14% for the OSV and 3.8% for the TUG model. Caused by the asymmetric

lateral shape of the OSV model a correction proposed in the previous section may not be valid. On the other hand, the correction for the TUG model show a good agreement.
The effects on the leeward side are negligible. However, in the bow section of the OSV model, an effect of the changed flow around the deck house on the pressure distribution is indicated.

4.3.7 Scale effects

For conventional ships the difference in the Reynolds number of model test and full scale is about two orders of magnitude. Deciding flow effects, such as flow separation, may occur at sharp edges which are localized in positions true to scale. Thus, the difference in the Reynolds number will have little influence on the extrapolation of the obtained wind load coefficients from model to full scale, apart from possible wind tunnel corrections.
Possible scale effects were investigated by CFD simulation. Starting from the model scale simulation setup the grid has been successively scaled in three further steps up to full scale measurement. The result of five varying encounter angles is presented in figure 4.37.

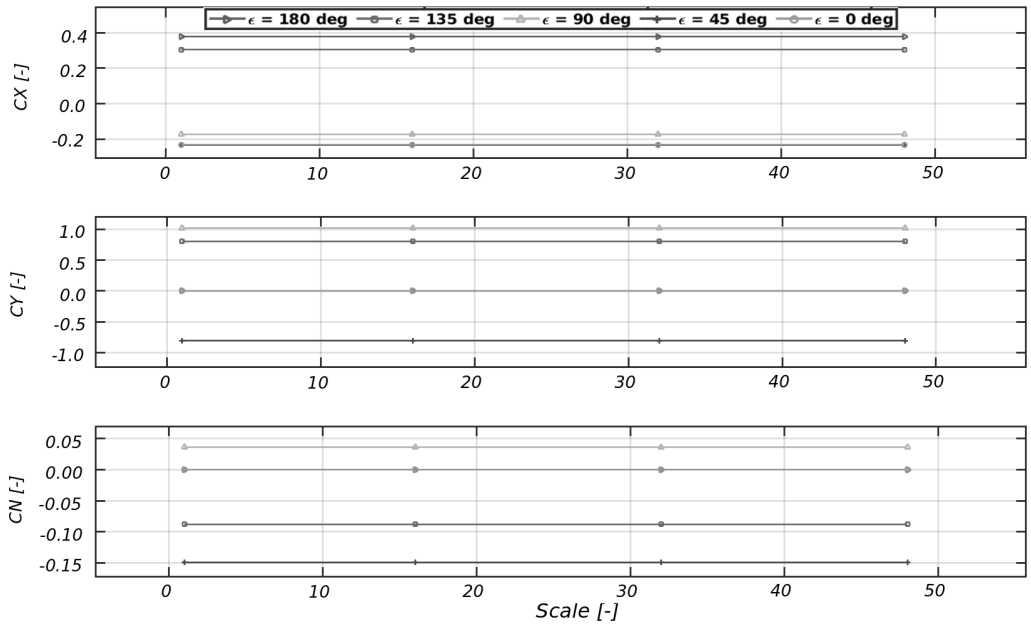

Figure 4.37: Scale effects of the wind load coefficients of the OSV for varying encounter angles

Further, the wind load coefficients in full scale were determined for different Reynolds numbers (according to wind speeds of the Beaufort wind scale). The result for head winds is shown in figure 4.38. The change of the pressure and shear force components over the Reynolds number exemplifies that wind loads are pressure dominant and the share of pressure increases slightly with the wind speed.

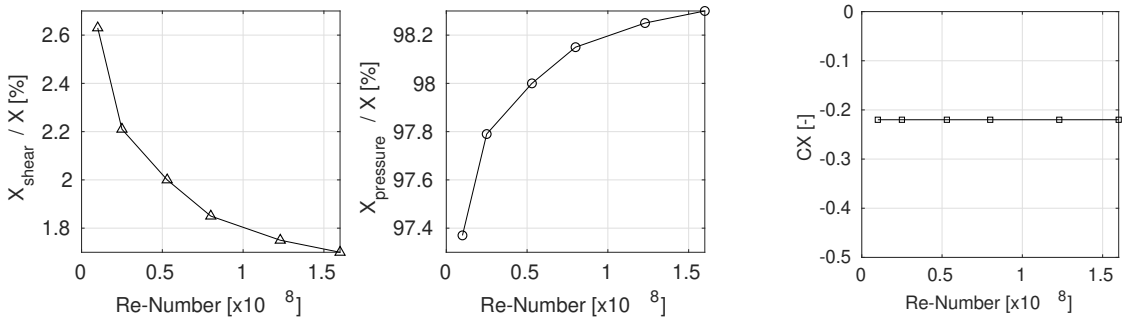

Figure 4.38: Reynolds effects in head winds and deviation of shear and pressure share of the total load

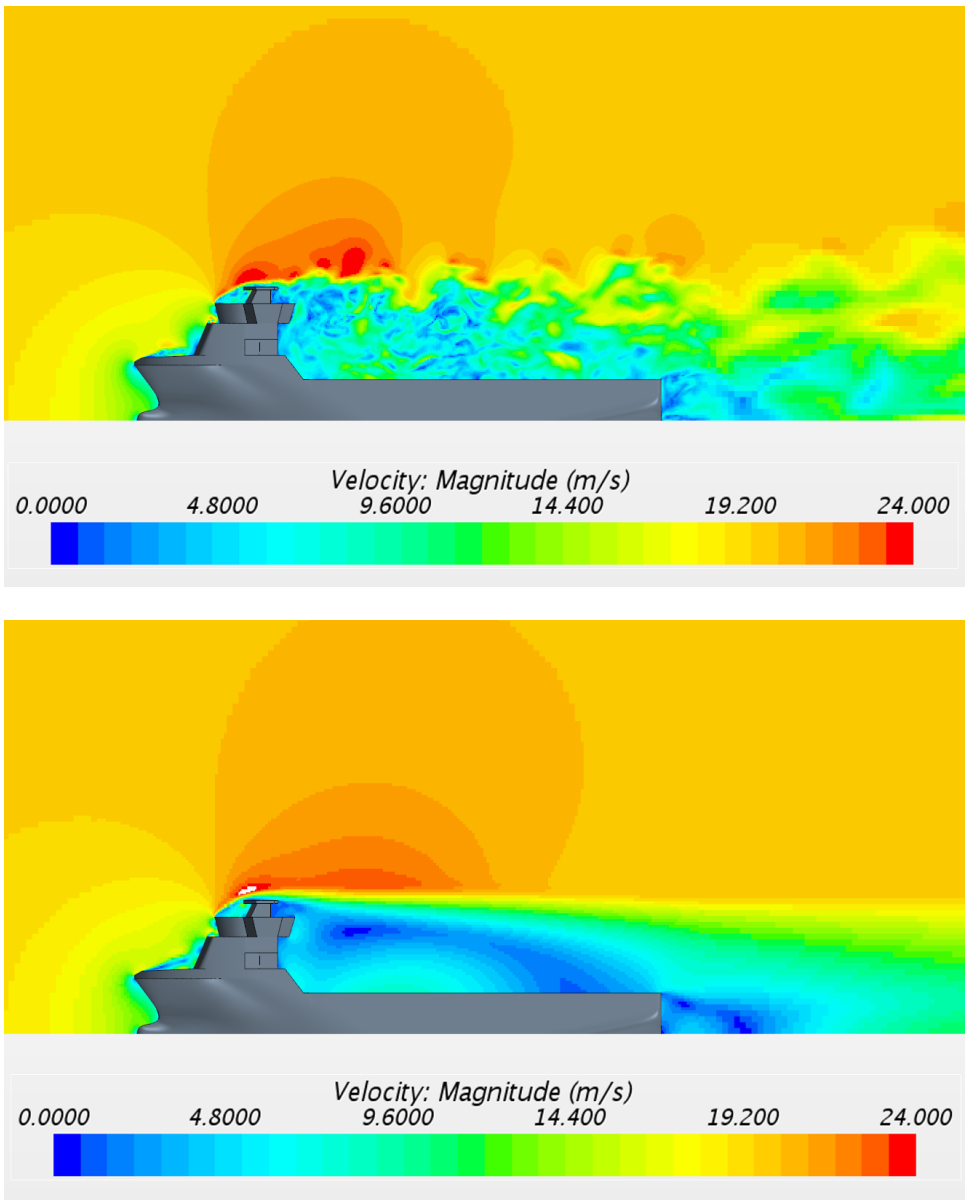

Figure 4.39: Comparison of the longitudinal velocity distribution in head winds between steady state RANS (bottom) and DES (top)

4.3.8 Influence of transient and turbulent flow

The approach in this work follows the steady state calculation of the wind loads. It is assumed, that the influence of turbulent flow and transient effects is not dominant, due to the high Reynolds number in the full-scale case. However, an approximation of the effects on the wind loads is elaborated in this section by a comparison between the steady state RANS simulation and DES.
The resultant longitudinal velocity distribution in head winds for both simulation methods is shown in figure 4.39. While the wind speeds in the wake of the deck house are averaged in case of the RANS solution, the turbulent effects of the wake flow are resolved by DES. A qualitative comparison with the smoke tests of section 4.2.2.2 allows the estimate of a more realistic representation of the air flow by DES. While the boundary between the accelerated flow above the vessel and the turbulent wake results almost close to the sharp boundary in the RANS solution, the velocities obtained from DES, demonstrate a mixture of high downstream velocities and vertical moving eddies.
For the DES simulation the grid resolution has been adapted on a hexahedral mesh type to 34.7 mio. cells with the smallest edge length of $\Delta x \approx 0.005m$. For the time discretisation a second order scheme was applied and the time step was set to $\Delta t = 5\text{e}{-5}$ sec.
The resultant longitudinal wind load coefficients in head wind is summarized in table 4.5. While the steady-state RANS approach underestimates the results of the experiments, the transient DES approach overestimates the result. However, the resultant deviation in the longitudinal force obtained from the DES approach are the smallest.

Table 4.5: Comparison between RANS and DES results for head winds

	RANS	DES	EFD
CX [-]	-0.223	-0.270	-0.258
Δ[%]	-13.6	+4.7	-

4.4 Comparison of wind load coefficients from CFD and experiments

A comparison of the numerically obtained wind load coefficients with the experimental results show a sufficient agreement. In figure 4.40 and 4.41 the the resultant coefficients and the absolute deviations are presented. For the OSV model the discrepancy yield to a mean of 9.3 % for CX, 7.7 % for CY, 6.5 % for CK and 14.9 % for CN. The transversal force and the yaw moment tend to be overestimated in contrast to the longitudinal force and roll moment, where an underestimation can be observed.

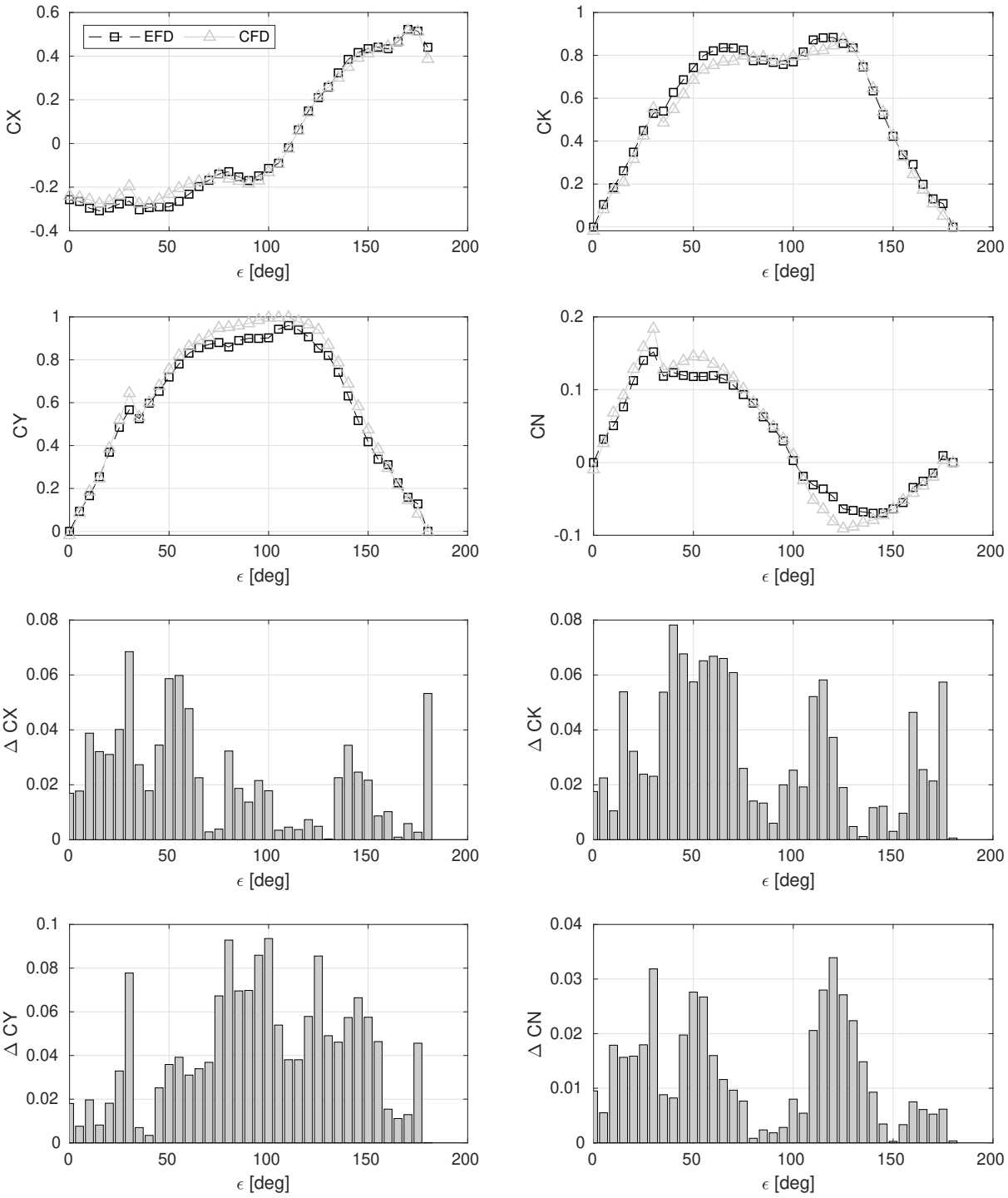

Figure 4.40: Comparison of wind load coefficients with experiments (OSV)

In case of the TUG model the discrepancy yield to a mean of 13.5 % for CX, 8.2 % for CY, 19.3 % for CK and 9.9 % for CN.

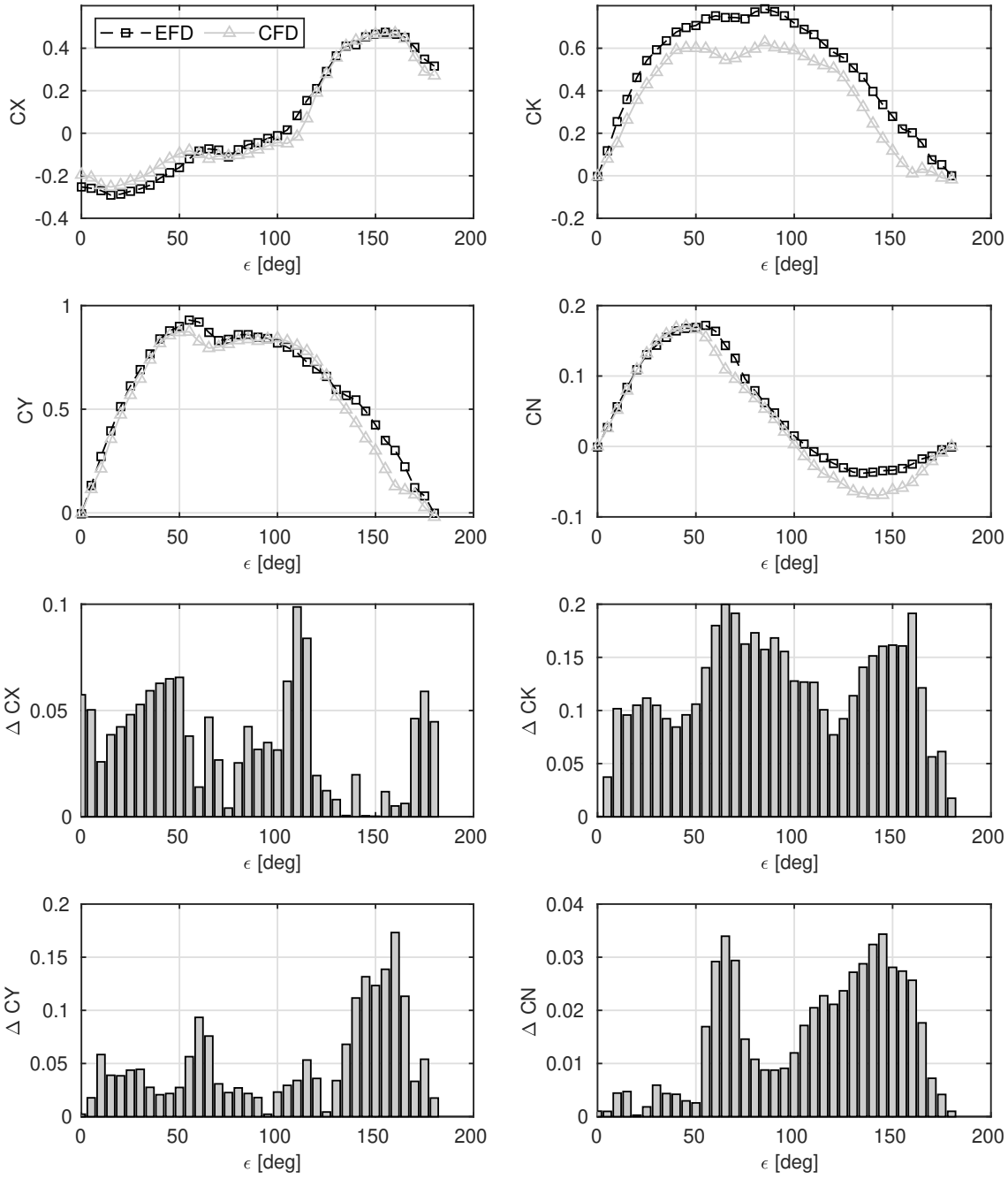

Figure 4.41: Comparison of wind load coefficients with experiments (TUG)

4.5 Discussion

The experiments and the simulation methods for determining wind loads result in differences based on the investigations presented. In order to be able to quantify the effects on DP simulations, computations were carried out with the *DPTool* using both sets of coefficients for the OSV model. The simulations were carried out for the OSV model. The ship was equipped with two VSP (each with 3800 kW) and three bow thruster (2x800 kW and 1x 600kW). Only wind loads were considered with a mean velocity of $v_w = 10m/s$ encountering from five directions. The allocation and the controller were set for a set point analysis. The results are presented in figure 4.42. For the simulation labeled EFD, the wind loads from the experiment have been used and correspondingly the CFD based ones in the other simulation.

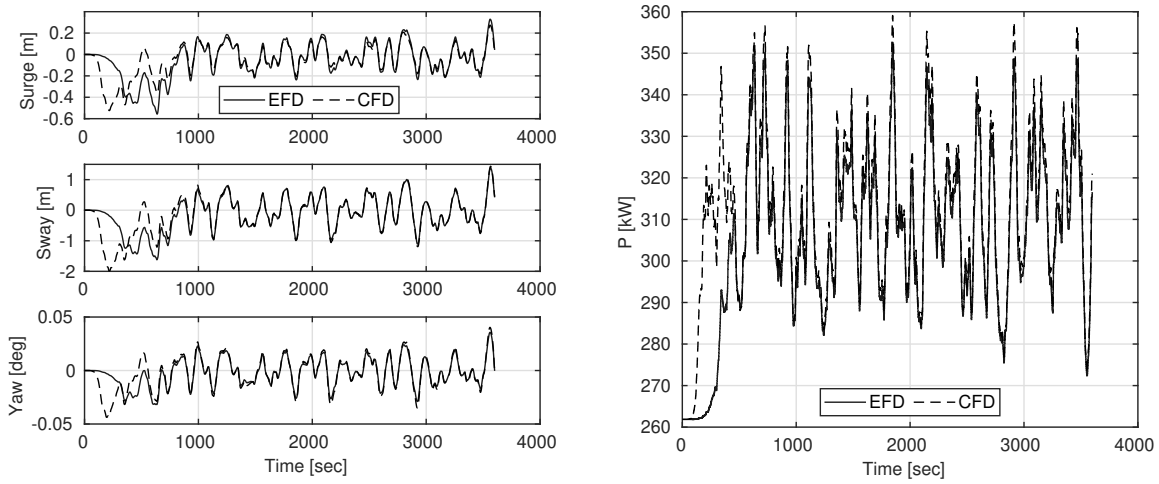

Figure 4.42: DP set point assessment for winds encountering from $\epsilon = 135deg$ - ship motion (left), required power (right)

Because the same wind speed fluctuation and wind direction has been applied to both sets, the controlled ship motion is very similar. Therefore, a fair comparison can be achieved by the observation of the required power. Hence, the effect of the wind load differences between the experiments and the CFD results is concluded by the ratio in power in table 4.6. A negative ratio corresponds to a higher power consumption with wind loads from CFD calculation.

Table 4.6: Required power during set point analysis

ϵ [deg]	EFD / CFD [%]
0	0.12
45	-3.36
90	-7.05
135	-5.02
180	-0.06

5 Current loads

Natural sea current is characterized by varying speed and flow direction combined with a certain turbulence level in the incident flow. Furthermore, unsteady flow develops around the hull due to body form and viscous effects.

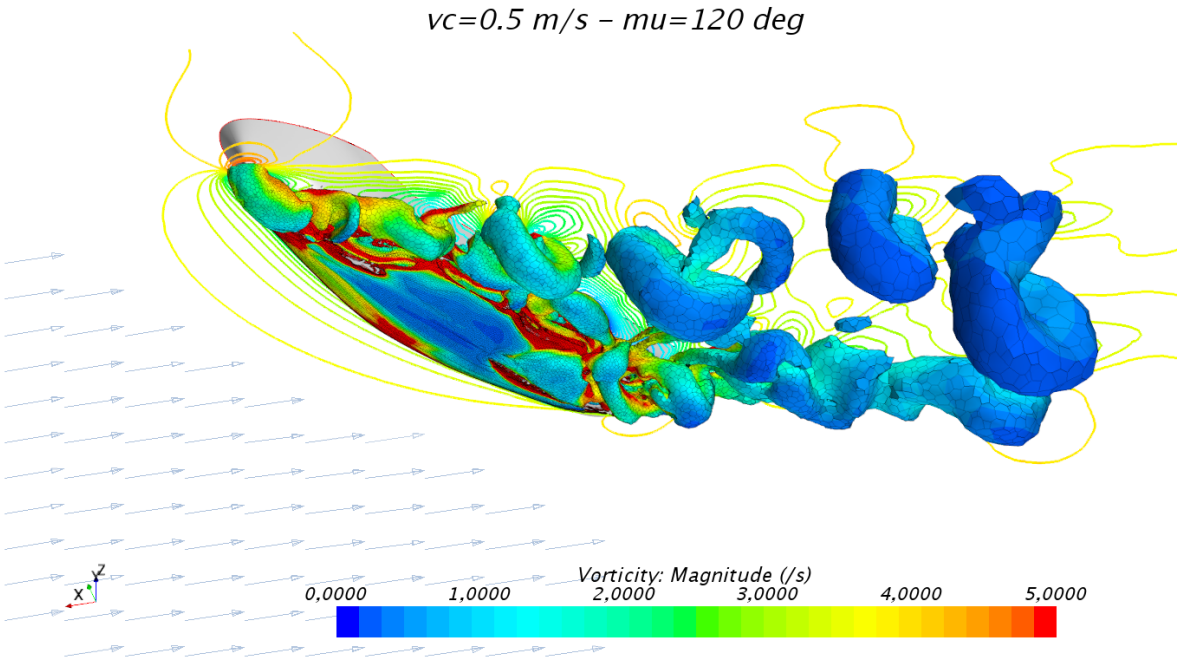

Figure 5.1: Turbulent flow around hull exposed in oblique current flow

The visualization of the turbulent flow around the OSV for quartering head current in figure 5.1 exemplifies the major unsteady effects:

Flow separation at the ship ends. Due to the interaction between accelerated flow caused by the displacement of the vessel and the decelerated flow in the ships wake field, the flow separates and a complex vortical flow structure is formed is formed. This effect involves instationary flow caused by the interaction of the flow regions and result in a fluctuating yaw moment.

Vortex shedding at bilge and keel as well as at ship ends. Depending on the encounter angle μ_c and the hull shape, instationary flow vorticies develop. Due to the interaction between the crossflow and the developed eddies, an instationary hull pressure distribution is developed on the leeward hull side.

Wake flow in downstream shaded areas at the leeward hull side. Heavy change in flow velocity and direction influence the force magnitude and direction. Especially, when the force component is small, i.e. longitudinal force in beam current, the influence of current loads in the considered direction is relatively high.

Free surface effects up- and downstream around the hull. Depending on the Froude Number, the hull displacement disturbs the pressure on the water free surface and the high current velocities develop a diverging wave system.

Turbulent flow on the hull surface. Depending on the roughness of the hull surface and the Reynolds number, transition of the flow occur.

The transient process outlined above lead to difficulties in predicting current loads in sufficient accuracy. For practical reasons, even though unsteady flow affects the ship motion, the model for current load prediction is limited to incident steady flow deterministic approach.
This chapter provides an experimental and a numerical assessment for the use of DP simulation of current loads for the OSV model that is used in this study. While the experiment provides integral forces, CFD simulation allows a detailed assessment of flow. In the following section a description of an experimental approach is presented. In addition CFD simulations are used to determine blockage and scale effects.

5.1 Implementation of current loads in the DPTool

For the consideration of current loads a module has been developed that accounts for the relative velocity and angle that sets in during DP operation. First, the encounter angle μ_e is calculated:

$$\mu_e = \psi + \alpha_0. \tag{5.1}$$

Here, the encounter angle is derived from the sum of heading angle ψ and the main flow direction of the current α_0. The resultant current velocity v_c

$$u_1 = u_c \cdot cos(\mu_e) - u \tag{5.2}$$

$$u_2 = -u_c \cdot -sin(\mu_e) + v \tag{5.3}$$

$$\mu_{c,rel} = atan\left(\frac{u_1}{u_2}\right) \tag{5.4}$$

$$u_{c,rel} = \sqrt{u_1^2 + u_2^2} \tag{5.5}$$

The influence of the roll and the pitch motion are neglected. The current coefficients are non-dimensionalised as follows:

$$C_{X,c} = \frac{X}{\frac{1}{2}\rho u_0^2 TB} \tag{5.6}$$

$$C_{Y,c} = \frac{Y}{\frac{1}{2}\rho u_0^2 TL_{PP}} \tag{5.7}$$

$$C_{N,c} = \frac{N}{\frac{1}{2}\rho u_0^2 TL_{PP}^2} \tag{5.8}$$

The current coefficients can be derived from experiments, CFD simulation or from an emperical approach.

5.2 Experimental approach

Experiments were carried out at the test facilities of the SVA-Potsdam, Germany [74]. The current loads were determined for the OSV bare hull model (model scale $\lambda = 16$) at low speed. The principle dimensions are listed in table 5.1. The measurements were carried out for 7 velocities from $v_c = 0.1m/s...0.7m/s$ ($v \approx 1.5kts...5.5kts$ in fullscale). The encounter angle has been varied from $\mu_c = 0°...180°$ by incremental steps of $\Delta\mu_c = 15°$. The objective of the model testing was to provide a consistent dataset of current loads to validate the CFD calculations.

Table 5.1: Principle dimensions of the OSV model

Loa	:	5.33	m
Lpp	:	4.84	m
Bwl	:	1.20	m
T	:	0.325	m
∇	:	1.200	m^3

5.2.1 Experimental setup and procedure

The model was mounted with a shaft on a six DOF load balance (compare fig. 5.2). The balance is equipped with six tension and pressure rods, one for the longitudinal force, two for the transversal force and yaw moment and three rods for the vertical force as well as for the roll and pitch moment. The forces and moments are measured in the tank fixed coordinate system, i.e. the positive longitudinal x-axis direction is parallel with the model in case of current from forward direction. The transversal axis point to port side and the vertical axis is directed upwards. Before the testing the model was trimmed even to keel at design draft with trim weights.

The measurements at the different speeds were carried out consecutively by incrementally increasing the velocity of the towing tank carriage. After the towing vehicle accelerates to the next higher speed, the measurement is started after a settling phase of $t_{settling} = 10sec$. The measuring time frame was set with $t_{measurement} = 15sec$.
The encountering angle has been set by rotating the shaft on the load balance. Between each run, a period of 15 minutes was allowed for the water movement in the towing tank to calm down.

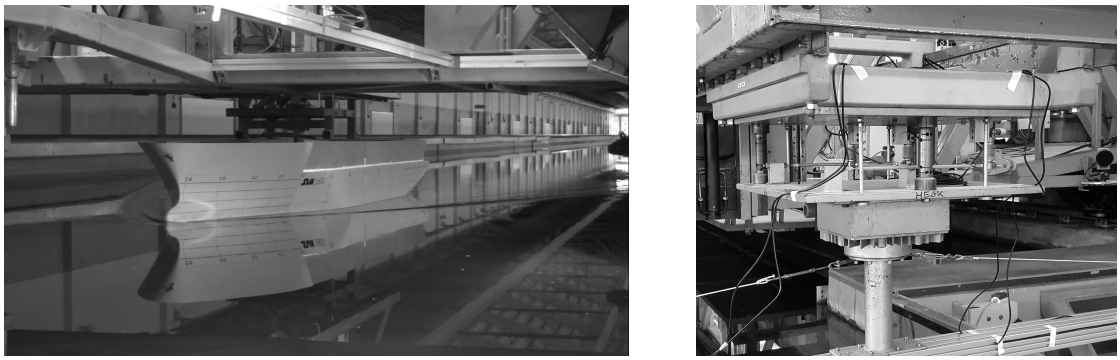

(a) (b)

Figure 5.2: OSV model mounted below the carriage(a), 6DOF load balance (b)

5.2.2 Modal analysis

The experimental determination of the current loads with the presented setup generally faces two challenges:

1. the transversal forces are of higher magnitude compared with the longitudinal force, hence the load balance must be accurate for small forces in longitudinal direction and at the same withstand high loads in transversal direction.

2. the shaft connection between the model and the load balance must be stiff enough in order to prevent motions of the vessel.

The first item has been addressed by the test facilities of the SVA-Potsdam, i.e. the setup and calibration of the load balance. For the latter issue, a modal analysis has been conducted to determine the eigenmodes of the experimental setup. The result is shown in figure 5.4. Here, the model has been excited with a small impulse in every degree of freedom. An estimate of possible vortex shedding frequencies by applying a Strouhal number of a cylinder $Sr = 0.21$ yield to

$$f_L = \frac{0.21 \cdot 0.1m/s \ ... \ 0.7m/s}{L} \approx 0.004Hz \ ... \ 0.028Hz \tag{5.9}$$

$$f_B = \frac{0.21 \cdot 0.1m/s \ ... \ 0.7m/s}{B} \approx 0.0175Hz \ ... \ 0.1225Hz \tag{5.10}$$

An excitation of the setup in eigenfrequency showed that this frequency will not influence the vortex shedding, since the 1st harmonic eigenmodes for all degrees of freedom are of higher order.

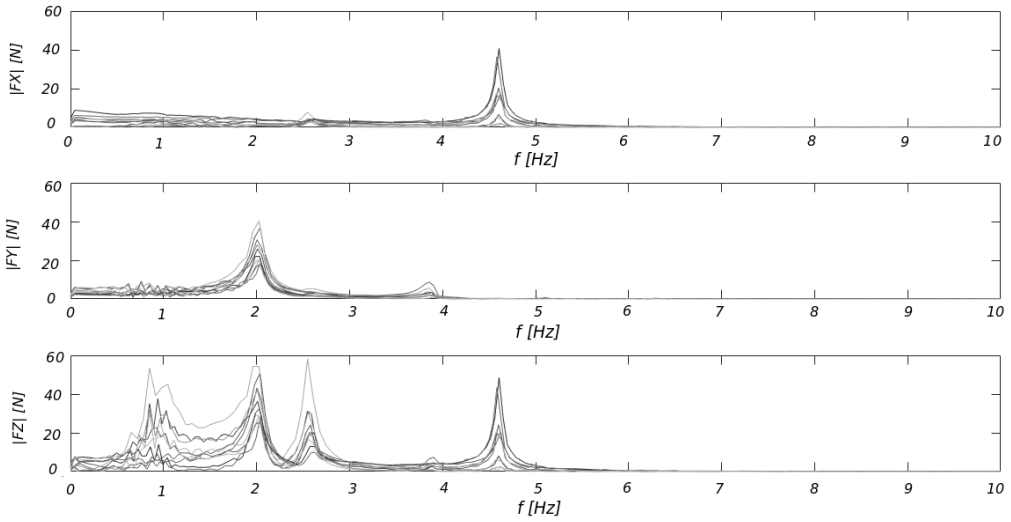

Figure 5.3: Fourier transform of a modal analysis of the experiment setup

Oscillating model motion in eigenfrequency can falsify the measured fluctuation of the forces. Therefore, the contributions of frequencies between 0.5 Hz and 6 Hz were filtered. In figure 5.4 the resultant Fourier transform and the measured forces of current loads for an encounter angle of $\mu_c = 75$ deg are illustrated.

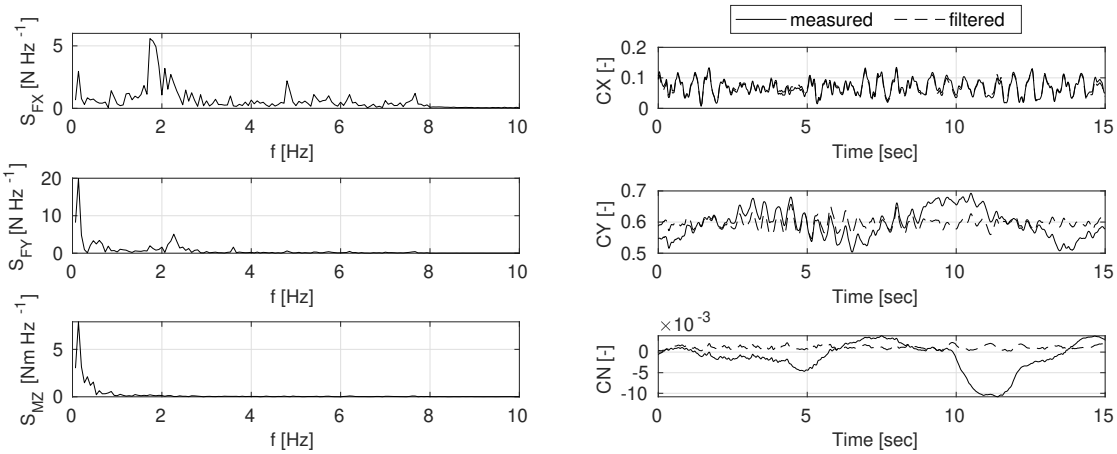

Figure 5.4: Measured forces in tank fixed coordinate system $(\mu_c = 75deg), v_c = 0.7m/s$

5.2.3 Results

The measured current forces in tank fixed coordinate system are summarized in figure 5.5. The encounter angle $\theta = 180deg$ correspond to incoming current from forward, $\theta = 90deg$ denotes

current from port side and $\theta = 0deg$ is current from astern.

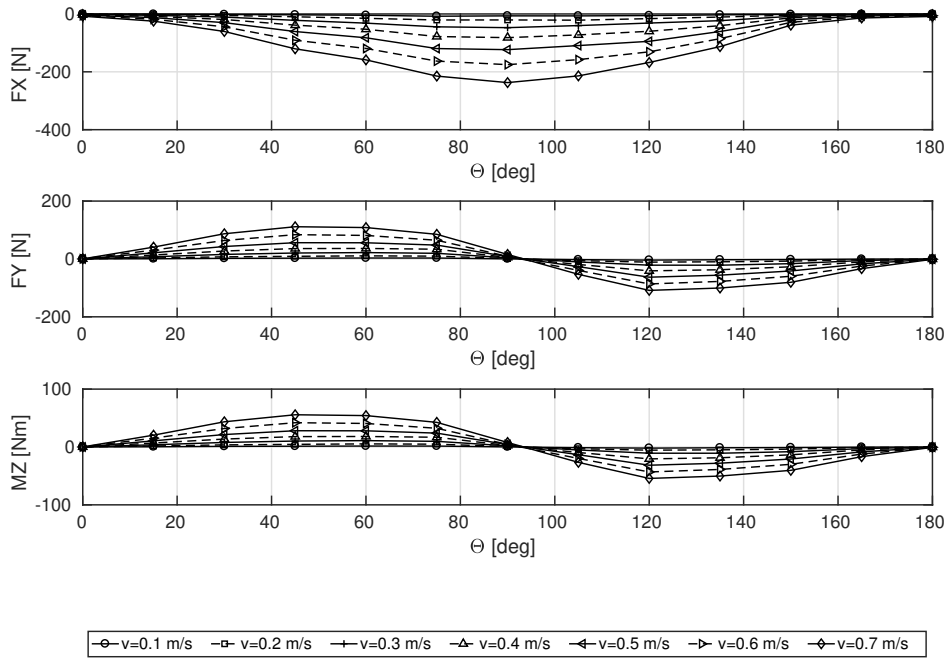

Figure 5.5: Current loads in tank reference system

The conversion of the measured forces into ship-fixed coefficients is shown in Figure 5.6. The longitudinal forces here are about one order of magnitude lower than the transverse forces. Strong fluctuations in the longitudinal force are obtained for an encounter angle of $\mu_c = 90deg$. This illustrates the difficulty of measuring small forces with a high degree of accuracy while at the same time applying a large transverse force. Further dynamic effects, such as detaching vortices may be involved here. For velocities above 1.5 kts the coefficients approach a constant value.

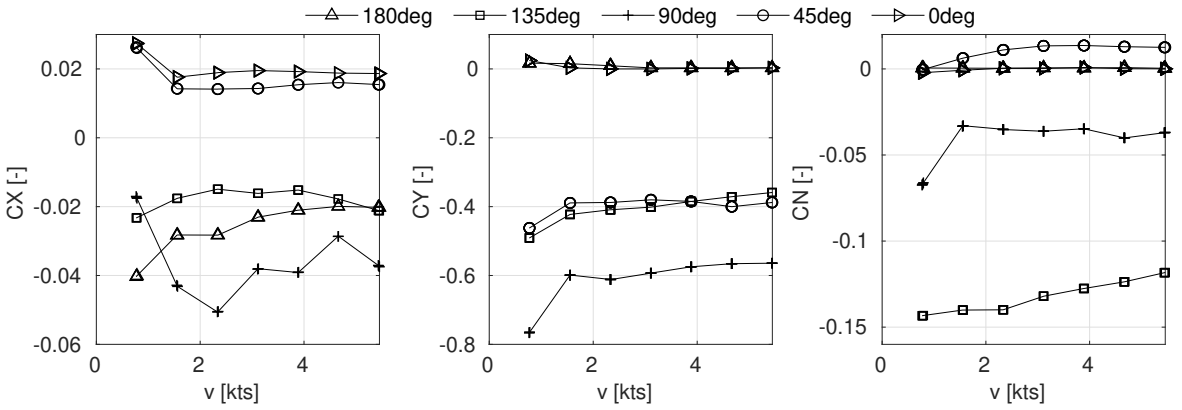

Figure 5.6: Velocity dependency of current load coefficients

5.3 Numerical approach

An accurate computation of the flow forces requires the consideration of the relevant turbulent effects in the simulation. These depend, among other things, on the geometric properties of the ship's form. The objective hull (OSV model) is characterized by a large bilge radius (compared to the draft of the hull), a small skeg with sharp edges and a high deadrise on the aft bottom with a sharp centerline. Additionally, the waterline at the aft body is tempered and the bulbous bow is not fully submerged. In figure 5.7 the vorticity of the current flow in sections around the OSV model with an encounter angle of 90 deg is shown. The intensity of the turbulent effects as well as the vortex formation is strongly dependent on the flow velocity and the encounter angle. The influence of flow separation and the vortices are accounted as dominant for the current flow coefficients, while the waves are according to the low Froude numbers negligibly small. However, with increasing current speed small deformation of the waterline along the hull might occur in section of the skeg and at the ship ends.

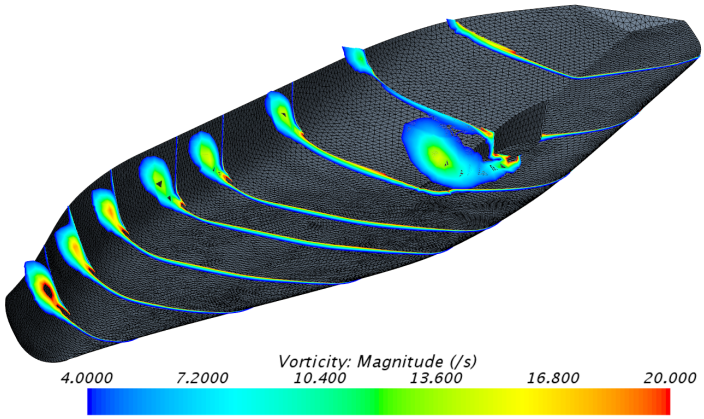

Figure 5.7: Vortex development on the hull in current flow - $\mu_c = 90$ deg, $v_c = 0.5$ m/s

5.3.1 Numerical setup

For the simulation of current loads three solution methods were applied and compared with each other: steady-state RANS, transient RANS and DES. However, due to the lower numerical effort, the steady-state method will be used to determine the flow coefficients for further DP simulations. The transient methods were applied in order to study unsteady flow effects. A second-order upwind scheme was used for the spatial discretisation. When transient methods are applied, the time has been discretised using a second order scheme. Prior the simulation of all encounter angles, the common turbulence models $k-\epsilon$ and $k-\omega$-SST with and without wall function were compared. It was found that the $k-\omega$-SST with no wall function (low-Re) delivered more accurate results. Considering the fact that a highly three-dimensional unsteady

separated flow around a blunt body is expected (far from a 2D steady friction-driven flat plate flow) it is justified and near-wall modeling errors being then avoided.
Although the velocities and the density differ from the assessment of the wind loads of the previous chapter, the flow characteristics a high degree of is similarity. Therefore, a polyhedral mesh was applied without proving the benefits again. However a grid study has been conducted for currents encountering from $\mu_c = 75deg$ (see figure 5.8). According to the results of the study, the grid of the third refinement level with a total of 1.6 mio. cells was selected. For the resolution of the velocities near the ship hull a prism layer with 15 cells and a stretching factor of 1.25 was applied.

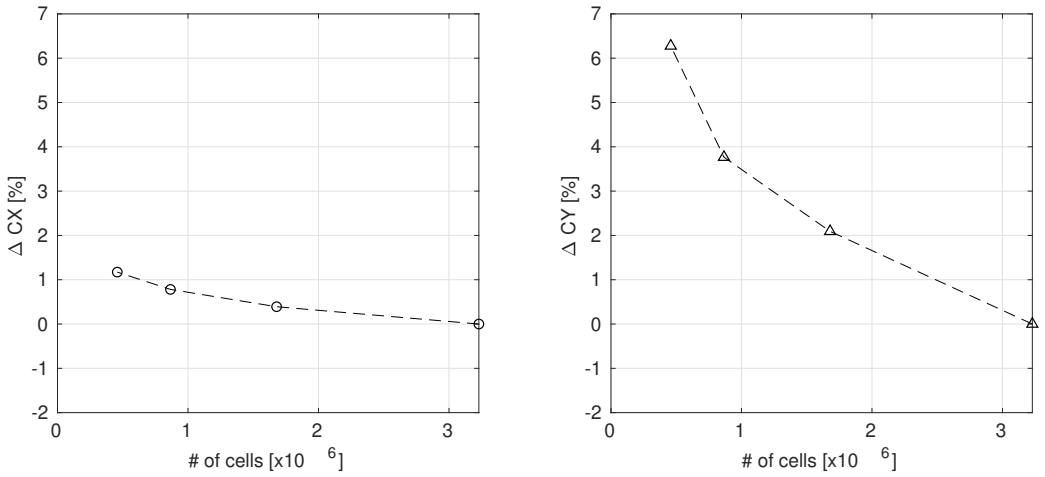

Figure 5.8: Grid study of current loads

The computational domain was chosen to be cylindrical. The diameter of the cylindrical disc measures about ten ship length, the height was set to one ship length. At the domain bottom the hydrostatic pressure is prescribed. Since the free surface effects are accounted to be small, a symmetry boundary condition is set at the top. The speed is prescribed on the lateral surface of the cylinder. A sketch of the domain setup is given in figure 5.9.

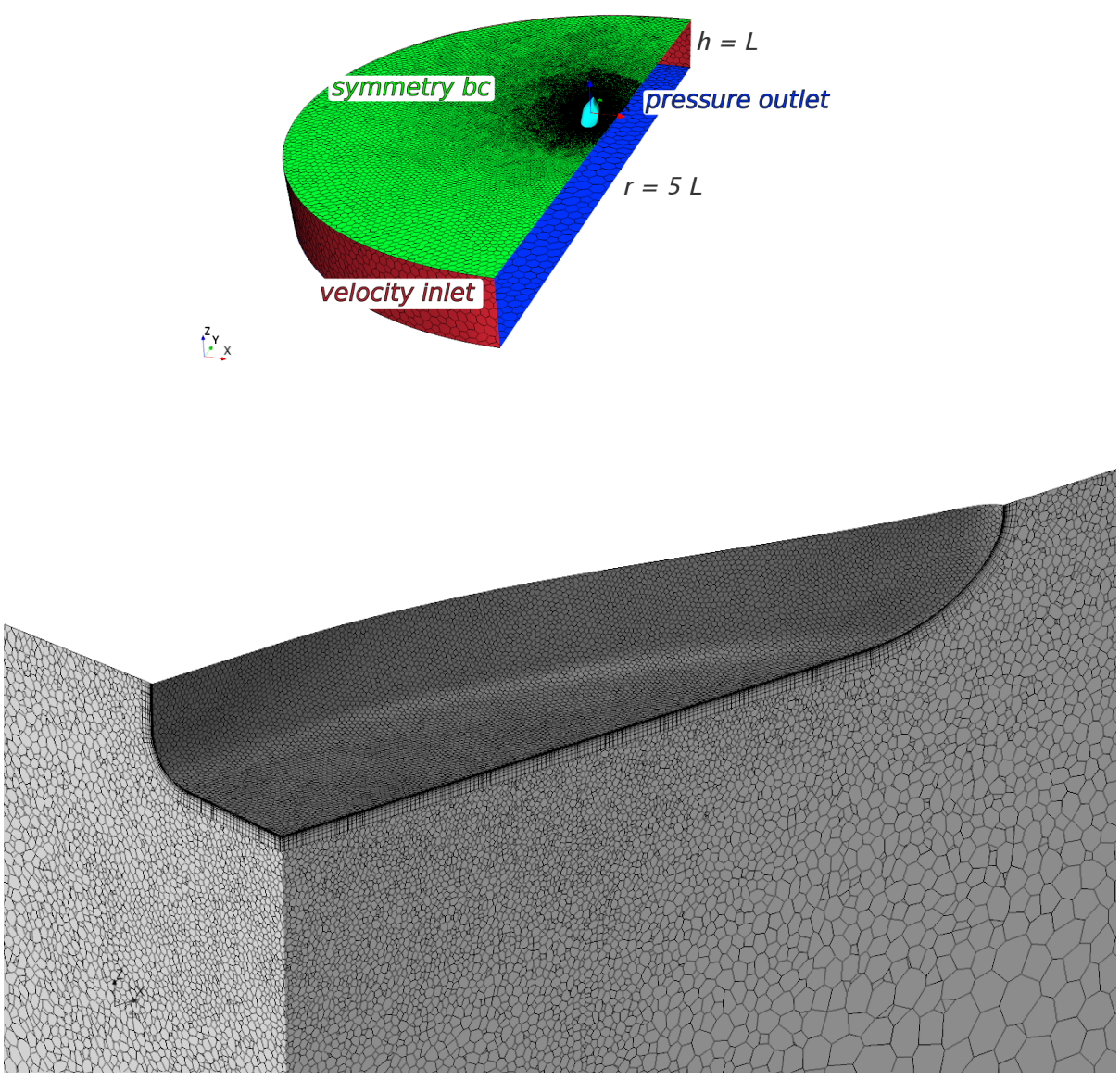

Figure 5.9: Domain setup for current loads (top), mesh refinement and prism layers (bottom)

5.3.2 Turbulent effects in the flow around ships

In general for the consideration of turbulent flow in numerical simulations a time depended method has to be applied. However, determining the current coefficients requires a large number of simulations with a sufficient simulation time and therefore results in an enormous computational effort. Knowing that the current numerical steady-state approach of this work neglects unsteady flow effects, such as turbulence, it is nevertheless an efficient approach in the sense of accuracy and numerical effort. In order to determine the influence of such effects, the steady-state results have been compared with the flow solution of a transient RANS simulation and further a DES approach.
The visualization of the inherent vortical structures in the three-dimensional flow field in a two-dimensional figure is a challenge. A commonly used method for vortex visualization is that of the Q-criterion. Positive values of Q are indicative of areas where the vorticity dominates and negative Q values indicate areas where viscous stress dominate.
In figure 5.10 the vorticity is visualized as an isosurface of Q=0.01. This value resulted in a sufficient representation ranging from very limited vortical structures ($Q \geq 0.1$) to an excessive number of vortices (($Q \leq 0.001$).
In order to compare the methods with each other the simulations were processed until the same level of convergence has been reached. The results for the steady-state method are aligned on the left side, the transient RANS approach can be find in the middle and on the right side the solution of the DES flow field is shown. Almost similar vortex structures are obtained for current flow from front and aft and for small incoming flow angles. With increasing encounter angle vortex structures detaches from the ship hull and follow the flow direction. Three-dimensional flow effects, such as the interaction between vortex structures transversal to the current flow, increase with the approach to current flow from the beam side.
A comparison of the transverse forces shows that the forces raise with increasing turbulent flow separation. The ratios of the DES and the steady-state RANS solution is summarized in table 5.2. The maximum deviation is obtained for encountering current of $\mu_c = 120deg$, where unsteady effects dominate.

Table 5.2: Comparison of transversal current coefficients CY

	15	45	90	120	135	165
Δ DES/RANS [%]	6.1	6.1	12.9	33.5	4.5	4.1

The velocities and the pressure distribution on the hull are shown in the figures 5.11 and 5.12 for the steady-state and the DES approach. A comparison of the upstream pressure shows a similar distribution. Downstream of the hull, when the turbulent flow develops, the velocities and thus the pressure distribution are very different. The averaging of the velocities in the stationary RANS simulation leads to an overestimation of the size of the wake field and thus to an overestimation of the pressure.

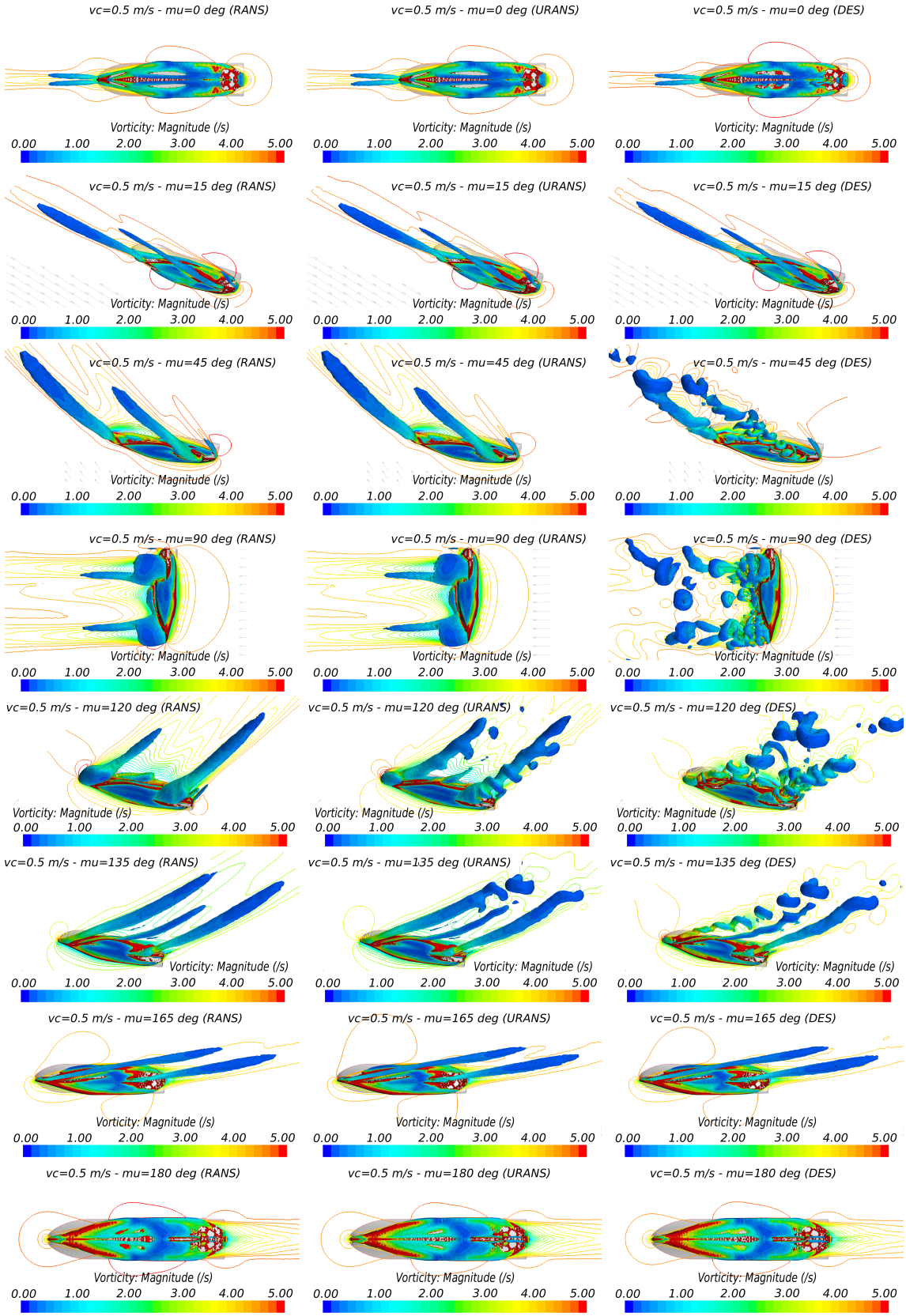

Figure 5.10: Visualization of vortical structures in current flow

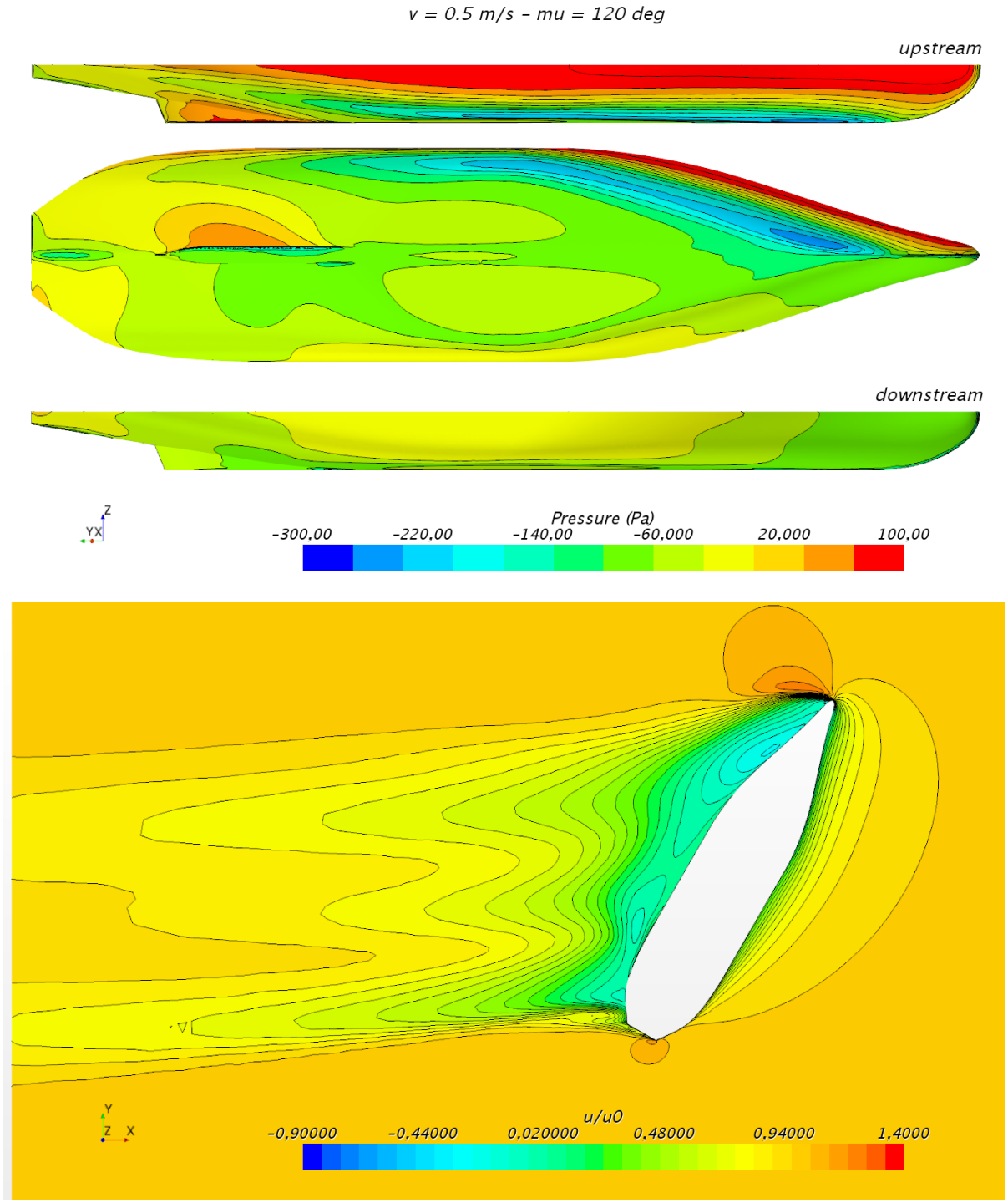

Figure 5.11: Pressure distribution RANS simulation (top), velocity in symmetry plane (bottom)

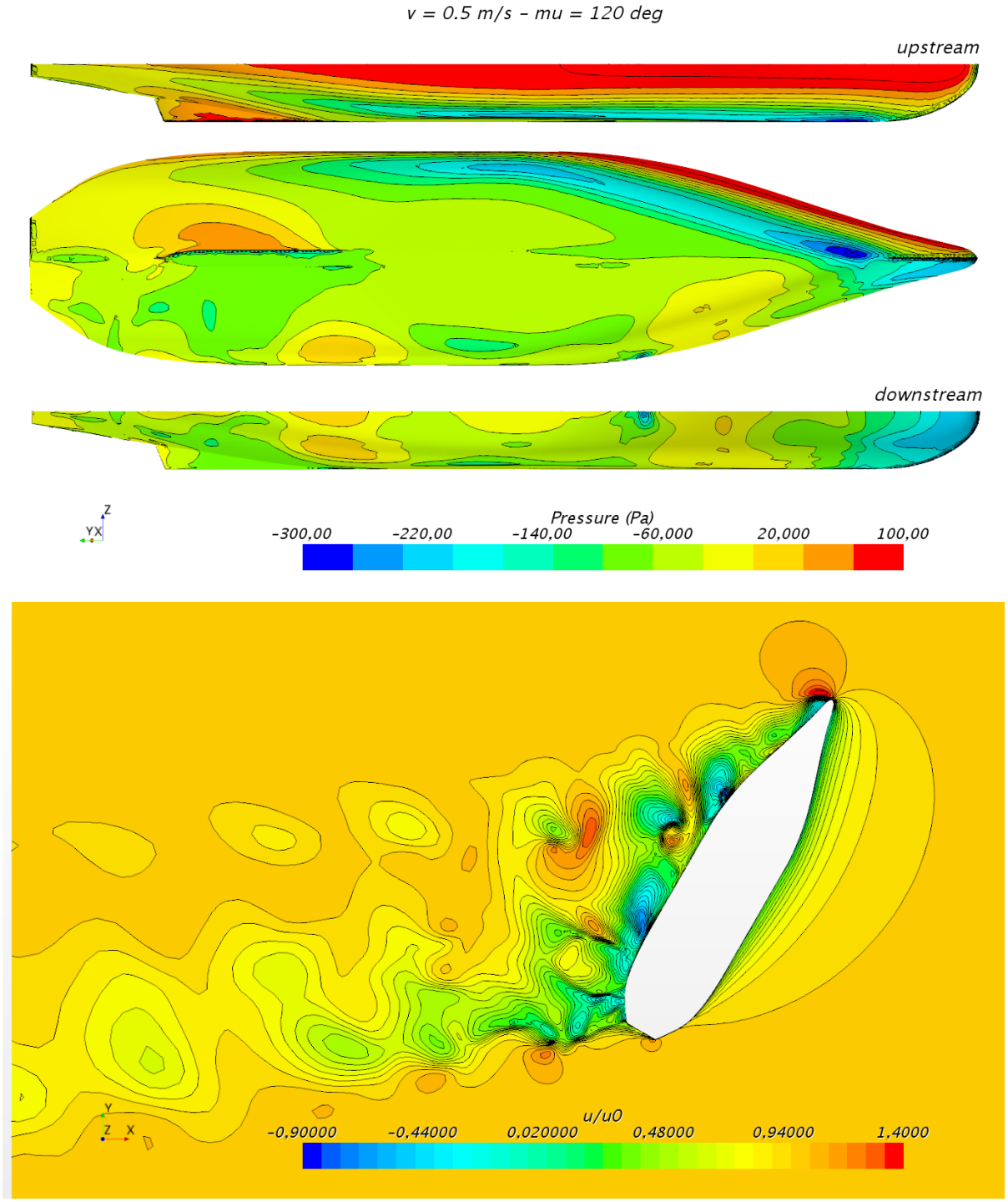

Figure 5.12: Pressure distribution DES simulation (top), velocity in symmetry plane (bottom)

5.3.3 Influence of the tank walls

When the model is set transversely to the tank direction it has a blockage ratio of 3.85 %. Therefore, the impact on the force measurements is expected to be negligible. However, the length of the model is about 60 % of the tank width. Therefore, an additional simulation was conducted with the exact tank width. The result is compared with the previous introduced numerical setup. The longitudinal force (tank fixed coordinate system) is increased by ≈ 3.2 % and the transversal force is increased by about 1.8 %.

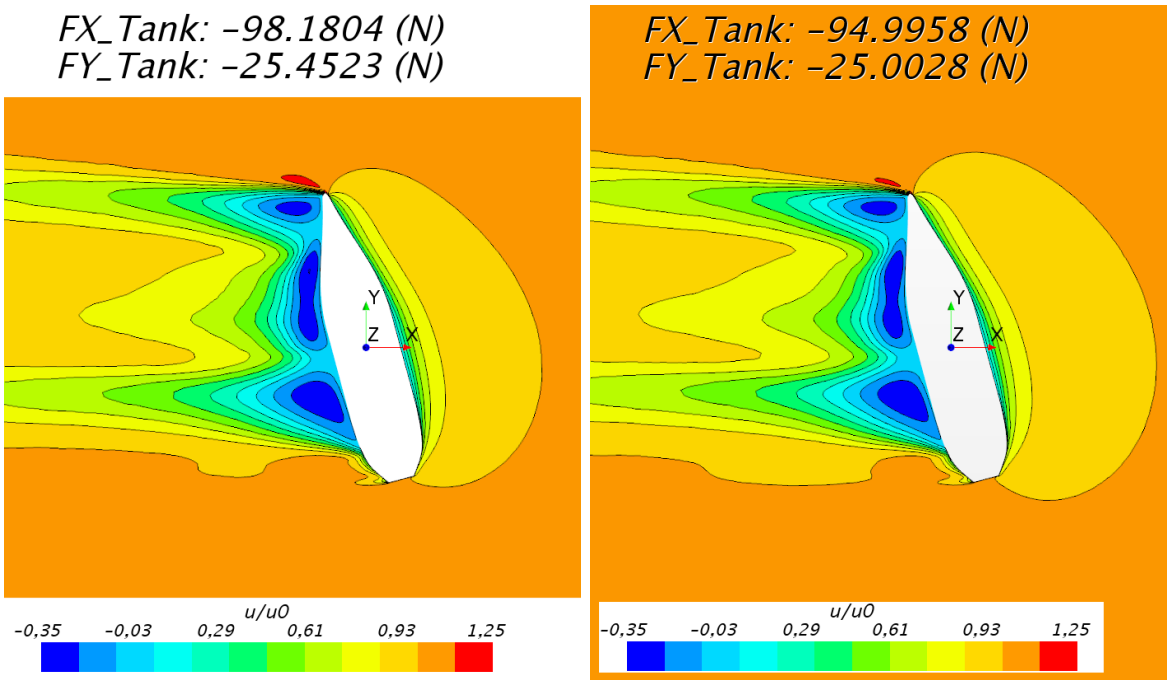

Figure 5.13: Normalized velocity with tank walls (left) - without tank walls (right)

5.3.4 Influence of free surface

As the tested velocities correspond to Froude numbers in range of $Fn \approx 0.014 \ldots 0.097$, no relevant bow waves were visible during the experiments.
In order to quantify the magnitude of small disturbances of the free water surface, a simulation with consideration of a free water surface was carried out for comparison. The resolution of the surface elevation strongly depend on the number of cells that are provided in vertical direction and the ratios in horizontal plane. The grid was created with 10 cells per wave height.
The surface elevation of the simulation is represented in figure 5.14. Compared to the draft of the model the free surface elevates up to ≈ 3%. The effect on the current loads can be expressed by the comparison of the transversal loads. The force increases with ≈ 3.3%.

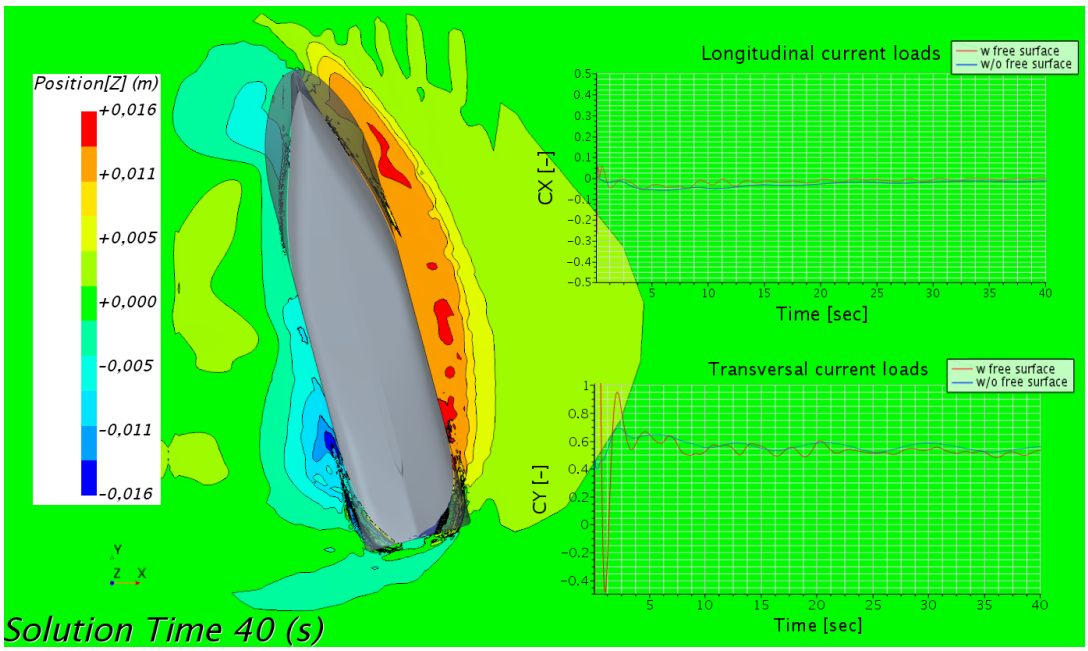

Figure 5.14: Visualization of the free surface with current flow ($\mu_c = 75deg$, $v_c = 0.7m/s$)

5.4 Comparison of current load coefficients from CFD and experiments

A comparison between the three numerical approaches and the experimental results is summarized in figure 5.15. The coefficients are represented in the ship fixed coordinate system and were transferred into the mid ship reference point ($L_{PP}/2$). The sign of the longitudinal component changes several times. This is due to the previously mentioned difficulties in experimental studies of measuring small longitudinal forces accurately with comparable large transversal forces. Thus, compared to the forces acting in each direction, the largest discrepancy between the numerical methods and the experiments is found in the longitudinal direction. However, the discrepancies are of small magnitude.

If transient and turbulent effects of the current loads become larger, e.g. for beam encountering direction, the deviations in the results obtained by DES method become smaller and good agreement is obtained for the transversal loads.

The current loads of the yaw moment are typical for offshore supply vessels. This effect may be caused by the small section immersion in the aft body compared to the draft at the forward part of the vessel. Thus, the yaw moment for currents from forward direction yield to a higher moment, while currents from the aft have minor influence.

The bar chart at the bottom of the figure 5.15 shows the absolute differences between the applied numerical methods and the experiment. The absolute mean percentages of all encounter angles are summarized in table 5.3. Due to the uncertainty of the experiment and CFD for the small longitudinal forces the deviations become large. The lowest deviations can be achieved with the DES method. In case of the transversal load the differences among the numerical approaches are significant with more than 10 % improvement.

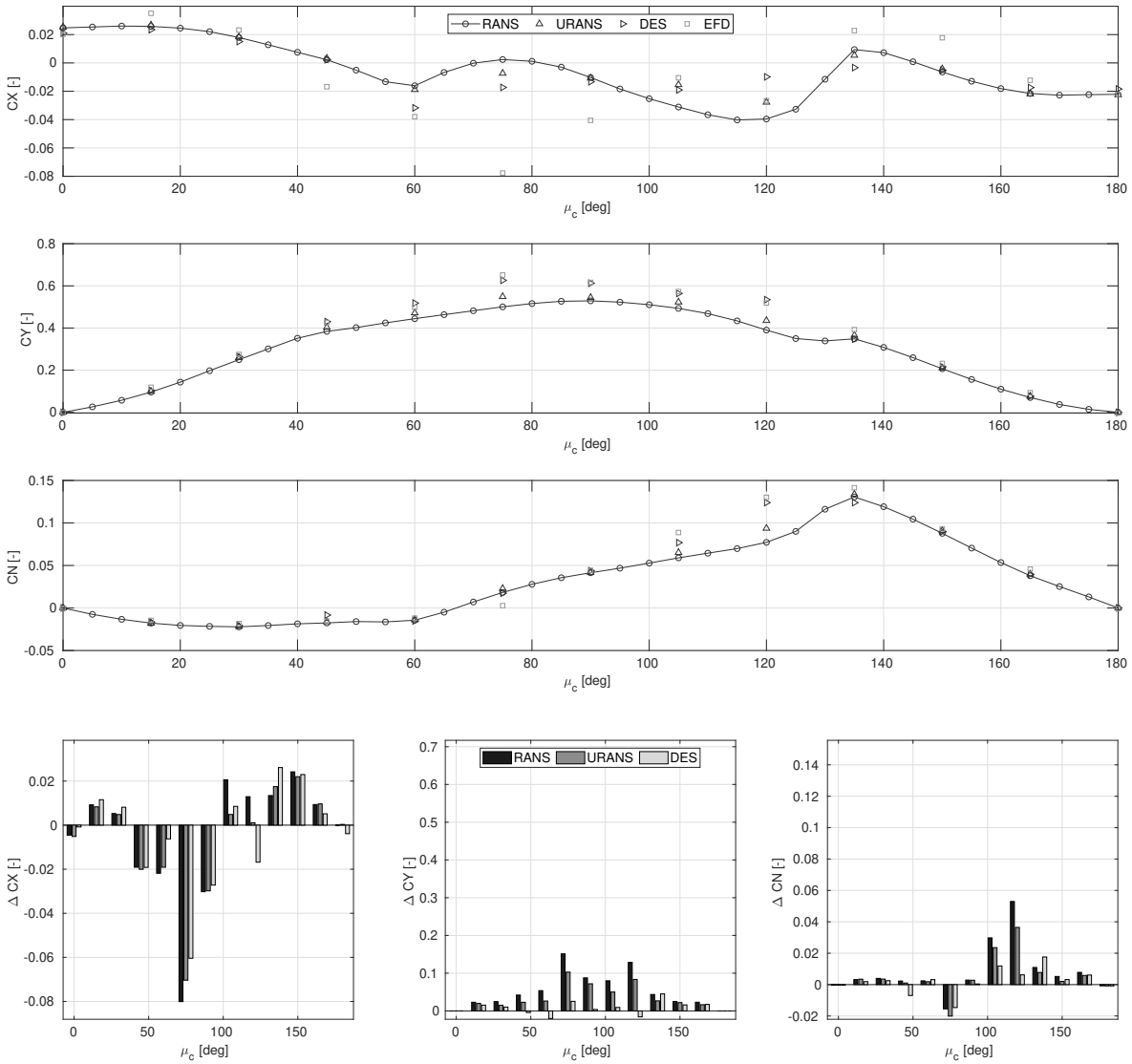

Figure 5.15: Results of numerical methods and experiments in ship fixed coordinate system

Table 5.3: Mean percentage deviations from the experiment

	Δ CX [%]	Δ CY [%]	Δ CN [%]
DES	27.3	6.3	20.6
URANS	28.9	11.4	22.2
RANS	50.4	17.5	25.9

5.5 Discussion

The results of a set point simulation are presented in figure 5.16. Only constant current forces were used encountering from $\epsilon = 135deg$. In order to quantify the effects of the deviation of elaborated coefficients from experiments and coefficients obtained from CFD simulation the resultant motion and the required power are compared against each other. The motion of the ship has a small deviation in the initial phase, while the control brings the ship's position close to the target position. However, the power required for dynamic positioning results in higher consumption with the set of coefficients determined from the experiments.

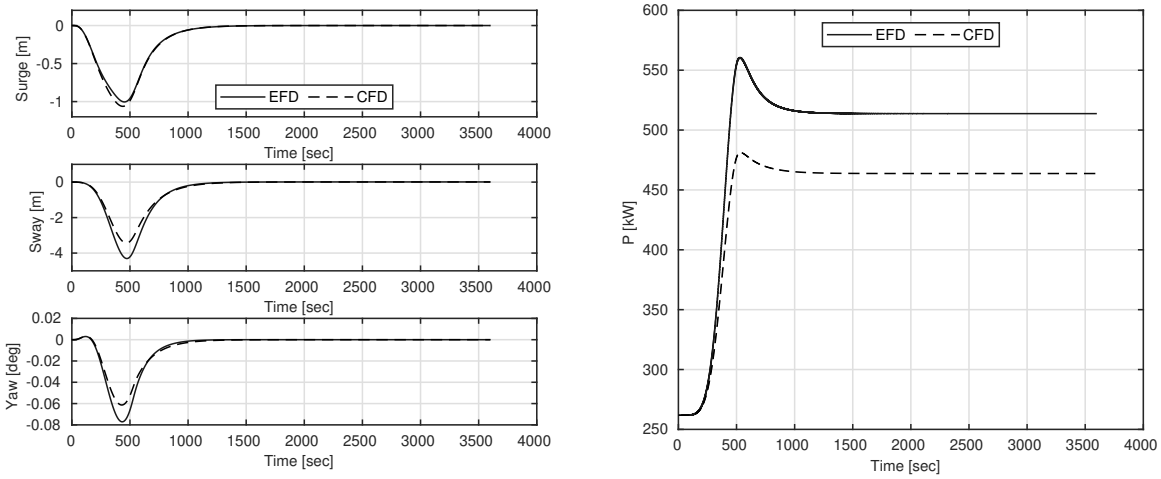

Figure 5.16: DP set point assessment for currents encountering from $\epsilon = 135deg$ - ship motion (left), required power (right)

The deviation between the two simulations for varying encounter angles is summarized in table 5.4. The greatest deviations can be found for flows directed from the side and obliquely from the front. No effects can be determined for the other encountering directions.

Table 5.4: Required power during set point analysis

ϵ [deg]	EFD / CFD [%]
0	-0.67
45	-0.29
90	11.87
135	10.60
180	0.02

6 Wave loads

The consideration of wave forces represents the most crucial component of all three environmental forces. For the implementation of wave loads, most decisive is a consistent distribution of the 2nd order wave loads over the encountering angle and the wave components. This is because in contrast to 2nd order wave loads, the wave forces of 1st order exert oscillating ship motions with no drift motion in horizontal plane.
The wave loads may be obtained from experiments or numerically. The difficulty in measuring 2nd order wave loads lies in the challenge of monitoring forces on a model that is free in all six degrees of freedom. On the other hand, numerical simulation with a high accuracy include a high computational effort. Therefore, in most cases methods of first order in frequency domain are applied. The following three components represent the largest shares in the composition of the wave drift forces:

1. Forces related to the non-linearities in the free surface

2. Forces of the velocity squared term in the Bernoulli's equation

3. Forces due to the nonlinear change of the vessel geometry caused by relative vertical or rotational motion

In the following section an experimental procedure for measuring 2nd order wave loads is presented. Further three numerical methods for the computation of the wave loads in frequency domain and time domain are described, i.e. a linear strip method, a three-dimensional panel method and a transient viscous field method. Finally, the results of the motion and the wave loads of the three methods are compared.

6.1 Implementation of wave loads in the DPTool

In the *DPTool* the second order wave drift forces are accounted as time depended varying forces. Therefore, prior the DP simulation, the wave forces are computed by superpositioning the wave loads obtained from frequency domain and the components of the seaway. Then, the same seaway and wave forces are used in the simulation.
With the assumption, that the drift forces and yaw moment are varying with the square of the seaway envelope $a^2(t)$, the drift forces in time domain can be derived by using a statistical

description of a natural seaway. For an envelop of a random seaway with a fluctuating wave amplitude $\zeta(t)$ follows:

$$a^2(t) = \zeta^2(t) + \frac{(d\zeta/dt)^2}{\omega_0^2} \tag{6.1}$$

with the significant frequency of the seaway ω_0. The wave elevation and the corresponding envelope of a random seaway with a peak period of $T_P = 12.7sec$ and a significant wave height $H_{1/3} = 2.5m$ is illustrated in figure 6.1.

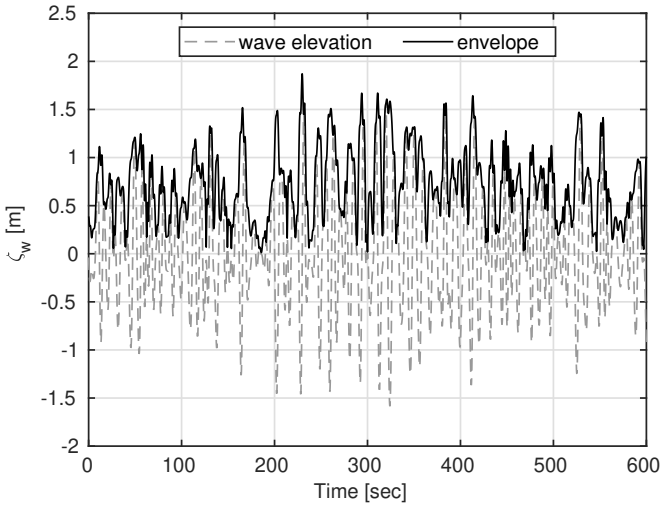

Figure 6.1: Wave elevation and wave envelope of a Pierson Moskowitz Seaway with 12.7 sec and 2.5 m

According to Clauss et al. [16] the forces and moment in time-domain are then derived by:

$$F^{(2)}(t) = \frac{1}{2}\rho g L\ \alpha_0^2\ a^2(t). \tag{6.2}$$

$$M^{(2)}(t) = \frac{1}{2}\rho g L^2\ \alpha_0^2\ a^2(t). \tag{6.3}$$

$F^2(t)$ and $M^2(t)$ represent the second order wave loads, L is the representative ship length while α_0^2 introduces the mean drift force coefficient as weighted average to the given seaway spectrum distribution $S_{zz}(\omega)$:

$$\alpha_0^2 = \frac{\int_0^\infty \alpha^2(\omega) \cdot S_{zz}(\omega) d\omega}{\int_0^\infty S_{zz}(\omega) d\omega} \tag{6.4}$$

with $\alpha(\omega)$ as the non-dimensional drift force component for the respective frequency ω:

$$\alpha_{FX,Y}^2(\omega) = \frac{\overline{F}_{X,Y}^2(\omega)}{\frac{\rho}{2} \cdot g \cdot L \cdot \zeta_a^2}. \tag{6.5}$$

$$\alpha_{MZ}^2(\omega) = \frac{\overline{M}_Z^2(\omega)}{\frac{\rho}{2} \cdot g \cdot L^2 \cdot \zeta_a^2}. \tag{6.6}$$

Herein, $\overline{F}_{X,Y}$ and $\overline{M}_Z$ are the frequency dependent average drift forces. The resultant wave drift forces in quartering head seas of the previously introduced seaway for the OSV in fullscale is represented in figure 6.2. The average drift forces are obtained by the three dimensional panel method ANSYS AQWA.

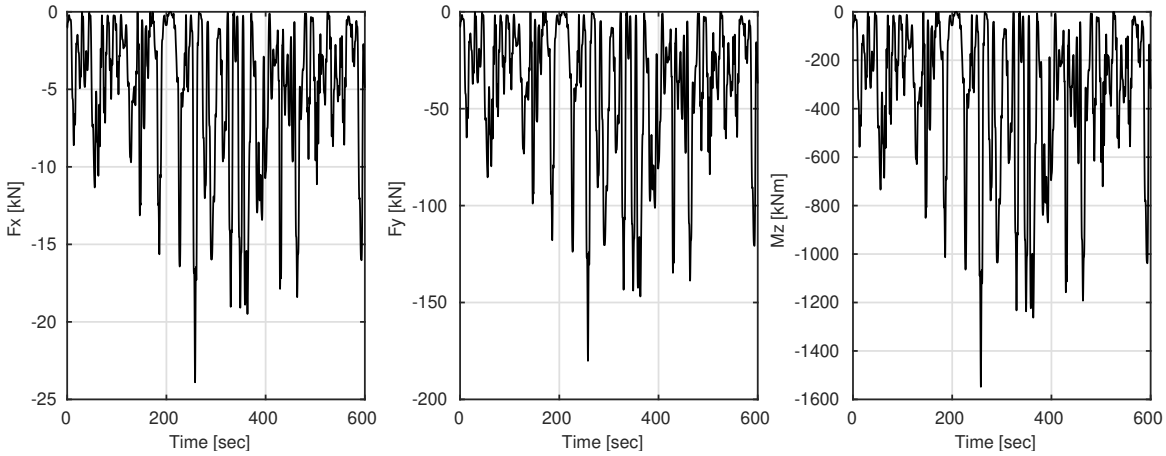

Figure 6.2: Drift forces in time domain for μ=135 deg

6.2 Experimental approach

Experiments with the OSV model were conducted in the test facilities of the SVA-Potsdam [74]. During the test series single harmonic waves were considered with varying wave lengths and wave steepness.

6.2.1 Experimental setup

The model was attached to a cross frame with four linear springs to keep it in place while the incoming waves exert ship motions. This setup allows nearly unrestricted 1st order oscillatory ship motions, while an offset of the mean position occurs. Both, the forces in the springs and the motion is measured. Additionally the cross frame is attached to a load balance for alternative measurement of the forces.
The spring stiffness was set to $c = 80\frac{N}{m}$. The value of the constant results from the assumption that the restoring force of the entire setup is less than 1/6th of the first-order wave force. This approach prevents oscillatory components that may effect the desired 2nd order wave forces.
The incoming waves were measured by two sequentially positioned wave probes with about two and three model lengths in front of the model. Due to energy dissipation of the generated waves in the tank basin, a slight deviation of the wave steepness along the propagating direction was observed. Although the wave probes were located far enough ahead of the model, radiated waves of the models motion influenced the encountering wave height measured. Therefore, the

incident wave without the model present has been measured according to the test procedure. The resulting wave amplitudes are summarized in table 6.1. The measured forces and motions

Table 6.1: Calibration of the undisturbed waves in the wave tank

$Hw[m]$	$\lambda[m]$	$\omega[rad/s]$	$T[s]$	$\zeta_{wp1}[m]$	$\zeta_{wp2}[m]$
0.160	5.30	3.410	1.842	0.138	0.132
0.210	5.30	3.410	1.842	0.182	0.172
0.095	3.18	4.403	1.427	0.099	0.091
0.127	3.18	4.403	1.427	0.129	0.123
0.159	3.18	4.403	1.427	0.161	0.156
0.064	3.18	4.403	1.427	0.069	0.063
0.191	6.36	3.113	2.018	0.135	0.133
0.223	7.42	2.882	2.180	0.215	0.207
0.191	7.42	2.882	2.180	0.187	0.179

were normalized with the corresponding measured wave amplitudes of the undisturbed wave. The setup of the experiments is sketched in figure 6.3. At the models stern, a small rod was attached in order to prevent contact of the model with the ropes. The attached ropes were all set with the same length and the springs were initialized with the same pre-tension.

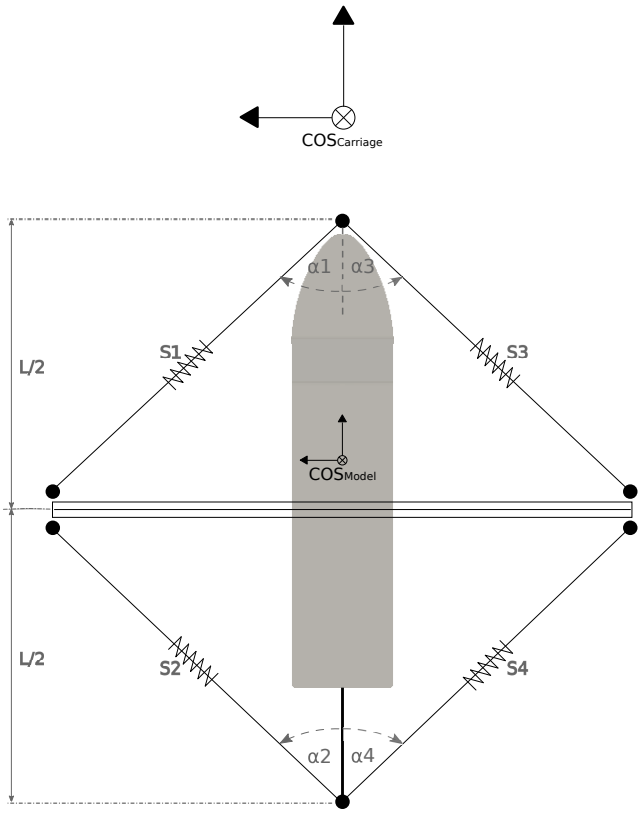

Figure 6.3: Sketch of the experimental setup for measuring the wave drift forces

6.2.2 Influence of wave steepness on wave drift force

Considering experiments to account for linear motion a wave steepness of $s = 0.03$ is appropriate ($s = H_w/\lambda$). However, depending on the wave frequency, the steepness effects the wave drift forces. Therefore, additional experiments in head waves with varying wave steepness from flat waves of $s = 0.02$ to steep waves of $s = 0.05$ for a wavelength of $\lambda/L \approx 0.6$ and $\lambda/L \approx 1.0$ were conducted.

The results of the experiments are illustrated as in figures 6.4-6.6. Comparing the model's response in both wave lengths, in shorter waves ($\lambda/L = 0.6$), the heave and pitch motion are of smaller magnitudes. The evaluated drift forces on figure 6.5 show an increase with the wave steepness with an approximated linear proportionality. Under consideration of the resultant non-dimensional drift forces, represented in figure 6.6, the effect of the wave steepness can be quantified for both wave lengths. Depending on the steepness the drift forces vary with 24% in case of the wave length equal to the ship length and 38% in case of the smaller wave length. For the latter approximation the measured drift force with wave steepness s=0.2 was not considered, due to small measured force in comparison with the accuracy of the experimental setup.

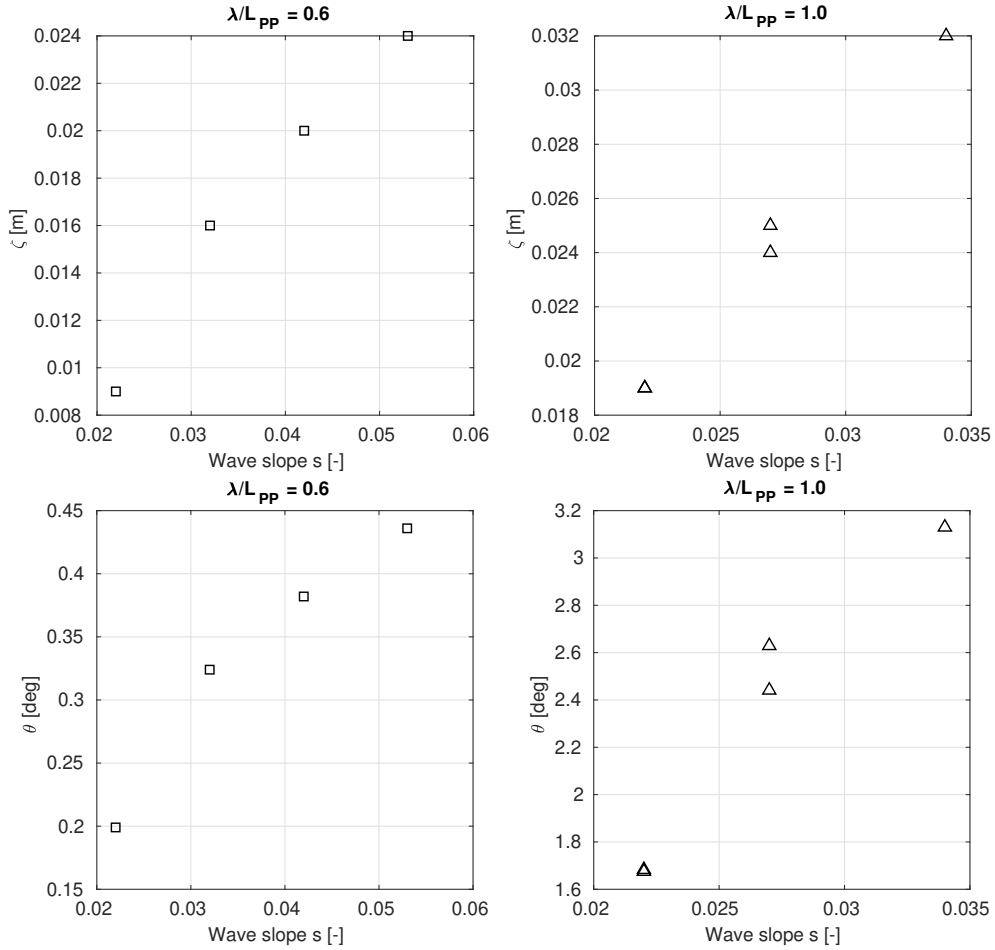

Figure 6.4: Measured heave (top) and pitch motion (bottom) in head waves under consideration of different wave steepness

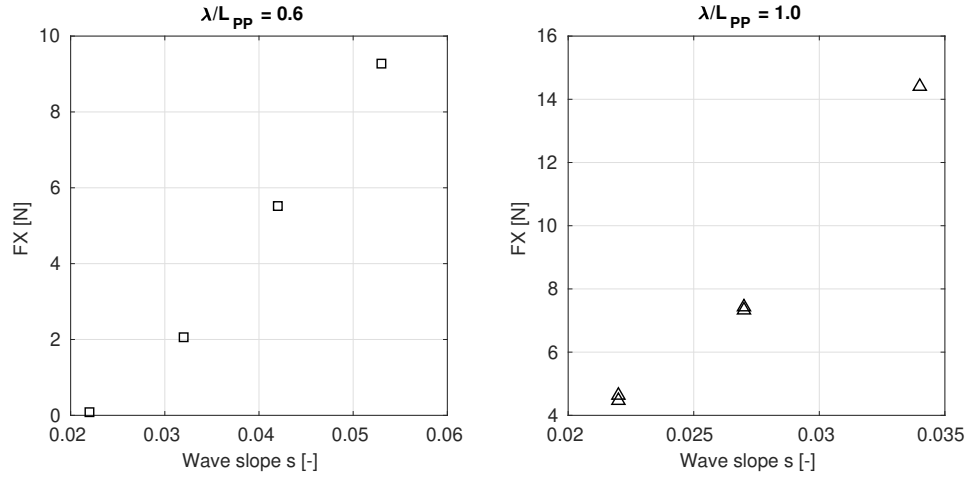

Figure 6.5: Measured drift forces in head waves under consideration of different wave steepness

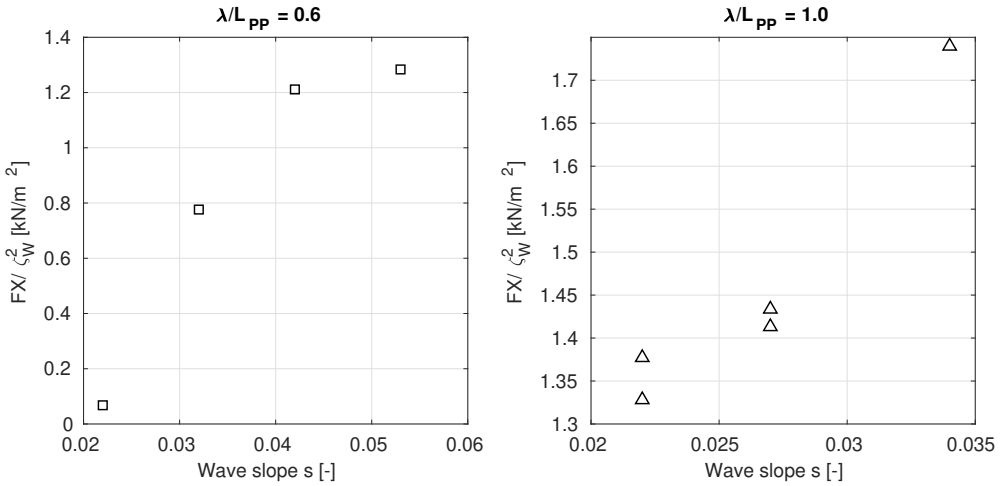

Figure 6.6: Response Amplitude Operators of the drift forces in head waves under consideration of different wave steepness

6.3 Numerical approach

Drift forces are time-averaged forces on the ship hull due to the interaction with waves. The forces on the ship in a seaway is to first order within a linear theory also a harmonically oscillating quantity. Hence, the time average of this quantity is zero. However, the ship experiences a non-zero contribution that exerts a directed drift motion. This contribution can be approximated using linear theory. Two leading assumptions are:

- Second-order pressure contributions are integrated over the average wetted surface
- First-order pressure contributions are integrated over the difference between the average and the instantaneous wetted surface, i.e. an integral over the contour of the waterplane.

With the assumption of small wave steepness the obtained contribution to the force is proportional to the incident wave amplitude squared.

6.3.1 Linear strip method

For the computation of the longitudinal and trasversal drift force as well as the yaw drift moment (in the upcomming denoted as the drift forces) the linear strip method is extended to a 2.5D method proposed by Söding [9]. Herein, the drift forces are separated in several contributions. For force contributions that are obtained from pressures integrated over the mean wetted hull surface, the sectionwise computed potential solutions are blended over a generated panel grid, hence longitudinal forces may be derived from the orientation of the normal vectors on each panel. Force contributions that consider the oscillating instantaneous wetted hull may be evaluated at two dimensional waterline segments.
The wave drift forces may be expressed by the following components:

$$\vec{F}_{Drift} = \begin{pmatrix} F_X^{(2)} \\ F_Y^{(2)} \\ F_Z^{(2)} \end{pmatrix} = \sum_1^{N_p} \left(\vec{f}_I + \vec{f}_{II} \right) + \sum_1^{N_{wl}} \vec{f}_{III} \tag{6.7}$$

where N_p and N_{wl} represent the number of panels and respective water line segments.
The first force contribution $\vec{f_I}$ accounts the periodical hull pressure and ship rotations. When setting up the equation for the pressure on each panel with a share of the complex amplitude of the oscillating pressure $\hat{p}$ and another with the rotativ motion vector $\hat{\vec{\alpha}}$ and neglecting the oscillating zero averaged terms, the following equation which contributes to the wave drift force:

$$\sum \vec{f}_I = -\frac{1}{2} Re(\sum_1^{N_p} (\hat{p}\, \vec{a}_0) \times \hat{\vec{\alpha}}^*) \tag{6.8}$$

The length of the normal vector $\vec{a}_0$ of each panel equals the panel area.
The second contribution $\vec{f_{II}}$ elaborated on the panel grid accounts the pressure due to the fluid velocity from Bernoulli's equation. The velocity of the fluid is denoted as $\vec{v}$. Analogous to the force contribution $\vec{f_I}$, terms that are independent of the wave and having zero time average are omitted. This yields to:

$$\sum \vec{f}_{II} = -\frac{1}{4} \rho \sum |\hat{\vec{v}}|^2\, \vec{a}_0 \tag{6.9}$$

The effect of variable hull immersion is considered by the third contribution $\vec{f}_{III}$. Here, the pressure acting on the difference between the average and the actual immersed hull surface is obtained from:

$$\sum \vec{f}_{III} = \frac{1}{4\rho g} \sum |\hat{p}|^2 \vec{n} \tag{6.10}$$

The pressure amplitude $\hat{p}$ in $\vec{f}_I II$ is the pressure at a ship-fixed mean waterline segment. The horizontal normal vector $\vec{n}$ on each segment is directed into the body.

The corresponding mean drift moments are obtained by considering the position vectors $\vec{x}$ of all grid panels and waterline segments:

$$\vec{M}_{Drift} = \begin{pmatrix} M_X^{(2)} \\ M_Y^{(2)} \\ M_Z^{(2)} \end{pmatrix} = \sum_1^{N_p} \vec{x} \times \left(\vec{f}_I + \vec{f}_{II} \right) + \sum_1^{N_{wl}} \vec{x} \times \vec{f}_{III} \tag{6.11}$$

6.3.2 Three dimensional panel method

Based on the flow potential Φ of the predefined compuational domain, the mean wave drift forces are determined as far field solution introduced by Newmann [59]. This method considers the rate of change of linear and angular momentum within a prescribed fluid domain to calculate the mean wave drift forces in the horizontal plane.
The rate of change of linear and angular momentum can be formulated by:

$$\frac{d\bar{G}}{dt} = -\rho \int_{S_t} \left[\left(\frac{p}{\rho} + gZ \right) \vec{n} + \vec{v}(v_n - u_n) \right] dS \tag{6.12}$$

$$\frac{d\bar{H}}{dt} = -\rho \int_{S_t} \left[(\vec{\xi} \times \vec{n}) \cdot \left(\frac{p}{\rho} + gZ \right) + (v_n - u_n) \cdot (\vec{\xi} \times \vec{v}) \right] dS \tag{6.13}$$

where S_t denotes all surfaces that are incorporated in the computational domain, i.e. the hull S, the free surface S_f and the domain sides S_{in}. The velocity normal to the boundary surface is represented by u_n, whereas the normal velocity of fluid on surfaces is v_n and $\vec{n}$ is the normal vector pointing outward from the fluid volume. The position vector $\vec{\xi}$ yields to a point on surface.
In case of zero forward speed the horizontal and forces and moment are obtained by:

$$F_{i\,Drift} = -\int_{S_{in}} (p n_i + \rho v_i v_n)\, dS - \frac{dG_i}{dt} \quad \text{with} \quad i = x, y \tag{6.14}$$

$$M_{z\,Drift} = -\int_{S_{in}} \left(\left(\vec{\xi} \times \vec{n} \right)_z p + \left(\vec{\xi} \times \vec{v} \right)_z n_n \right) dS - \frac{dH_z}{dt} \tag{6.15}$$

Since the second order potential makes no contribution to the mean wave drift in horizontal plane, the required potential to describe the fluid field needs only to be of first order. The first order potential is known from the solution of the linear radiation and diffraction problem. Considering the wave amplitude ζ_w of a harmonic wave and the Response Amplitude Operator (RAO) of motion in each degree of freedom x_j the source strengths of the diffraction σ_d and the radiation σ_j yield to:

$$\sigma_t(\vec{\xi}) = \zeta_w \cdot \left[\sigma_d(\vec{\xi}) + \sum_{j=1}^{6} \sigma_j(\vec{\xi}) x_j \right] \tag{6.16}$$

By applying the principle of linear superposition the flow potential Φ. Then the velocities in polar coordinates can be obtained:

$$v_r = \frac{\partial \Phi}{\partial r}; \qquad v_\psi = \frac{1}{r}\frac{\partial \Phi}{\partial \psi} \tag{6.17}$$

Averaging of the forces and moment in horizontal plane, and using the velocities in polar coordinates the mean drift forces are formed:

$$\bar{F}_x = -\int_{S_{in}} \overline{p\cos(\psi) + \rho v_r(v_r\cos(\psi) - v_\psi \sin(\psi))r}\; d\psi dz \tag{6.18}$$

$$\bar{F}_y = -\int_{S_{in}} \overline{p\sin(\psi) + \rho v_r(v_r\sin(\psi) - v_\psi \cos(\psi))r}\; d\psi dz \tag{6.19}$$

$$\bar{M}_z = -\int_{S_{in}} \overline{\rho v_r v_\psi r^2}\; d\psi dz \tag{6.20}$$

6.3.3 Field method for viscous flows

In the two previous described methods in the frequency domain, the mean wave drift forces could be derived from the potential flow. In the following section a description for the developed numerical set-up for the determination of wave forces based on field methods for viscous flows given.

6.3.3.1 Computational procedure

Analogues to the experiments, a RANS method has been applied using a similar setup with linear springs attached on the model to keep it in place. For the motion a six degree of freedom approach was set, where the model was entirely free to heave, pitch and roll and due to the springs partially free to sway, surge and yaw. An overset mesh technique has been used to separate the drift motion and the 1st order osculating motion from the rest of the domain (see figure 6.7). Fifth order Stokes waves with prescribing values of flow variables on the domain boundaries is applied for the wave generation in the computational domain. However, in order to prevent wave reflection, relaxed zones adjacent to the wave maker boundaries are set up.
A hexahedral mesh type was applied in the computational domain with three sequentially arranged refinements for the free surface. The finest level height was set corresponding to the wave height with 16 subdivisions in vertical direction. The size of the mesh involved 2.14 mio cells. The time stepping was set according to a CFL number < 1.
The computational domain size measured two ship lengths forward of the model and three lengths aft of the model. The height was set with a half ship length from still water level to top and one and a half length to the bottom, as well as to each domain side.

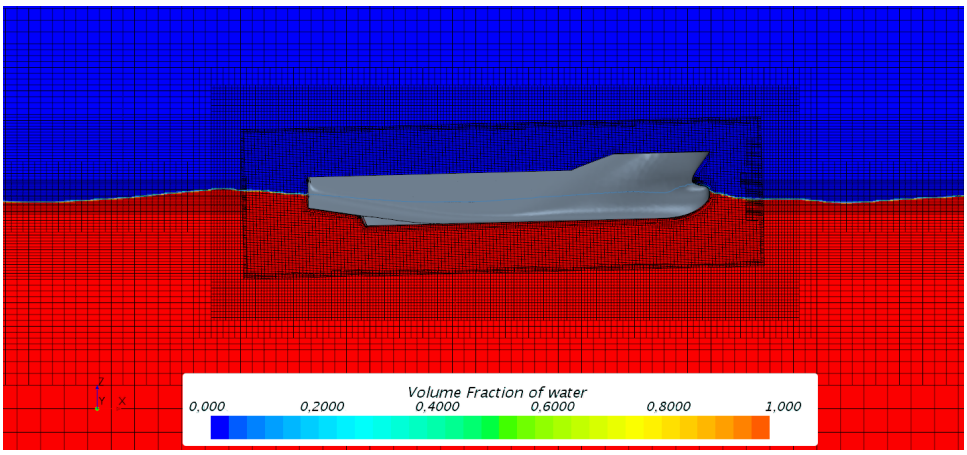

Figure 6.7: Volume fraction and overset mesh

6.3.3.2 Evaluation of wave drift loads

As in the experiments, the drift forces were determined by evaluating the spring forces. For this purpose, the mean value of the resulting force was determined. In figure 6.8 the resultant surge motion, the wave elevation and the body force as well as the spring force of a simulation with a wave length of $\lambda/L = 0.6$ is shown. The first order surge motion oscillates with an amplitude of $\xi_{amp} \approx 0.055m$. With the 2nd order wave forces, an equilibrium is reached with the spring forces. The model is displaced by $\Delta\xi = 0.11m$ in the longitudinal direction. The incident wave was monitored with a numerical wave probe about one and a half model lengths in front of the model. In line with the characteristic of fifth order Stokes waves, the wave crests show a steep course while the wave troughs are flattened. The body forces are obtained from pressure iteration over the wetted surface. While the body forces oscillate with the wave period ($T_{wave} = 1.4sec$), the spring forces are in phase with the surge motion ($T_{surge} = 12.8sec$). For the comparison with the experiments and the other numerical solutions the mean wave drift force is divided by the wave amplitude square:

$$Fx_{Drift} = \frac{fx_{spring}}{\zeta_w^2} = 1.06kN/m^2 \tag{6.21}$$

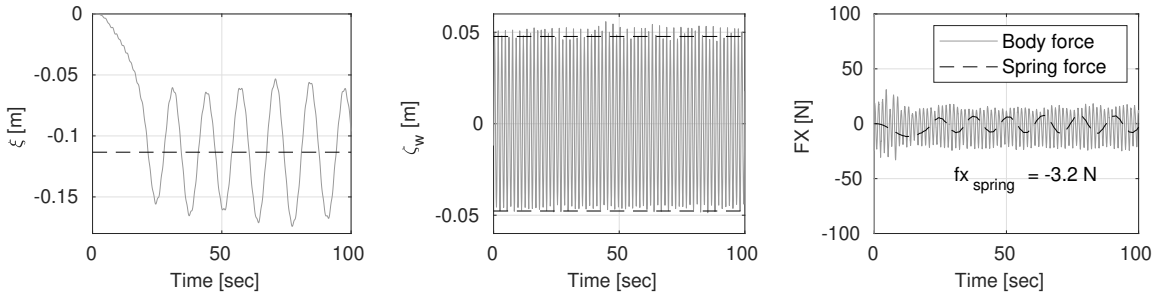

Figure 6.8: Simulation of the ship motion and forces for a wave length of $\lambda/L = 0.6$: (left) surge motion, (center) wave elevation, (right) longitudinal forces

6.4 Comparison of numerical and experimental results

In the following, the experimental results of the ship motion and the wave drift forces are compared with the numerical methods.

6.4.1 Ship motion

The results of the motion for quartering head waves are presented in figure 6.9 in the form of response amplitude operators. The resultant motion was normalized with the undisturbed wave amplitudes in case of the translational motion and additionally with the wave steepness in case of the rotational motion. In general, the computational results and the experiments follow the same trend. However, deviation is obtained for the pitch motion. Here, the results from the RANS simulation and the experiments comply with each other. But with increasing the wavelengths, the pitch motion is reduced in case of PDSTRIP and AQWA. One reason for increasing pitch motion in case of longer waves may be implied by the attached springs. The resultant motion for other encountering directions are attached in the appendix B.

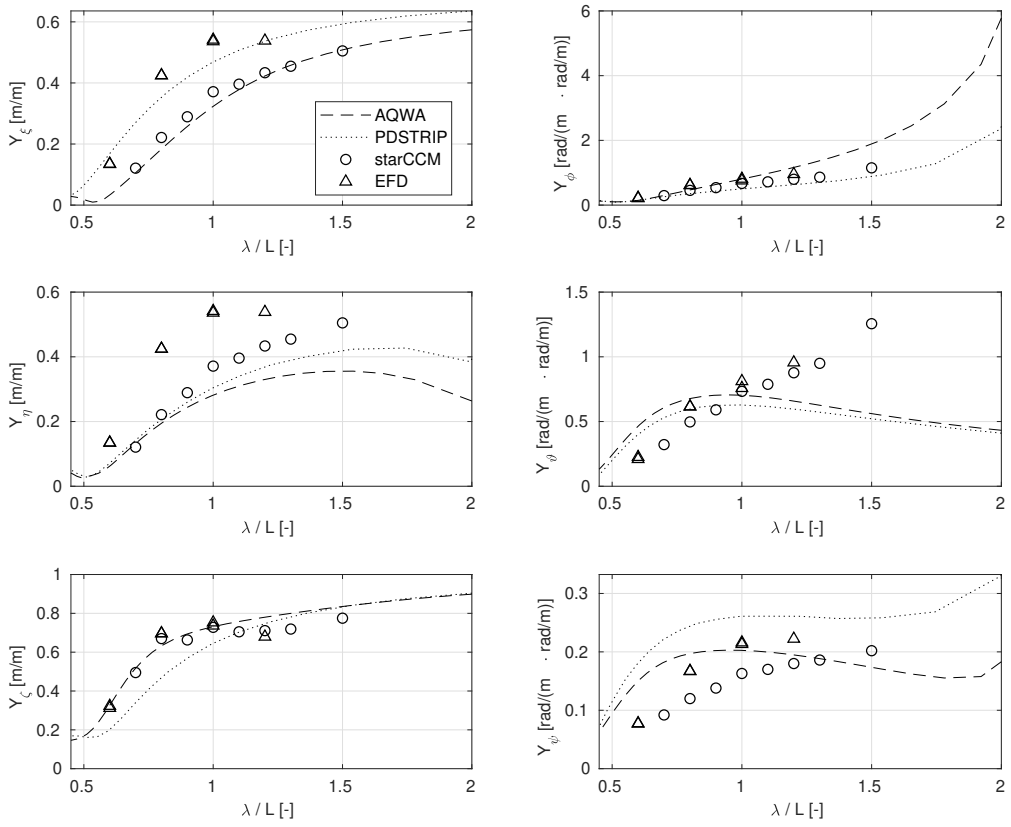

Figure 6.9: Response amplitude operator in quartering head waves

6.4.2 Wave loads

The results for quartering head wave loads are illustrated in figure 6.10. The loads are normalized by the square of the waves amplitude. While the strip methods clearly overestimates the wave loads obtained from experiments, the deviations from the panel method ANSYS AQWA and starCCM+ show a fair agreement. The wave loads nearly distinguish for waves longer than 1.2 of the ship length. One reason could be the reduction of the ship's motion relative to the wave, as the ship's motion follows the surface and the steepness of the wave as the waves get longer. Same holds for short wave lengths, where the energy of the waves are too small to exert motion on the ship. However, a small contribution is preserved by the reflection of the small waves on the ship hull, especially for transversal forces. The comparison for other encountering directions can be found in appendix B.

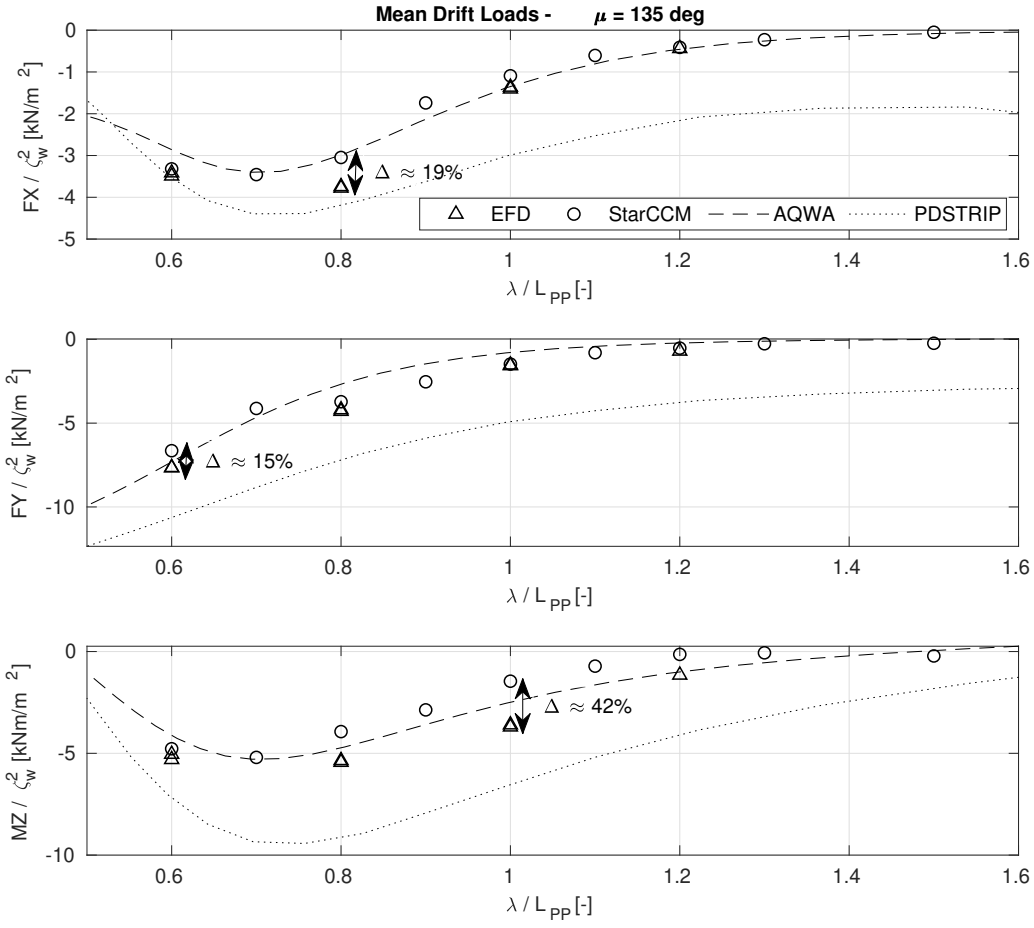

Figure 6.10: Comparison of wave drift loads in quartering head waves

Table 6.2: Required power during set point analysis

ϵ [deg]	EFD / CFD [%]
0	-4.89
45	-9.10
90	-11.70
135	-9.70
180	-3.65

6.5 Discussion

For the evaluation of the influence of wave drift force coefficients from experiments and CFD calculations (ANSYS AQWA), the data set from the experiments was interpolated with further grid points and extrapolated with CFD simulation values where no experiments were carried out. The peak period of the wave has been set according to a respective wave length equal to the ship length. Since the highest energy density is then modeled either from experimental or from CFD data this ensures a fair comparison between both approaches.
In figure 6.11 the resultant motion and the required power during a DP-operation are illustrated for head quartering waves of Beaufort 5. The required power in case of the wave loads obtained from CFD simulations is higher. The deviation for other encountering angles is summarized in table 6.2. It can be found that the largest deviation occurs for beam encountering waves.

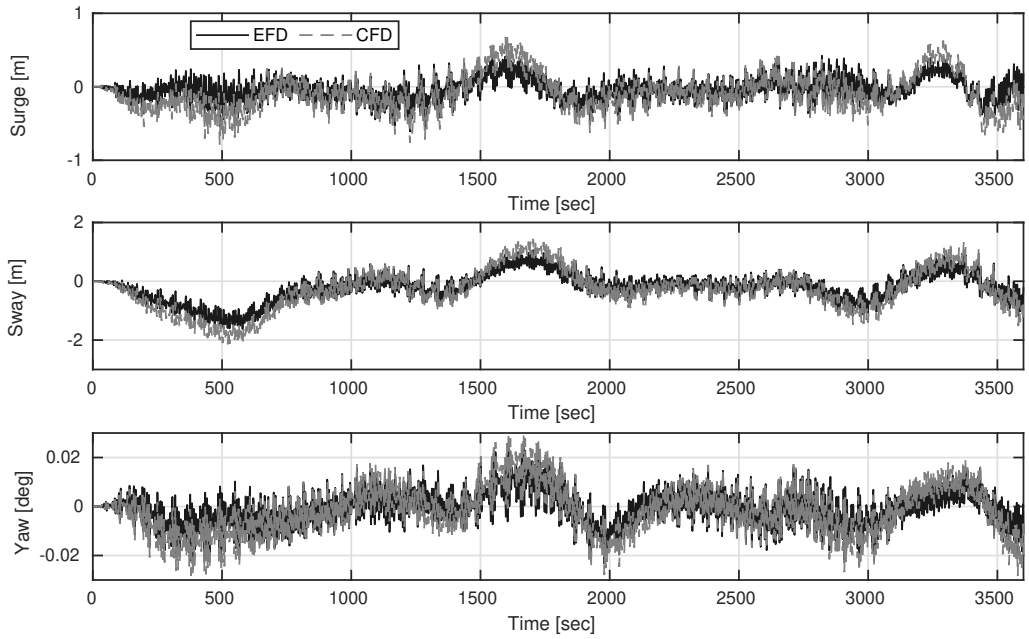

Figure 6.11: DP set point assessment for waves encountering from $\epsilon = 135deg$ - ship motion

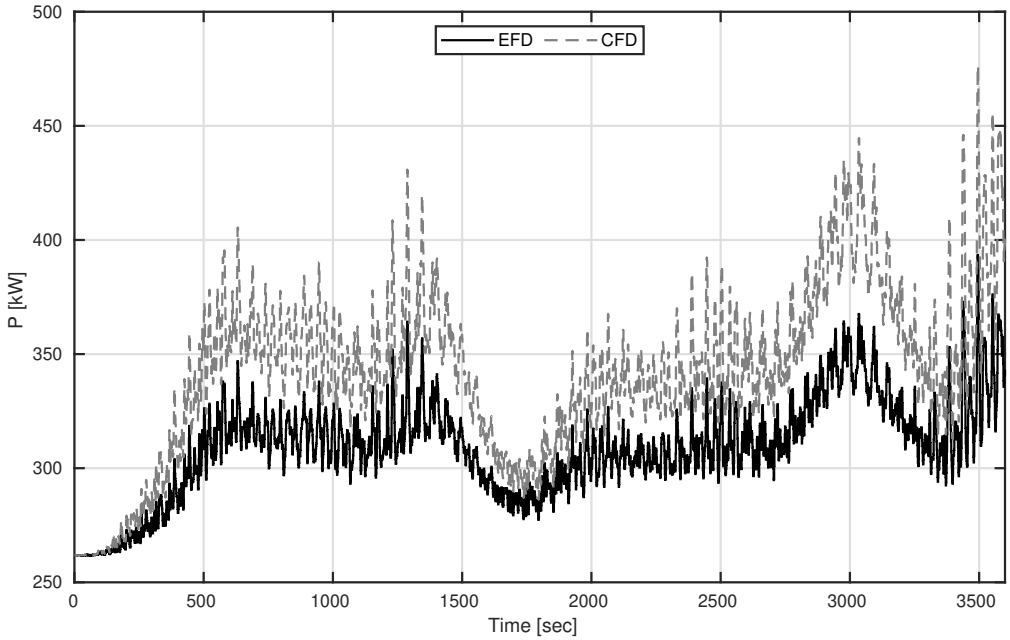

Figure 6.12: DP set point assessment for waves encountering from $\epsilon = 135deg$ - required power

7 Application

The application cases presented in the following chapter are exclusively applied to the OSV. The following section exemplifies the workflow of setting up an allocation arrangement, identifying a controller and simulating a dynamic capability plot in time domain. The hydrodynamic coefficients obtained from ANSYS AQWA for the ship motion simulation and the coefficients obtained from CFD simulation for accounting the environmental loads are calculated according to the present approach in the previous chapters.

7.1 Allocation

For the demonstration of the *DPTool* a realistic allocation setup for the OSV model was set. Further, an additional configuration with two azimuth thruster instead of the VSP is presented. The thruster arrangement is illustrated in figure 7.1. Three bow thrusters of different capacity were installed.

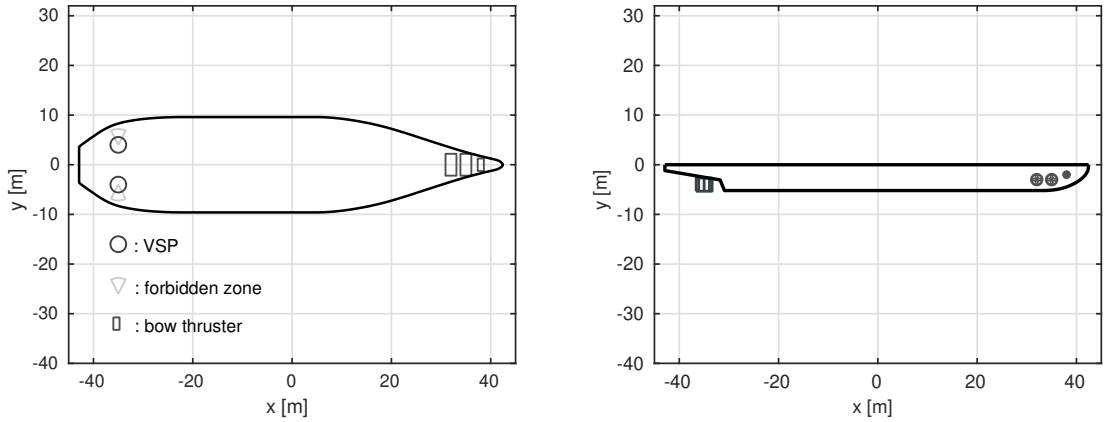

Figure 7.1: Typical thruster arrangement of the OSV model

Selected technical specifications of the used actuators are summarized in table 7.1. The reaction time indicates the time it takes for the maximum thrust force to change from one side to the other.

Both allocation settings are compered against each other in figure 7.2. The configurations were exposed to a sea state of Beaufort 9 encountering from beam side. The footprint of

Table 7.1: Thruster configuration

		VSP	AZI	BT 1	BT 2
P	[kW]	2500	2500	1400	800
n_{nom}	[rpm]	66	273	243	312
D	[m]	3.2	2.4	2.2	1.25
response Time	[sec]	5	45	-	-
Thrust	[kN]	361	354	210	120

the high and low frequency as well as the low frequency motion are illustrated. Comparing the maximum deviation of the position and heading angle, the setup with the VSP is slightly better in precision.

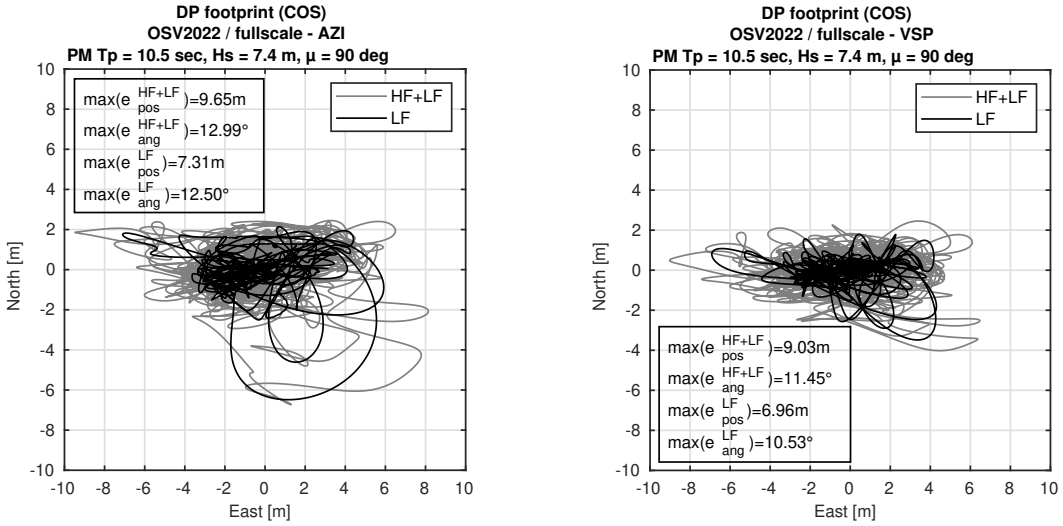

Figure 7.2: Comparison of footprint between allocation set with azimuth thruster (left) and VSP (right)

7.2 Setup of the controller

The *DPTool* allows the design and parametrizations of the controller and wave filter. For the application study the standard procedure has been applied.

Identification of DP process parameter

The design of the controller system starts with an identification of the mass **M** and damping **D** matrices of the underlying mathematical motion model from equation 3.14. The *DPTool* allows a manually created sequence of external forces according to the standard procedure. In figure 7.3 (left) the standard input is illustrated. Herein, a small impulse in the relevant degree of freedom is set. The correlated motion of the vessel is summarized on the right side of figure 7.3.

Together with the known external forces and the simulated motion of the vessel the mass

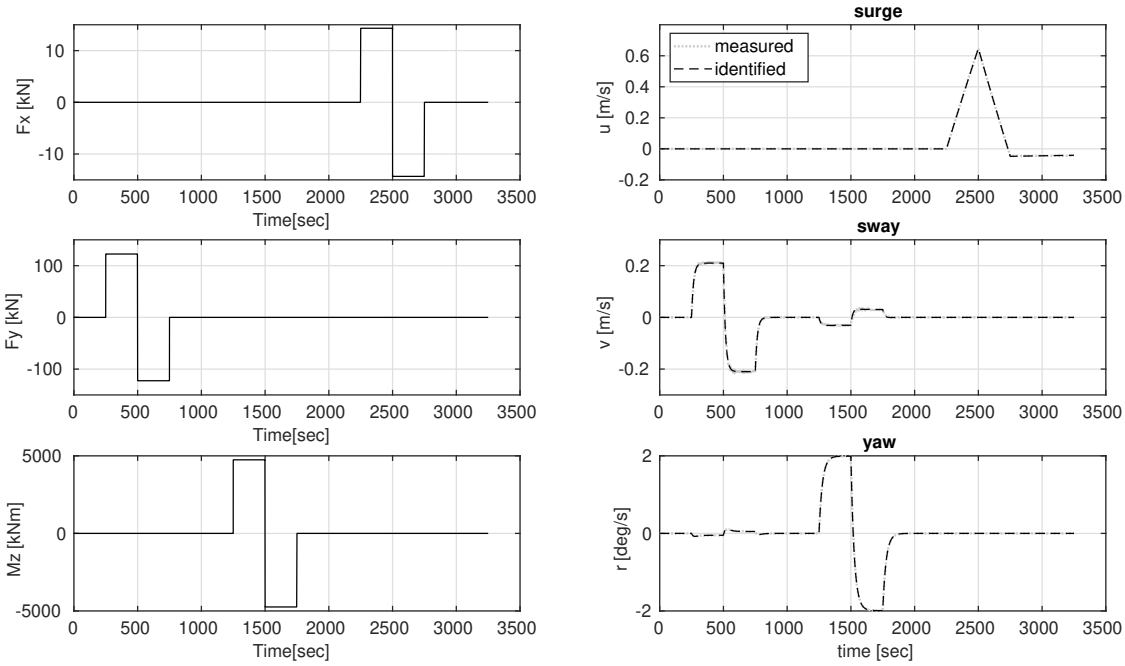

Figure 7.3: Identified trajectory of standard identification procedure

and damping matrices are developed by using the subspace identification method (SID). The resultant matrices yield to:

$$M = \begin{bmatrix} 5322.5 & 0 & 0 \\ 0 & 9344.1 & 16241 \\ 0 & 39141 & 3609500 \end{bmatrix} \quad ; \quad D = \begin{bmatrix} 1.65 & 0 & 0 \\ 0 & 585.69 & 515.01 \\ 0 & 555.22 & 136860 \end{bmatrix}. \tag{7.1}$$

Design and parametrization of DP controller

The controller design was developed according to the following setup:

In case of the allocation setup with two azimuth thruster, the design and parametrization yield to a maximum thrust of τ_{AZI} =[FX=708 kN, FY=540 kN, MZ=18.600 kNm] with a time span to achieve the maximum forces of δt =[15 sec, 22.5 sec, 21.7 sec]. For the VSP configuration a maximum thrust of τ_{VSP} =[FX=722 kN, FY=540 kN, MZ=18.600 kNm] in a time span of δt =[15 sec, 22.5 sec, 21.7 sec] can be achieved.

Observer & wave filter

The VSP has the advantage of short reaction times. Although the high-frequent ship motion may be within the bandwidth of the propulsion system and a direct correlation my lead to a better performance, the feeding of such components will increase mechanical wear an tear.
In order to obtain a feasible closed control feedback loop, the high-frequent ship motion oscillations caused by wind and waves should be excluded by filter algorithms. Hence, the position

- Controller type: nonlinear PID
- Design of three single input single output controller (SISO)
- Parametrization: LQ
- Anti-windup method: Off
- Output-filter: Off
- Max positioning error:

  [2.0 m 2.0 m 3 deg]

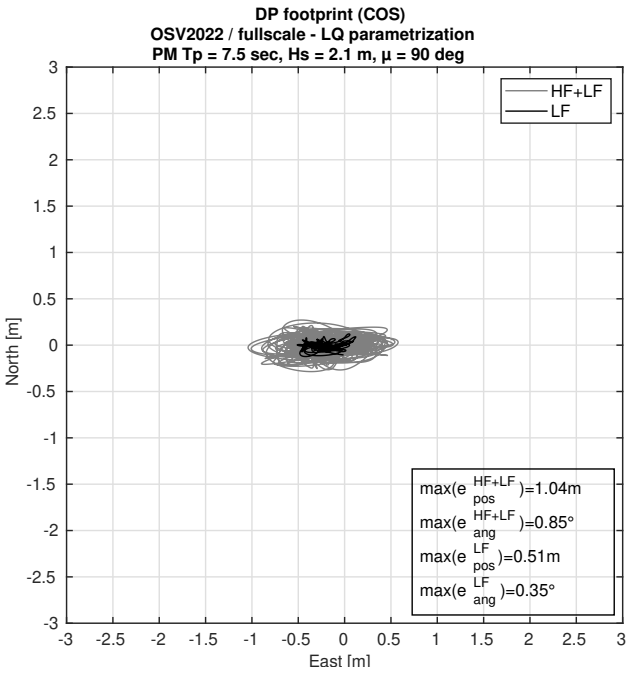

Figure 7.4: Controler setup (left) and example of a footprint (VSP) with LQ parametrization for Beaufort 5 encountering from beam side

and heading obtained from the ship motion simulation are seperated into a low-frequency and a high-frequency wave induced part. The wave-free position, heading and a velocity estimate are then used in feedback control.

For the application cases a nonlinear version of the Kalman filter is used, e.g. the extended Kalman filter (EKF). An example for a DP-simulation in beam seas of level 5 is illustrated in figure 7.5. The black line represents a linearized estimate of the current mean position an heading which is considered in the feedback control loop.

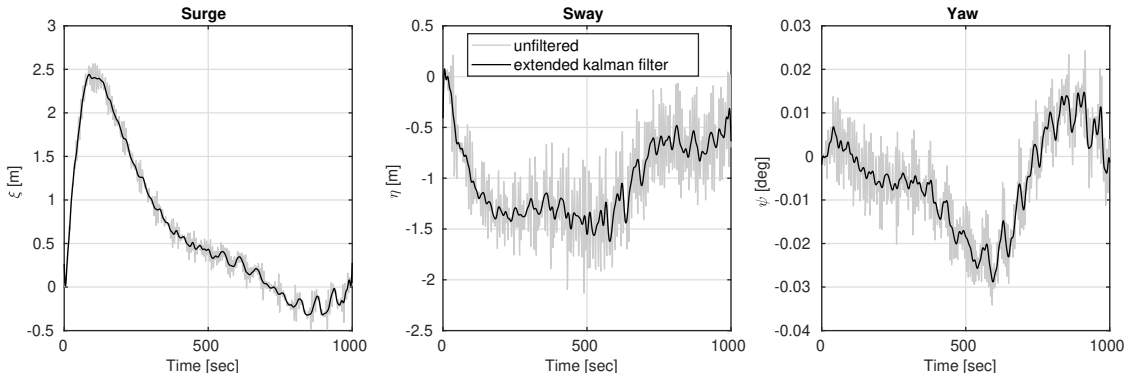

Figure 7.5: Filtered motion by extended Kalman filter algorithm

In order to arise the optimal performance of the VSP with its dynamical advantage, the identification of the filter parameter are deciding. In order to generate a good set of parameters a proceedure described in Hahn et al. [33] has been applied. The method uses ship responses in

a series of seaways prior to DP-simulation to identify the peak frequency of the entire system. This approach is based on a stationary state of the sea state and distinguishes between, for example, a broad and a narrow bandwidth of energy distribution, i.e. Pierson-Moskowith and JONSWAP seaway spectrum. Adaptive approaches according to Popov et al. [68] are also available, but not considered for the application cases.

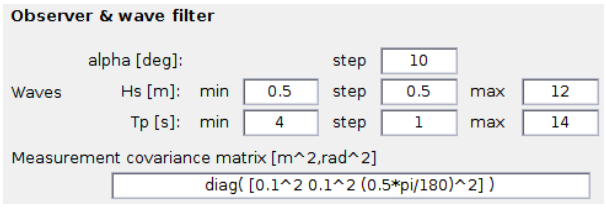

Figure 7.6: GUI for parameter input for the observer and wave filter design

7.3 Verification maneuvers

In the previous sections, the required power for a set point operation of the load coefficients from experiments was compared with those from CFD. In this section a comparison is conducted for all environmental loads. The simulation includes wind velocity of $v_w = 10m/s$, a current velocity of $v_c = 1m/s$ and seaway with a peak period of $T_P = 7.5sec$ and a significant wave height of $H_s = 2.1m$. The resultant motion is shown in figure 7.7 and the corresponding power is illustrated in figure 7.8. The deviations for all encounter angles are summarized in table 7.2.

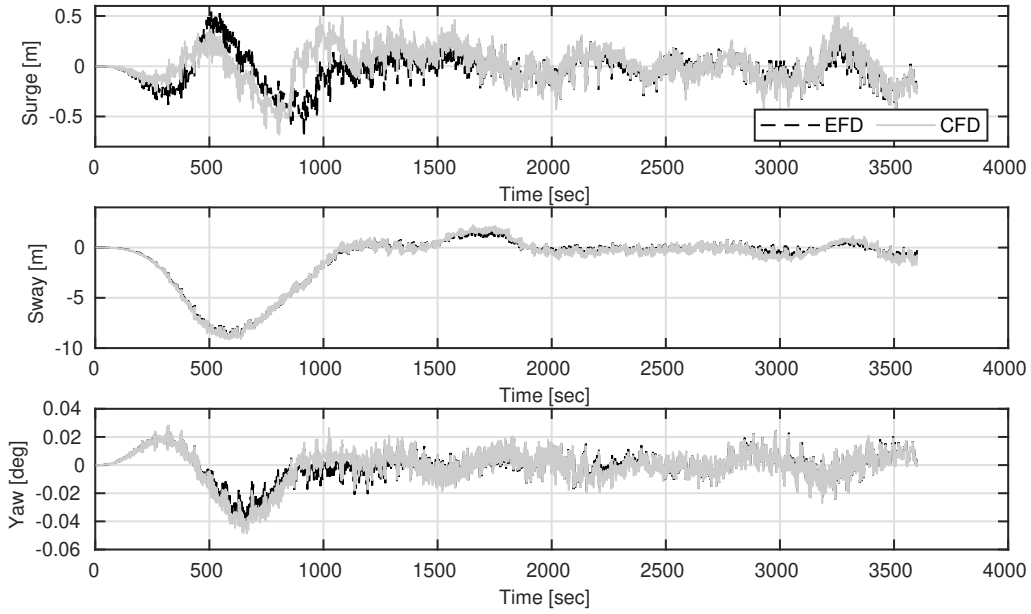

Figure 7.7: DP simulation environmental loads encountering from 135 deg (BFT 5)

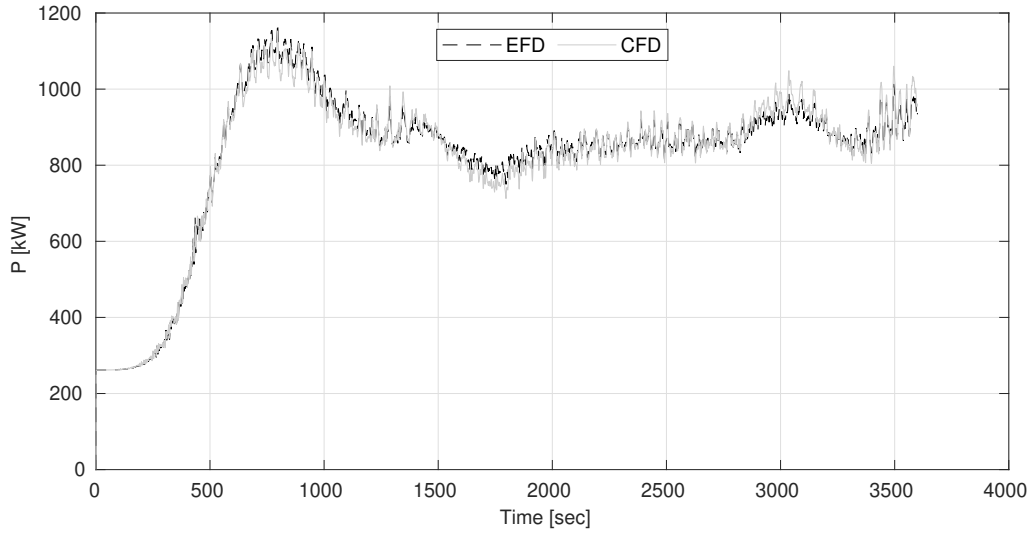

Figure 7.8: DP simulation environmental loads encountering from 135 deg (BFT 5)

The deviation between the resultant required power for environmental loads from experiments and from CFD simulation is summarized for varying encounter angles in table 7.2. It is shown that coefficients based on CFD overestimate by about 10 % according to the underlying encountering directions.

Table 7.2: Required power during set point analysis

ϵ [deg]	EFD / CFD [%]
0	-8.63
45	-10.53
90	-3.41
135	0.10
180	-6.23

Another verification is represented by a set point simulation for environmental loads encountering from 180 deg at Beaufort 6. The resultant motion is shown in figure 7.9. The surge and sway motion maintain the position within the limits of 3 m and the yaw motion varies with 2 deg of heading. The heave, roll and pitch motion result in moderate amplitudes for significant wave height of $H_{1/3} = 3.1m$.
In figures 7.10 and 7.11 the resultant environmental loads split in the respective load type and the correlating allocation forces are shown. The representation of the current forces include the force fluctuation due to the ships velocity. According to the load variation, a mean longitudinal force of $F_X \approx 33$ kN can be expected. The resultant allocation forces show that the required forces can be successfully achieved. The diagram of the individual force components shows that one VSP was used to maintain the force in the longitudinal direction and the second divides the force in order to balance the transversal force and the yaw moment.

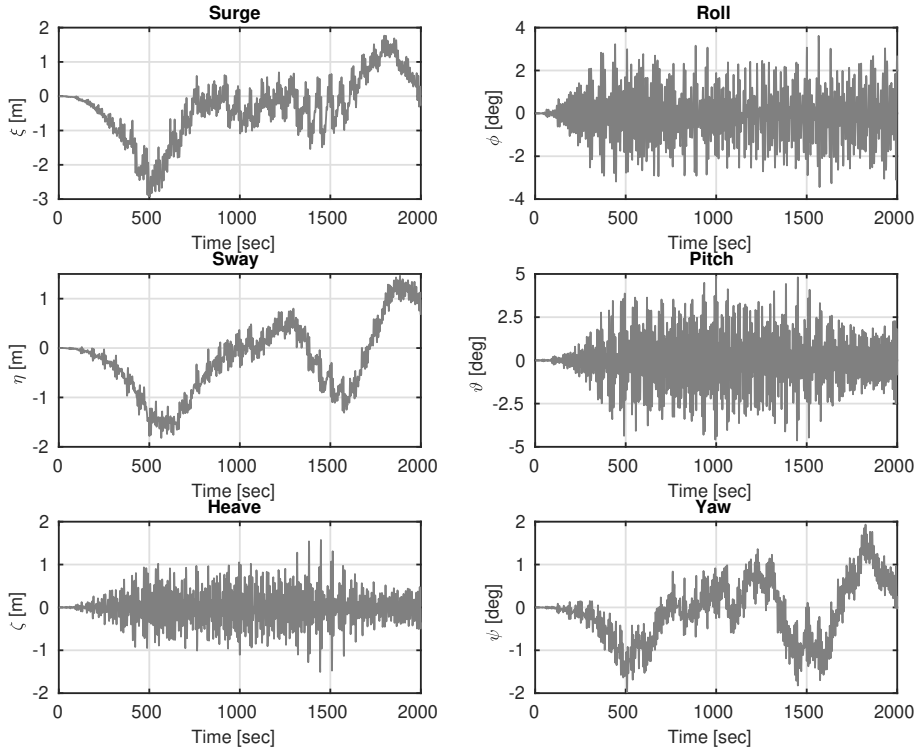

Figure 7.9: Resulting ship motion of DP simulation with encountering loads of 180 deg at Bft 6

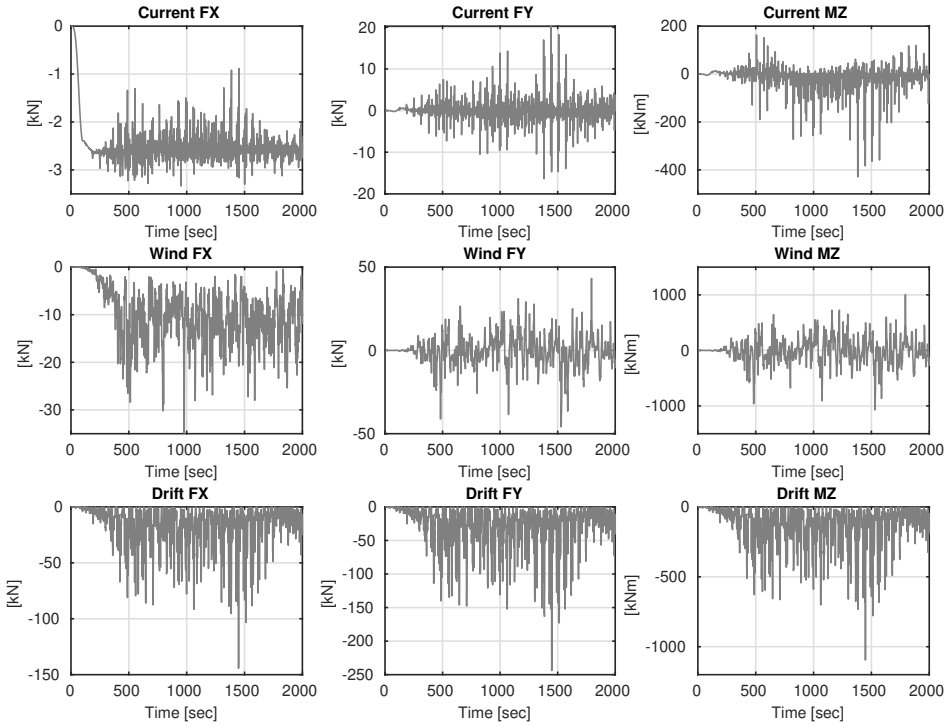

Figure 7.10: Resulting environmental loads in time domain for a DP simulation of Bft 6 with encountering direction of 180 deg

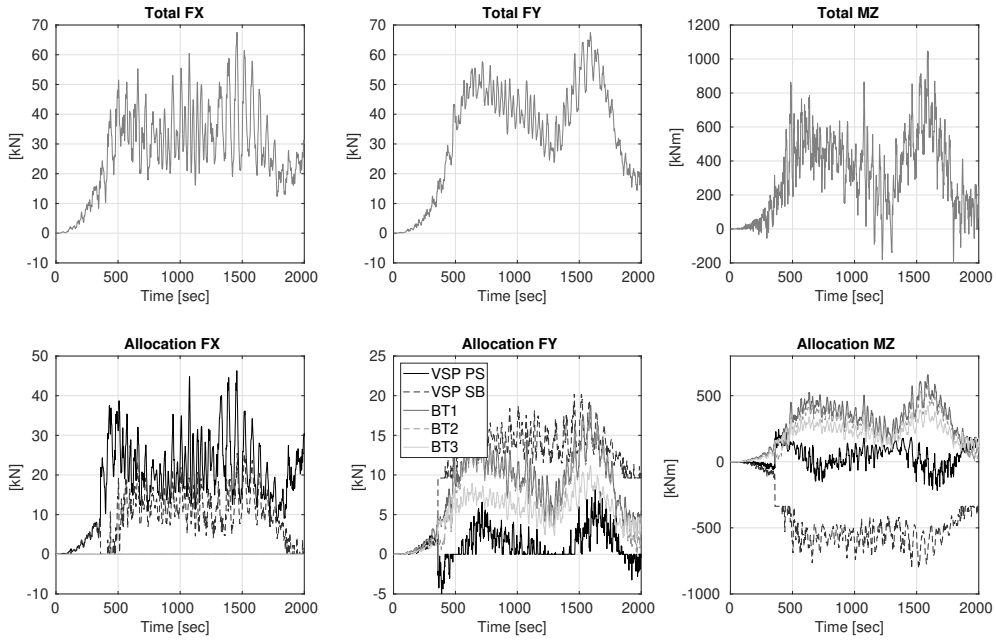

Figure 7.11: Allocation forces of propulsion plants for Bft6 and encountering direction of 180 deg

The control parameters of the actuators are presented in figure 7.12. In this diagram it can also be seen that the VSP on the SB side compensates for the lateral motion, while the rudder parameter of the VSP on PS fluctuates around zero. The bow thrusters operate simultaneously.

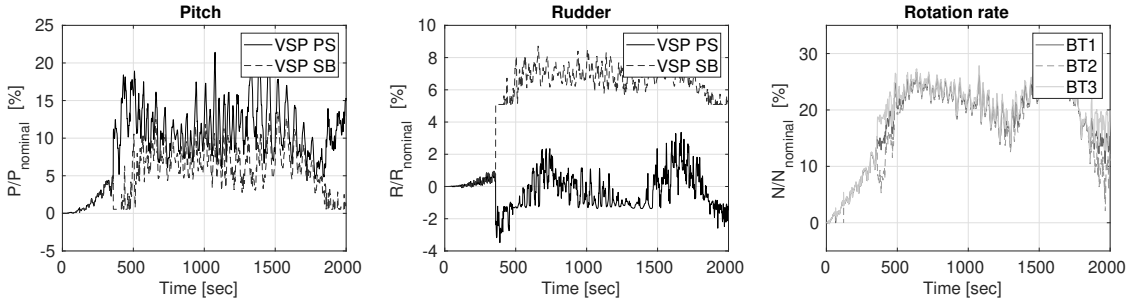

Figure 7.12: Resulting control parameter of VSP and bow thruster

7.4 Static and dynamic assessment

The dynamic capability of the OSV model is shown in figure7.13. The resultant limits are represented by the Beaufort levels summarized in table 7.3. The static and dynamic simulation show the typical restrictions in keeping position due to quartering waves. The differences between the static and the dynamic results arise from the dynamic control in time domain. The applied criteria for holding the position were set to 5 m in radial deflection and three degrees in heading. For each simulation a time span of 5400 sec was analyzed.

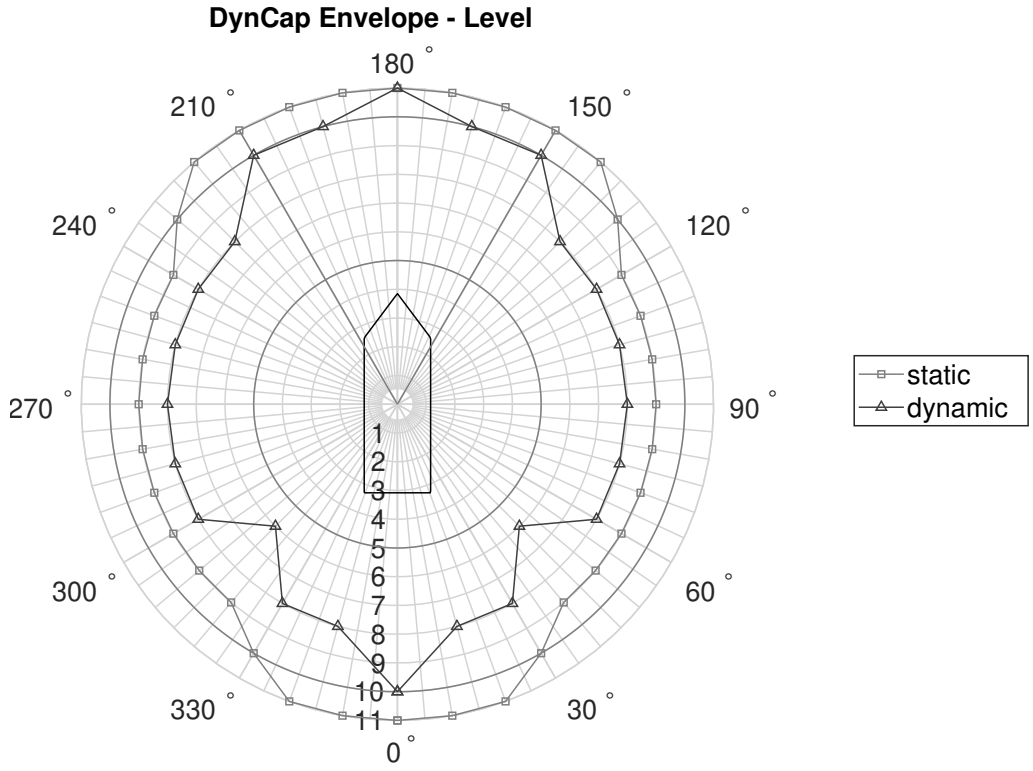

Figure 7.13: Comparison between static and dynamic capability in a polar diagram (VSP allocation)

Table 7.3: Environmental parameter according to [23]

DPCap number	Wind Speed v_w [m/sec]	Sig. wave height $H_{1/3}$ [m]	Peak period T_p [sec]	Current speed v_c [m/sec]
1	1.5	0.1	3.5	0.25
2	3.4	0.4	4.5	0.50
3	5.4	0.8	5.5	0.75
4	7.9	1.3	6.5	0.75
5	10.7	2.1	7.5	0.75
6	13.8	3.1	8.5	0.75
7	17.1	4.2	9.0	0.75
8	20.7	5.7	10.0	0.75
9	24.4	7.4	10.5	0.75
10	28.4	9.5	11.5	0.75
11	32.6	12.1	12.0	0.75

8 Conclusion and perspectives

In the thesis the development and application of a closed-loop simulation platform (*DPTool*) for evaluating the DP capability of typical DP vessels with Voith-Schneider-Propeller are presented. Realistic environmental loads, i.e. wind, waves and current, have been numerically and experimentally studied and then verified and considered in application cases.
The numerical framework of the *DPTool* is seperated in the treatment of the vessel's motion, the controler setup and the allocation module. For the holistic approach all components were combined in a MATLAB/Simulink model. The ship motion has been simulated by using the method *IMPRES* [20] based on potential theory. The hull forces were computed in frequency domain and then transfered into the time domain by using the impulse response functions. Additional correction for viscose longitudinal damping and for the roll motion have been applied. The DP-System is designed as a non-linear PID feedback-control system with a Kalman filter-based observer [43]. For the allocation module a constrained, multi-criteria optimization algorithm [35] was applied to find the desired forces in a short period of time, but also in a energy-efficient way. A graphical user interface for the usability was designed and implemented. The functionality has been separated into a project management for controlling hydrodynamic forces, the setup of the allocation and the design of the controller. A job manager was designed for various application cases.
The numerical methods for determining the environmental loads were successfully validated against experiments. In conclusion of the investigation, for each environmental load component a comparative simulation with coefficients from experiments and CFD were carried out to assess the effects of deviating force components. The resulting power required to maintain the position was evaluated. It was found that wind and wave loads are underestimated by the underlying CFD methods with about 7 % and 12 % while current loads overestimate by about 12 %.
The OSV model and the TUG model were tested in the wind tunnel. In advance of the measurement of wind loads, the influences of the natural boundary layer in the wind tunnel have been investigated. This revealed that the boundary layer had a thickness of about 7cm. For the TUG model and the OSV model, a comparison was made between the analytical and numerical correction for the transfer of wind loads for uniform flow condition. The influence on the lateral force was up to 14 % in the case of the OSV and 3.8 % in the case of the TUG model. Repeated measurements with different directions of rotation revealed the influence of detaching and attaching vortices. This effect caused deviations of about 4-5 %. An investigation of the influence of different wind speeds using the TUG model as an example showed a deviation of about 17 %. The influence of heeling was also investigated on this model. The forces increased

by about 16 %. The effect of additional deck equipment was tested using the example of a crane. Here, the largest differences were found with 25 %. An investigation was conducted to develop an efficient numerical setup for the simulation of the wind loads was carried out by testing two discretisation methods (tetrahedral and polyhedral cells) in a grid study. The comparison of the results showed that the most efficient method is represented by polyhedral cells with a steady-state RANS solver. The grid size was about 0.8 mio cells. The realizable $k-\epsilon$ turbulence model was used with an average Y+ $\approx$ 90. The deviation to the DP-relevant measured wind loads yield to about 9% in case of the OSV model and 14 % for the TUG model. Comparative simulations were carried out with DES. Here, the deviations could be significantly reduced.

The current forces were measured for the OSV model in a tank basin. Current flow has been applied by attaching the model with a load balance on the carriage and accelerating it to the desired velocity. Natural oscillations of the experimental setup were filtered by suitable Fourier transforms. For the numerical approach three methods have been compared: steady-state RANS, transient RANS and DES. The domain setup was modeled in cylindrical shape with polyhedral cells. It was found that the $k-\omega-SST$ model with no wall function gave best results. A grid study resulted in a grid size of 1.6 mio cells. The comparison between the three methods showed that with the DES method the smallest deviations from the experiment can be achieved. Thereby, the numerical methods underestimate the experiment. In case of the steady-state approach the maximum deviation yield to 26 %.

For the measurements of the wave loads the OSV model was attached to a cross frame with four linear springs. The forces were measured in the springs as well as with a load balance that was mounted on the cross section. First tests were conducted for head waves with different wave slopes (flat waves s=0.02 to steep waves s=0.05). In case of short waves ($\lambda/L \approx 0.6$) drift forces become smaller with increasing wave slope and for longer waves vice versa. The forces varied up to 20 % in magnitude. The same trends hold for the pitch and the heave motion. Further, three numerical methods were applied for the computation of the drift forces: a two-dimensional strip method PDSTRIP [9], a three-dimensional panel method ANSY AQWA [5] and a RANS method StarCCM+ [77]. The model motion and the forces were compared with the experiments. It was found, that the strip method was not applicable for the drift forces. The deviation in wave loads of about 30 % were obtained.

The functionalities of the *DPTool* were demonstrated in an application case with a static and a dynamic DP capability assessment. The simulations were conducted with the OSV model. A realistic allocation was set with two VSP and three bow thruster. The arrangement has been compared with two azimuth thruster instead. The VSP configuration yield to a slightly smaller power demand and thus footprint of 7%.

The developed methods integrated in the *DPTool* can be improved and extended with new developments in future studies. Concerning the allocation module, the integration of different rudder types as well as twin screw shaft lines may be desirable to open the *DPTool* for other ship types. Further model tests on DP capability in different sea state, current and wind configurations increase the reliability of the numerical results. In addition, the DP system for

the ship can be further developed. In the first step, the *DPTool* can be used for the basic design of the allocation and the controller, i.e. among others the required power and number of thrusters. To ensure save DP-Operations the *DPTool* may be reconfigured as a part of a Hardware-in-the-Loop (HIL) system. This function lays out manifold tests for Failure Mode and Effects Analysis (FMEA).
Several research topics are conceivable for the further development of the DP controller: The controller can be extended by a pre-trained neural network that supports adaptive sea states, i.e. the changes from lower to higher states with increasing wind during a DP operation. Another improving feature may be the integration of a wind feedforward system that uses real-time simulation in parallel. Different types of controller can be designed with the *DPTool*. The designs may range from a 'green DP-Mode', where the controller is more optimized for low energy consumption, up to 'high performance DP-Mode' that focuses on very accurate positioning.

Bibliography

[1] Aalbers, A. ; Jansen, R.B.H.J. ; Kuipers, R.J.P.E. ; Van Walree, F.: Developments in dynamic positioning systems for offshore stationkeeping and offloading. In: *The Fifth International Offshore and Polar Engineering Conference, The Hague*, 1995

[2] Aalbers, A. ; Nienhuis, U.B.: Wave direction feed-forward on basis of relative motion measurements to improve dynamic positioning performance. In: *Offshore Technology Conference, Houston*, 1987

[3] Aalbers, A. ; Waals, O.J. ; Tap, R.F. ; Davison, N.J.: Wave feed forward DP and analysis of the effect on Shuttle Tanker Operation. In: *Dynamic Positioning Conference, Houston*, 2004

[4] Andersen, I.M.V.: Wind loads on post-panamax container ship. In: *Ocean engineering* 58 (2013), S. 115–134

[5] ANSYS, AQWA: AQWA theory manual. In: *ed. Canonsburg, PA 15317, USA* (2015)

[6] Antheunisse, W. ; Chalkias, D. ; Huijsmans, R.: Offset Requirements in Quasi Static DP Capability Calculations. In: *The 26th International Ocean and Polar Engineering Conference, Rhodes*, 2016

[7] Arslan, T. ; Pettersen, B. ; Andersson, H.I.: Large-eddy simulation of cross-flow around ship sections. In: *Journal of Marine Science and Technology* 21 (2016), Nr. 3, S. 552–566

[8] Augener, P.H. ; Krüger, S.: Computation of drift forces for dynamic positioning within the very early design stage of offshore wind farm installation vessels. In: *International Conference on Offshore Mechanics and Arctic Engineering* American Society of Mechanical Engineers, 2014

[9] Bertram, V. ; Söding, H.: *Program PDSTRIP: Public Domain Strip Method*. 2014. – Manual

[10] Blendermann, W.: Parameter identification of wind loads on ships. In: *Journal of Wind Engineering and Industrial Aerodynamics* 51 (1994), Nr. 3, S. 339–351

[11] Blendermann, W.: Estimation of wind loads on ships in wind with a strong gradient. In: *OMAE* Bd. 1, 1995, S. 271–277

[12] Boese, P.: Eine einfache Methode zur Berechnung der Widerstandserhöhung eines Schiffes im Seegang. 1970. – Forschungsbericht

[13] Boom, H.J.J. van d. ; Nienhuis, U.: Hydrodynamic analysis of dynamically positioned vessels. In: *International Workshop on Ship and Platform Motions*, 1983

[14] Brandner, A.: Allokationsmodul für Voith-Schneider und Azimutpropeller / Technical report, Universität Ulm and Voith Turbo Marine. 2014. – Forschungsbericht

[15] Brix, J.: *Manoeuvring Technical Manual*. Seehaven Verlag, 1992

[16] Clauss, G. ; Lehmann, E. ; Östergaard, C.: *Offshore Structures: Volume II Strength and Safety for Structural Design*. Springer Science & Business Media, 2012

[17] Cummins, W.E.: The impulse response function and ship motions. In: *Report 1661, Department of the Navy, David W. Taylor Model Basin, Hydromechanics Laboratory, Research and Development Report*, 1962

[18] Davenport, A.G.: The spectrum of horizontal gustiness near the ground in high winds. In: *Quarterly Journal of the Royal Meteorological Society* 87 (1961), Nr. 372, S. 194–211

[19] Detlefsen, O.: *Entwicklung eines Verfahrens zur Simulation von Schiffsbewegungen und dynamischem Positionierem im Seegang unter Verwendung von Impuls-Antwort-Funktionen.* Technische Universität Hamburg-Harburg, Masterarbeit, 2014

[20] Detlefsen, O. ; Theilen, L. ; Abdel-Maksoud, M.: Time domain simulation of dynamic positioning manoeuvres based on impulse response functions. In: *VI International Conference on Computational Methods in Marine Engineering*, 2015

[21] Detlefsen, O. ; Theilen, L. ; Abdel-Maksoud, M.: Static and Dynamic Analysis Methods of Position-Keeping Capability for Offshore Supply Vessels With Voith-Schneider Propellers. In: *International Conference on Offshore Mechanics and Arctic Engineering* American Society of Mechanical Engineers, 2017

[22] Deutsche WindGuard: *Status des Offshore-Windenergieausbaus in Deutschland.* `https://www.windguard.de`. Version: (Januar 2022). – Last accessed 16 January 2022

[23] DNV, GL: Assessment of station keeping capability of dynamic positioning vessels. In: *DNV GL AS* (2016)

[24] Donnarumma, S. ; Figari, M. ; Martelli, M. ; Vignolo, S. ; Viviani, M.: Design and validation of dynamic positioning for marine systems: A case study. In: *IEEE Journal of Oceanic Engineering* 43 (2017), Nr. 3, S. 677–688

[25] Faltinsen, O.M.: Prediction of resistance and propulsion of a ship in a seaway. In: *Proceedings of the 13th symposium on naval hydrodynamics, Tokyo, 1980*, 1980

[26] Fathi, F. ; Klaij, C. ; Koop, A.: Predicting Loads on a LNG Carrier with CFD. In: *International Conference on Offshore Mechanics and Arctic Engineering* Bd. 49149, 2010, S. 427–440

[27] Fossen, T.I.: *Handbook of marine craft hydrodynamics and motion control*. John Wiley & Sons, 2011

[28] Fossen, T.I. ; Perez, T.: Kalman filtering for positioning and heading control of ships and offshore rigs. In: *IEEE control systems magazine* 29 (2009), Nr. 6, S. 32–46

[29] Fujiwara, T. ; Ueno, M. ; Nimura, T.: Estimation of wind forces and moments acting on ships. In: *Journal of the Society of Naval Architects of Japan* 1998 (1998), Nr. 183, S. 77–90

[30] Garratt, J.R.: Review of drag coefficients over oceans and continents. In: *Monthly weather review* 105 (1977), Nr. 7, S. 915–929

[31] Gould, R.W.: The estimation of wind loads on ship superstructures. Royal Institution of Naval Architects, 1982. (Maritime technology monograph). – Forschungsbericht

[32] Haddara, M.R. ; Soares, C.G.: Wind loads on marine structures. In: *Marine Structures* 12 (1999), Nr. 3, S. 199–209

[33] Hahn, T. ; Koschorrek, P. ; Jeinsch, T.: Parameter estimation of wave-induced oscillatory ship motion for wave filtering in dynamic positioning. In: *IFAC-PapersOnLine* 51 (2018), Nr. 29, S. 183–188

[34] Hess, J.L. ; Smith, A.M.O.: Calculation of nonlifting potential flow about arbitrary three-dimensional bodies. In: *Journal of ship research* 8 (1964), Nr. 04, S. 22–44

[35] Huber, C. ; Palm, M. ; Leger, A.: *DPMotion : Dynamic Positioning von Schiffen und Plattformen mit Motionstabilisierung unter Verwendung von x-y-Logik*. (2016). – Technical Report 03SX351A, 01141705, Heidenheim, Voith Turbo GmbH & Co. KG

[36] Hughes, G.: Model experiments on the wind resistance of ship. In: *Summer Meeting of the 71st Session of the Royal Institution of Naval Architects, RINA Transactions: 1930-19, July*, 1930

[37] IMCA, M: 140 Rev. 1. Specification for DP Capability Plots. In: *IMCA, London* (2000)

[38] Inc., WAMIT: *User Manual, Versions 6.4, 6.4 PC, 6.3, 6.3 S-PC*. 2006

[39] Institute for fluid dynamics an ship theory: *Large Low-Speed Wind Tunnel at TUHH*. `https://www.tuhh.de/fds/institute/experimental-and-computing-facilities/large-low-speed-wind-tunnel.html`. Version: 2020. – Last accessed 1 October 2022

[40] International Renewable Energy Agency: *Renewable Energy Statistics 2022*. https://www.irena.org/publications/2022/Jul/Renewable-Energy-Statistics-2022. Version: (April 2022). – Last accessed 16 January 2022

[41] Isherwood, R.M.: Wind resistance of merchant ships. In: *The Royal Institution of Naval Architects* 115 (1972), S. 327–338

[42] Janssen, W.D. ; Blocken, B. ; Wijhe, H.J. van: CFD simulations of wind loads on a container ship: Validation and impact of geometrical simplifications. In: *Journal of wind engineering and industrial aerodynamics* 166 (2017), S. 106–116

[43] Jeinsch, T. ; Drewelow, W. ; Haghani, A. ; Koschorrek, P. ; Siebert, C.: *DPM-control - Integriertes Steuerungs- und Regelungskonzept mit Voith-Schneider-Propellern*. (2016). – Technical Report 03SX351D, 01141705, Rostock, Universität Rostock

[44] Journée, J.M.J. ; Massie, W.W.: *Offshore hydromechanics*. CITG Section Hydraulic Engineering, 2000

[45] Jürgens, D. ; Palm, M. ; Brandner, A.: Comparative investigation on influence of the positioning time of azimuth thrusters on the accuracy of dp. In: *Dynamic Positioning Conference, Houston*, 2012

[46] Koop, A. ; Yeon, S. ; Yu, K. ; Loubeyre, S. ; Xu, W. ; Huang, J. ; Vinayan, V. ; Agrawal, M. ; Kim, J.: Development and Verification of Modeling Practice for CFD Calculations to Obtain Current Loads on FPSO. In: *International Conference on Offshore Mechanics and Arctic Engineering* Bd. 1 American Society of Mechanical Engineers, 2020

[47] Koschorrek, P. ; Siebert, C. ; Haghani, A. ; Jeinsch, T.: Dynamic positioning with active roll reduction using voith schneider propeller. In: *IFAC-PapersOnLine* 48 (2015), Nr. 16, S. 178–183

[48] Koschorrek, P. ; Siebert, C. ; Theilen, L. ; Detlefsen, O. ; Palm, M. ; Mach, K.-P. ; Steinwand, M. ; Jeinsch, T. ; Abdel-Maksoud, M.: Dynamic positioning with Voith Schneider Propeller: Experimental system validation with a model-scale offshore supply vessel. In: *22nd International Conference on Methods and Models in Automation and Robotics (MMAR)* IEEE, 2017, S. 7–12

[49] Kröger, H.-P.: Simulation der Rollbewegung von Schiffen im Seegang. (1987). – Schriftenreihe Schiffbau, Technische Universität Hamburg-Harburg, 473

[50] Lübcke, A.: *Modellierung von Windkräften im Zeitbereich*. 2012. – Last accessed 16 January 2022

[51] Lübcke, A.: *Dynamisches Positionieren als Aspekt in der frühen Schiffsentwurfsphase*. Technische Universität Hamburg, 2019

[52] Lübcke, A. ; Krüger, S. ; Christiansen, J.: Calculation of the Dynamic Positioning Capability in Time Domain in Early Design Stages. In: *Proceedings of the 12th International Marine Design Conference*, 2015

[53] Mahrt, L.: Surface wind direction variability. In: *Journal of applied meteorology and climatology* 50 (2011), Nr. 1, S. 144–152

[54] Maruo, H.: The drift of a Body floating on waves. In: *Journal of Ship Research* 4 (1960), Nr. 1, S. 2–15

[55] Men, J. ; Krishnan, G. ; Dev, A.: DP Capability Analysis by Time-Domain Simulation Approach. In: *Message from Chairman,"OSV Singapore 2016" Organizing Committee* (2016)

[56] Meneghini, J.R. ; Saltara, F. ; Siqueira, C.L.R. ; Ferrari Jr, J.A.: Numerical simulation of flow interference between two circular cylinders in tandem and side-by-side arrangements. In: *Journal of fluids and structures* 15 (2001), Nr. 2, S. 327–350

[57] Menter, F.R.: Two-equation eddy-viscosity turbulence models for engineering applications. In: *AIAA journal* 32 (1994), Nr. 8, S. 1598–1605

[58] Mercier, R.S. ; Huijs, F.A.: Steady current forces on tanker-based FPSOs. In: *WIT Transactions on the Built Environment* 84 (2005)

[59] Newman, J.N.: The drift force and moment on ships in waves. In: *Journal of ship research* 11 (1967), Nr. 01, S. 51–60

[60] Nguyen, D. ; Pivano, L. ; Børhaug, B. ; Smogeli, Ø.: Dynamic station-keeping capability analysis using advanced vessel simulator. In: *SIMS 54th conference on Simulation and Modelling*, 2013

[61] Nienhuis, I.R.U.: Simulations of low frequency motions of dynamically positioned offshore structures. In: *Royal Institution of Naval Architects Transactions* 129 (1987)

[62] Odd, J.A. ; Løvseth, J.: The Frøya database and maritime boundary layer wind description. In: *Marine Structures* 19 (2006), Nr. 2-3, S. 173–192

[63] Odd, J.A. ; Løvseth, J.: Stability modifications of the Frøya wind spectrum. In: *Journal of wind engineering and industrial aerodynamics* 98 (2010), Nr. 4-5, S. 236–242

[64] Ogilvie, T.F.: Recent progress toward the understanding and prediction of ship motions. In: *5th ONR Symp. on Naval Hydrodynamics*, 1964

[65] Oliveira, M.C. ; Sphaier, S.: Numerical Simulation of Vortex Induced Vibrations in Three Dimensions Using a Hybrid Method. In: *Proceedings of the 20th International Conference on Offshore Mechanics and Arctic Engineering (OMAE Conference), Rio de Janeiro, Brazil*, 2001

[66] Oltmann, P. ; Sharma, S.D.: Simulation of combined engine and rudder maneuvers using an improved model of hull-propeller-rudder interactions. 1984. – Forschungsbericht

[67] Pinkster, J.A.: Low frequency second order wave exciting forces on floating structures. (1980)

[68] Popov, I.n ; Koschorrek, P. ; Haghani, A. ; Jeinsch, T.: Adaptive Kalman filtering for dynamic positioning of marine vessels. In: *IFAC-PapersOnLine* 50 (2017), Nr. 1, S. 1121–1126

[69] Quadvlieg, F. ; Hallmann, R. ; Hughes, G. ; Harris, R.: Improved dynamic positioning using wave feed forward. In: *International Conference on Offshore Mechanics and Arctic Engineering* Bd. 44359, 2011, S. 765–773

[70] Remery, G.F.M. ; Van Oortmerssen, G.: The mean wave, wind and current forces on offshore structures and their role in the design of mooring systems. In: *Offshore Technology Conference* OnePetro, 1973

[71] Rodi, W.: Experience with two-layer models combining the k-epsilon model with a one-equation model near the wall. In: *29th Aerospace sciences meeting*, 1991, S. 216

[72] Rp, Api u. a.: Design and analysis of stationkeeping systems for floating structures. In: *American Petroleum Institute* (2005)

[73] Salvesen, N.: Second-order steady-state forces and moments on surface ships in oblique regular waves. In: *Int Symp. On the Dynamics of Marine Vehicles and Structures in Waves*, 1974

[74] Schiffbau-Versuchsanstalt Potsdam: *Towing Tank*. `https://www.sva-potsdam.de/en/towing-tank/`. Version: 2022. – Last accessed 1 December 2022

[75] Serraris, J.: Time domain analysis for DP simulations. In: *International Conference on Offshore Mechanics and Arctic Engineering* Bd. 1, 2009, S. 595–605

[76] Shih, T.-H. ; Liou, W.W. ; Shabbir, A. ; Yang, Z. ; Zhu, J.: A new k-ϵ eddy viscosity model for high reynolds number turbulent flows. In: *Computers& fluids* 24 (1995), Nr. 3, S. 227–238

[77] Siemens PLM Software Inc: User Guide, STAR-CCM+ v11. 06. (2016)

[78] Smogeli, Ø. ; Trong, N.D. ; Borhaug, B. ; Pivano, L.: The next level DP capability analysis. In: *Proceedings of Dynamic Positioning Conference*, 2013

[79] Taylor, D.W.: The Speed and Power of Ships. In: *maritime press* (1943)

[80] Theilen, L.: *Diskretisierungsmethoden von Schiffsgeometrien zur Benutzung in Rechenverfahren für potenzialtheoretische Strömungen.* 2010. – Technische Universität Hamburg-Harburg, Studienarbeit

[81] Travin, A. ; Shur, M. ; Strelets, M. ; Spalart, P.: Detached-eddy simulations past a circular cylinder. In: *Flow, turbulence and combustion* 63 (2000), Nr. 1, S. 293–313

[82] Valčić, M. ; Prpić-Oršić, J.: Wind load estimation method based on Elliptic Fourier Descriptors. In: *Towards Green Marine Technology and Transport*. CRC Press, 2015, S. 903–910

[83] Van't Veer, R. ; Gachet, M.: Dynamic Positioning: Early Design, Capability and Offsets—A Novel Approach. In: *International Conference on Offshore Mechanics and Arctic Engineering* Bd. 3, 2011, S. 755–764

[84] Vaz, G. ; Waals, O.J ; Ottens, H. ; Fathi, F. ; Le Soue¨ f, T. ; Kiu, K.: Current affairs: Model tests, semi-empirical predictions and CFD computations for current coefficients of semi-submersibles. In: *International Conference on Offshore Mechanics and Arctic Engineering* Bd. 5, 2009, S. 877–887

[85] Vinh, T.C. ; Canh, T.N. u. a.: Establishing Mathematical Model to Predict Ship Resistance Forces. In: *Fluid Mechanics* 3 (2017), Nr. 5, S. 44

[86] Voith GmbH Co. KGaA: *Voith Inline Thruster Voith Inline Propulsor*. `https://voith.com/corp-de/antriebe-und-getriebe/voith-inline-thruster-voith-inline-propulsor.html`. Version: 2022. – Last accessed 27 January 2022

[87] Voith GmbH Co. KGaA: *Voith Radial Propeller*. `https://voith.com/corp-de/antriebe-und-getriebe/voith-radial-propeller.html`. Version: 2022. – Last accessed 27 January 2022

[88] Voith GmbH Co. KGaA: *Voith Schneider Propeller VSP*. `https://voith.com/corp-de/antriebe-und-getriebe/voith-schneider-propeller-vsp.html`. Version: 2022. – Last accessed 27 January 2022

[89] Wassermann, S. ; Feder, D.-F. ; Abdel-Maksoud, M.: Estimation of ship roll damping—A comparison of the decay and the harmonic excited roll motion technique for a post panamax container ship. In: *Ocean Engineering* 120 (2016), S. 371–382

[90] Wichers, J. ; Bultema, S. ; Matten, R.: Hydrodynamic research on and optimizing dynamic positioning system of a deep water drilling vessel. In: *Offshore Technology Conference* OnePetro, 1998

[91] Wilde, J.J. de ; Schrijvers, P. ; Witz, J.: CFD benchmark study from the wind load joint industry project. In: *Offshore Technology Conference* OnePetro, 2018

Appendix A

This appended section illustrates hydrodynamic wave and radiation forces and the use in a time simulation method compared with experimental data.

A.1: First order wave forces for the OSV

Comparison of the first order wave forces obtained from a two dimensional strip method and a three dimensional panel method for varying encounter angles for a wave length equal to ship length.

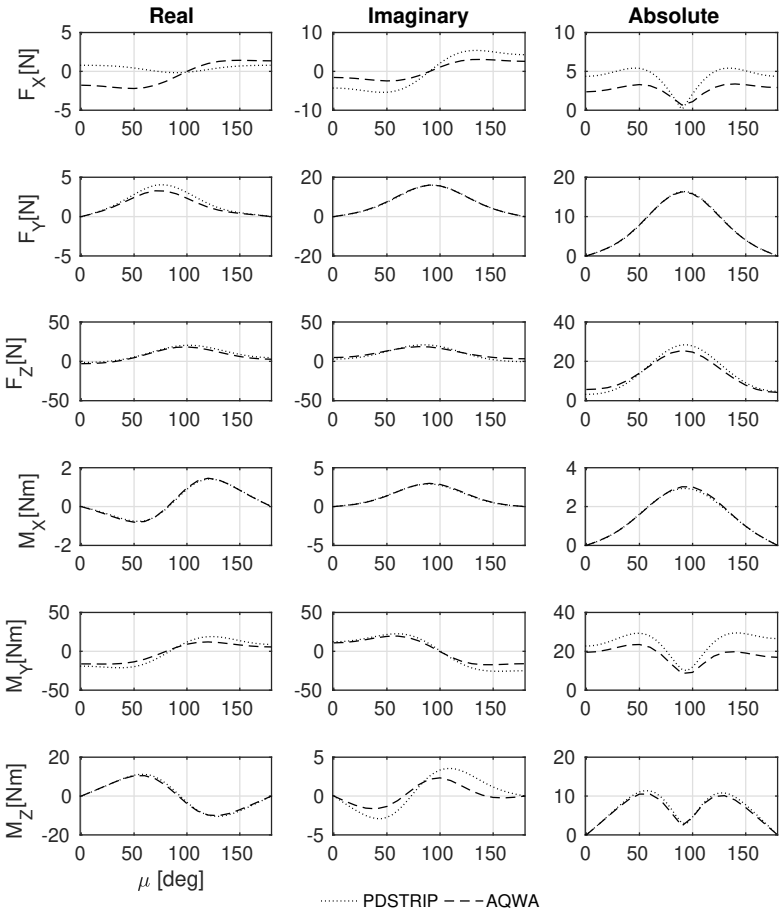

Figure 8.1: Froude Krylov and diffraction force λ/L_{PP}=1.0

A.2: Added mass matrix

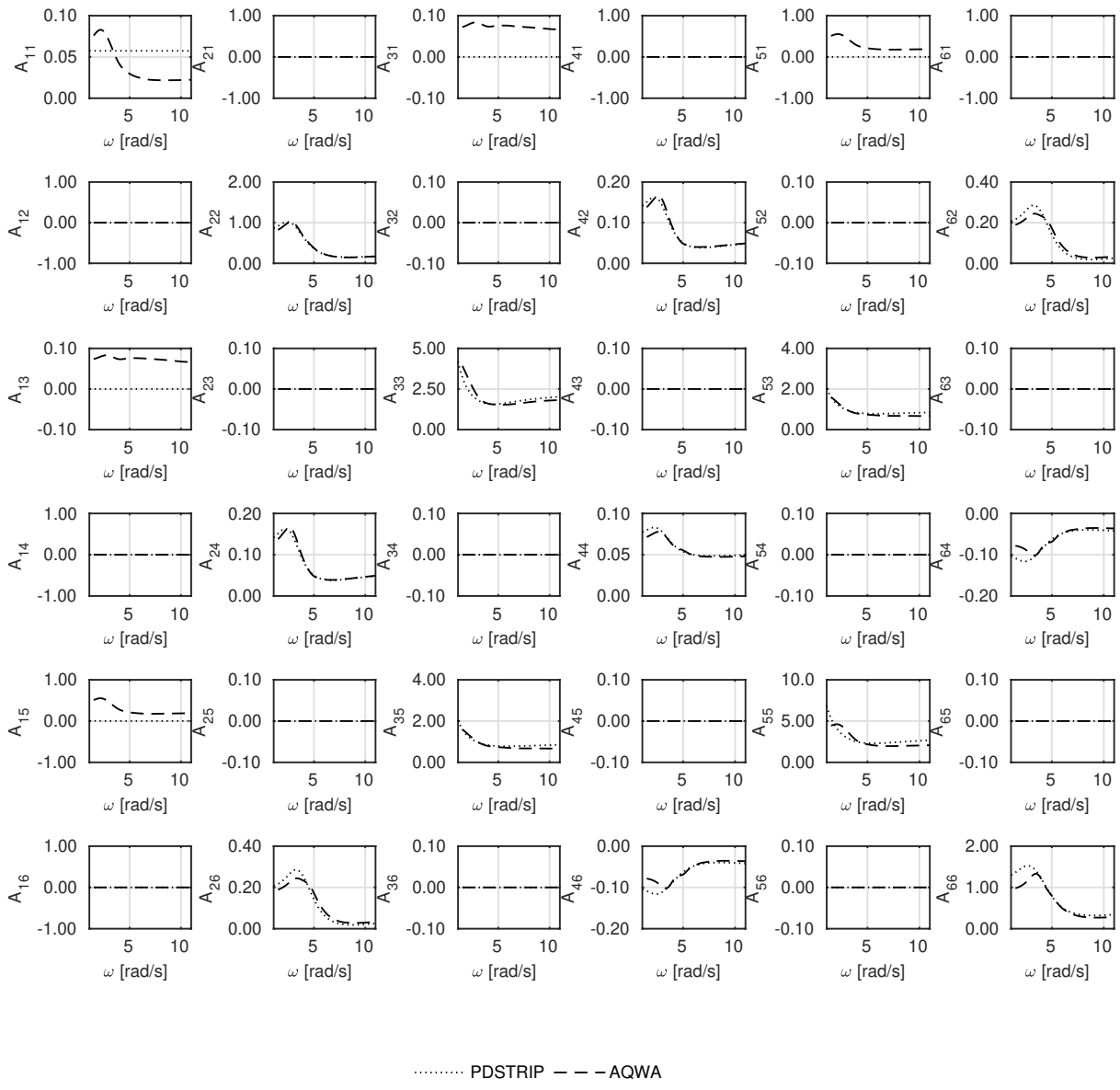

Figure 8.2: Added mass matrix $\mathbf{A}$ of OSV in model scale [$t\ m^2$]

A.3: Damping matrix

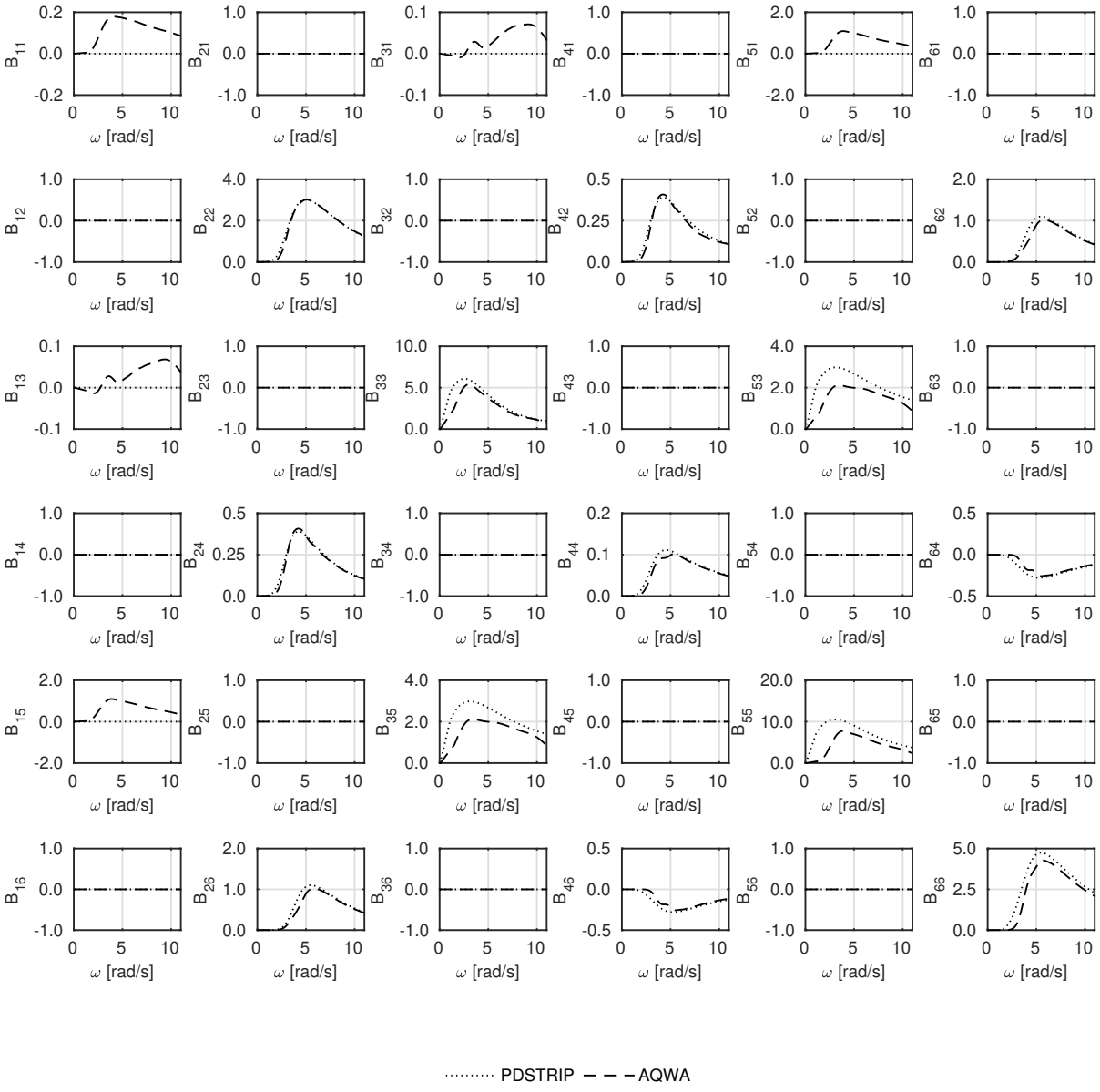

Figure 8.3: Damping matrix **B** of OSV in model scale [t / s^2]

A.4: Motion in regular waves

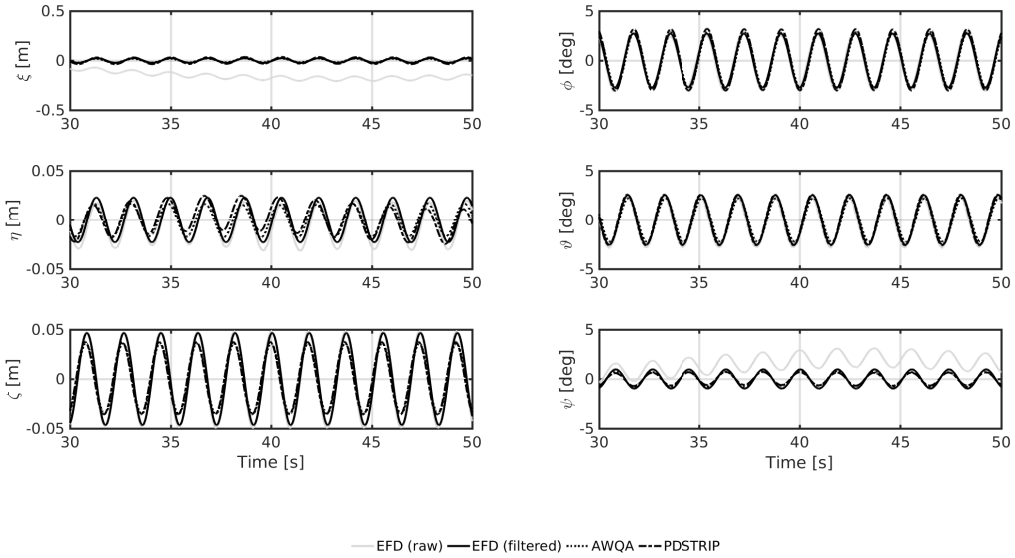

Figure 8.4: Ship motion in regular waves - μ =135deg, λ/L_{PP}=1.0

Appendix B

This appended section provides information about the model motion and drift forces

B.1

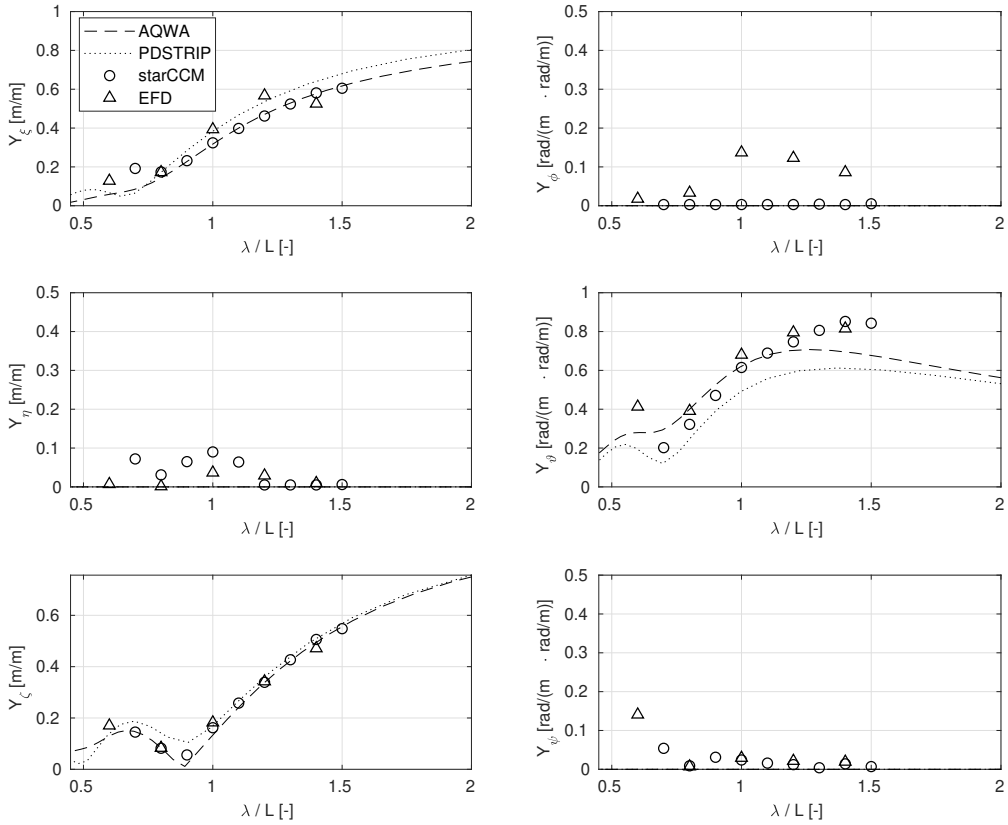

Figure 8.5: Response amplitude operator in following waves

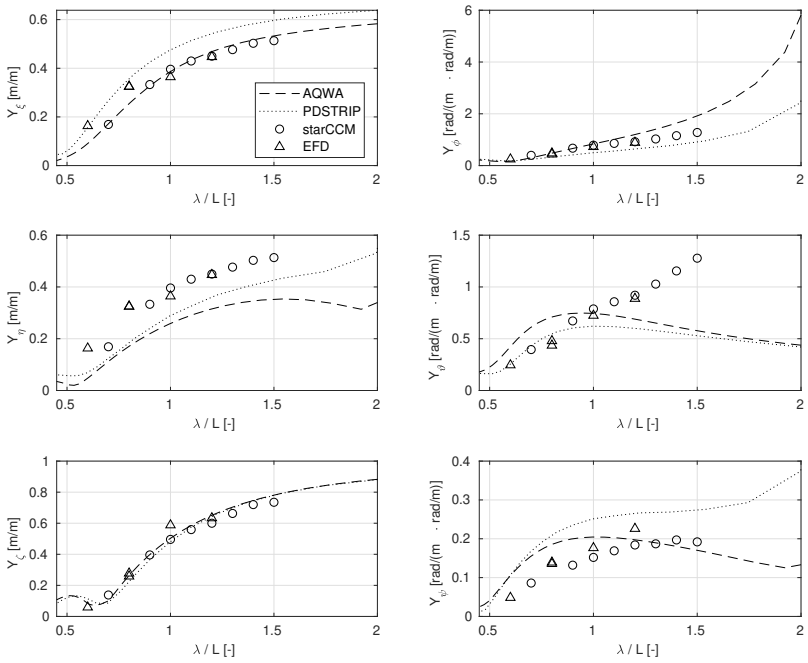

Figure 8.6: Response amplitude operator in quatering following waves

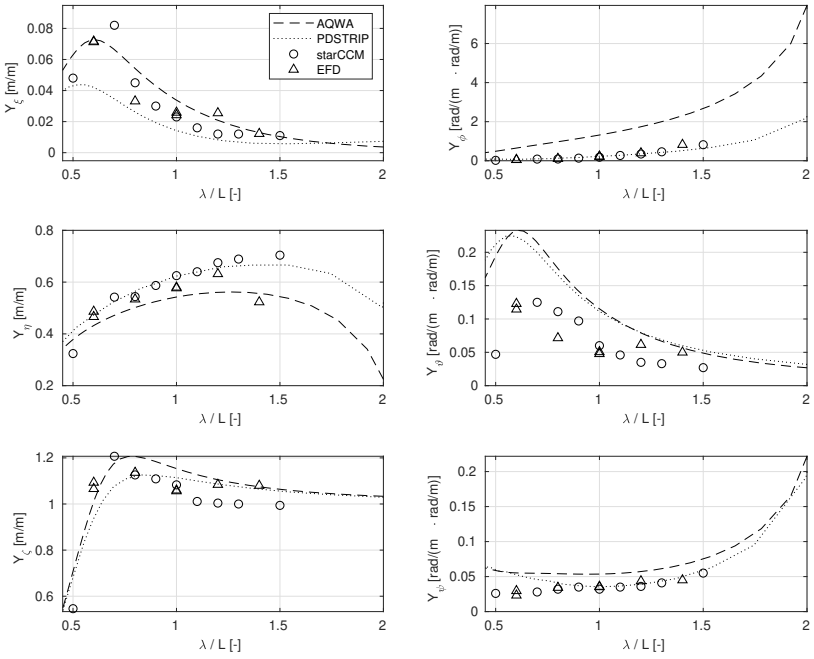

Figure 8.7: Response amplitude operator in beam waves

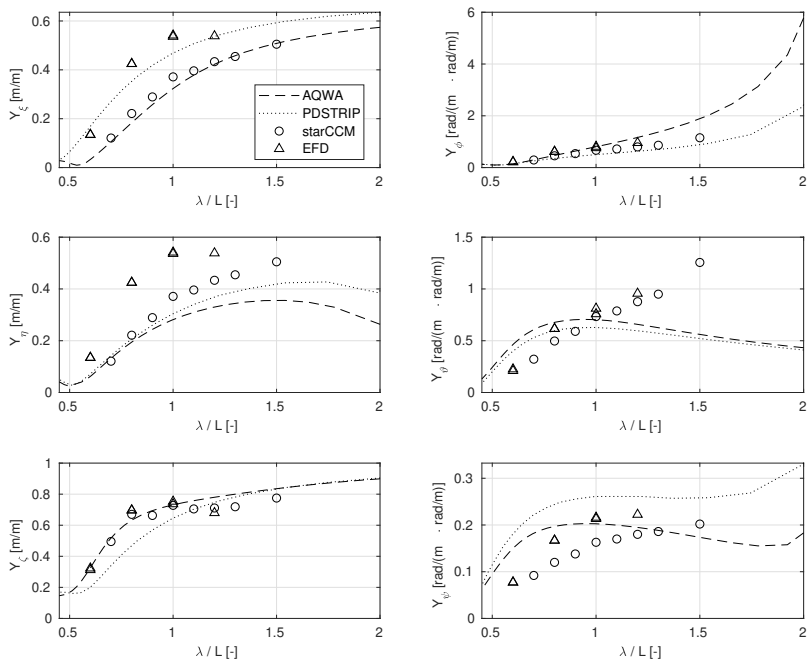

Figure 8.8: Response amplitude operator in quatering head waves

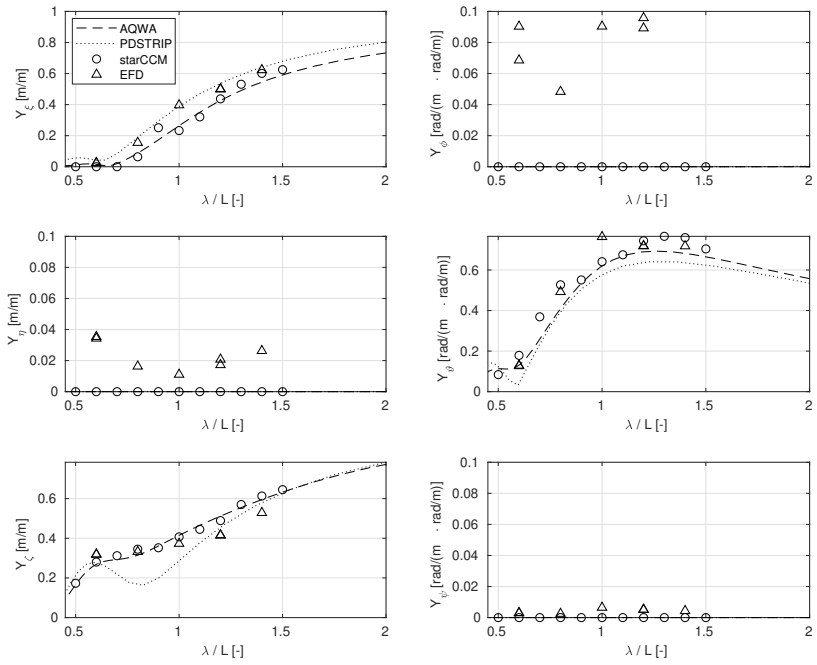

Figure 8.9: Response amplitude operator in head waves

B.2

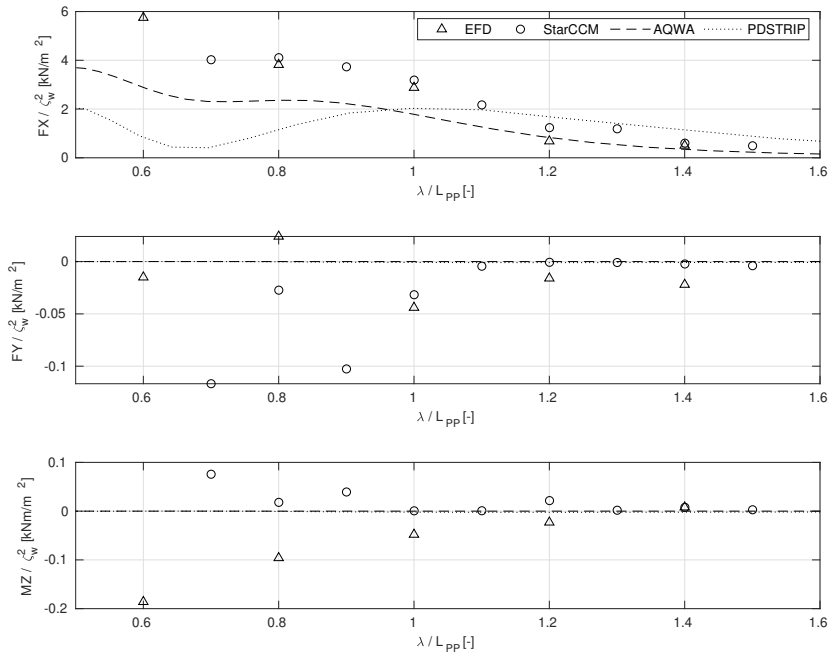

Figure 8.10: Comparison of wave drift loads in following waves ($\mu_w = 0°$)

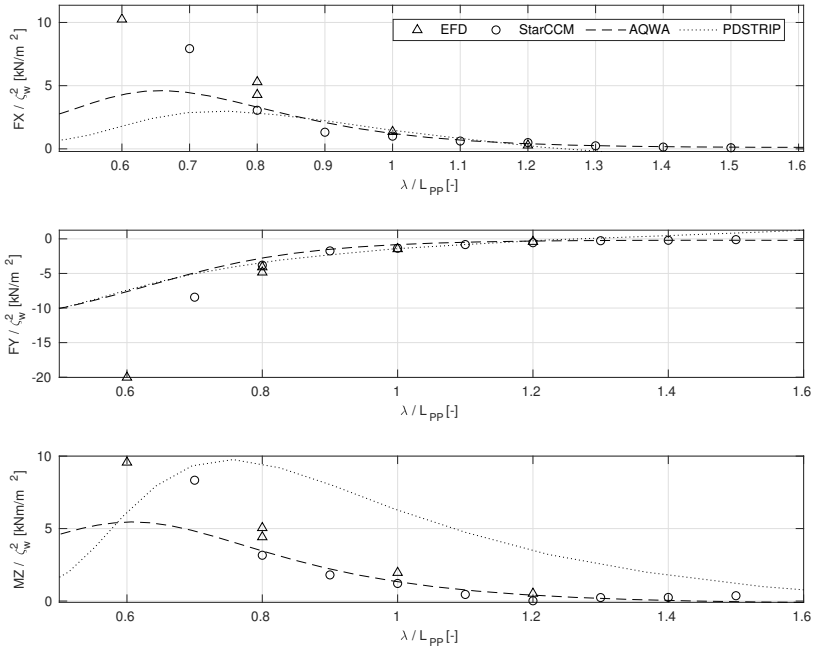

Figure 8.11: Comparison of wave drift loads in quatering following waves ($\mu_w = 45°$)

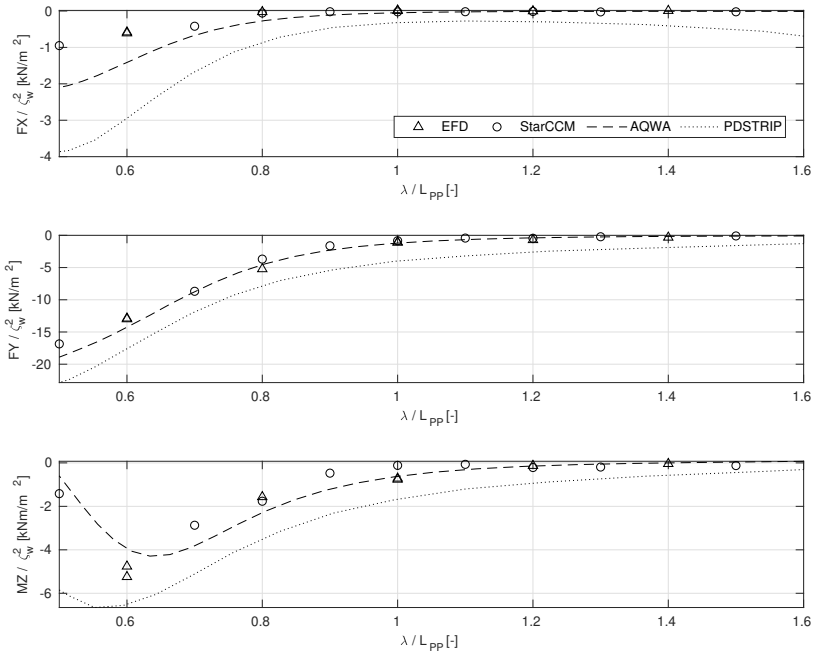

Figure 8.12: Comparison of wave drift loads in beam waves ($\mu_w = 90°$)

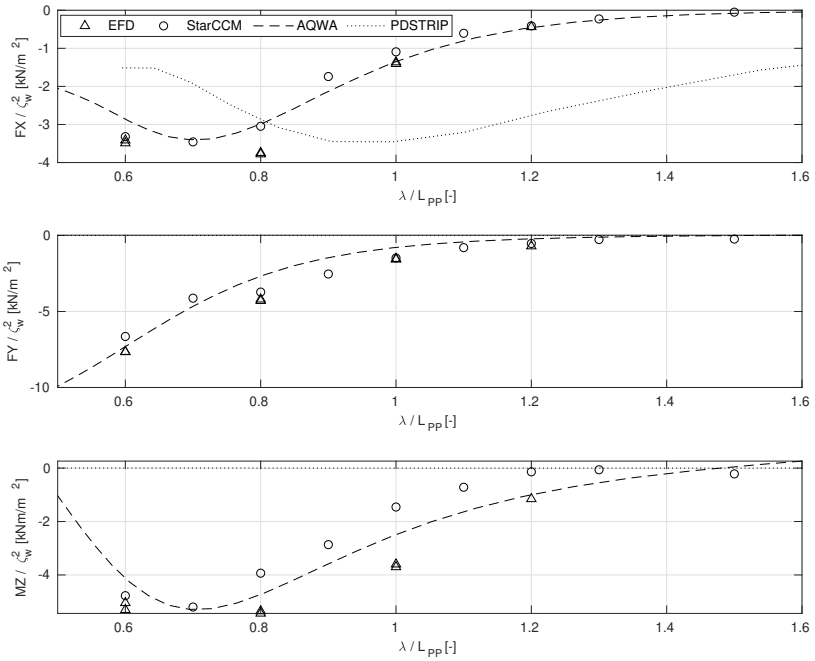

Figure 8.13: Comparison of wave drift loads in quatering head waves ($\mu_w = 135°$)

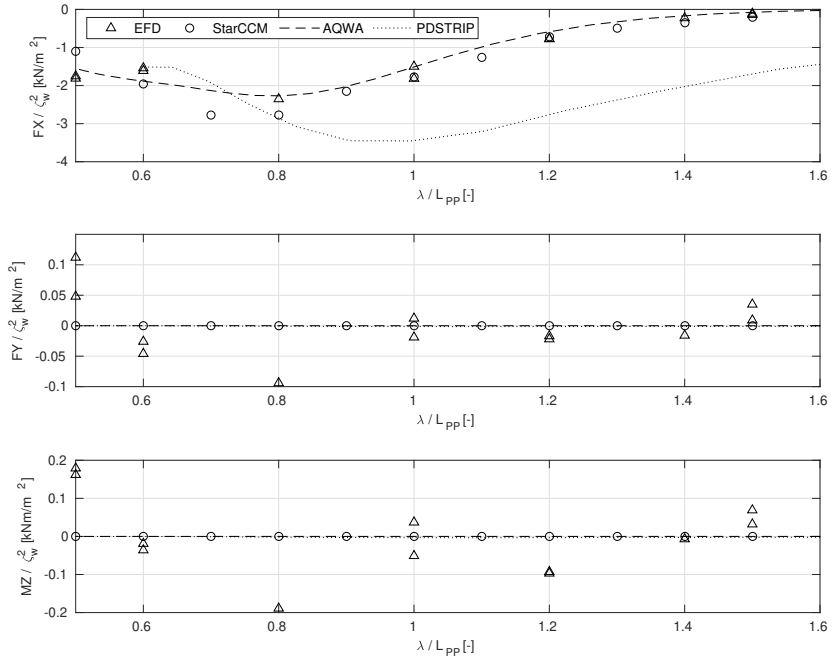

Figure 8.14: Comparison of wave drift loads in head waves ($\mu_w = 180°$)